Tunable Laser-Plasma Acceleration with Ionization Injection

by

Philipp Messner

A Thesis Submitted to the Faculty of

Mathematics, Informatics and Natural Sciences

Department of Physics

for the Degree of

DOCTOR RERUM NATURALIUM

Universität Hamburg

April 2020

Eidesstattliche Versicherung / Declaration on oath

Hiermit versichere ich an Eides statt, die vorliegende Dissertationsschrift selbst verfasst und keine anderen als die angegebenen Hilfsmittel und Quellen benutzt zu haben.

Die eingereichte schriftliche Fassung entspricht der auf dem elektronischen Speichermedium.

Die Dissertation wurde in der vorgelegten oder einer ähnlichen Form nicht schon einmal in einem früheren Promotionsverfahren angenommen oder als ungenügend beurteilt.

Hamburg, den 28.4.2020 _____

Philipp Messner

Abstract

Accelerating electrons to relativistic energies by an intense laser field interacting with a plasma is a widely considered concept to drive future applications such as compact light sources. The strong requirements on the electron beam quality imposed by these applications requires to precisely control the injection and acceleration dynamics and hence the parameters of the laser-plasma accelerated electrons.

This thesis studies electron beam generation with ionization injection in a nitrogen doped hydrogen plasma, focused on tunability and improvement of electron beam parameters. A capillary type plasma target was developed and characterized with Computational Fluid Dynamic (CFD) simulations allowing extensive parameter scans. It is demonstrated that electron beam parameters can be tuned in a wide range with peak energies between $200\,\mathrm{MeV}$ and $350\,\mathrm{MeV}$, bunch charges between $100\,\mathrm{pC}$ and $350\,\mathrm{pC}$ at percent-level shot-to-shot stability, by varying the laser focus position, laser pulse energy, plasma density and the nitrogen concentration. The accelerator performance could be optimized by controlling beam loading effects with a combination of the nitrogen concentration and the laser pulse energy, resulting in electron beams with reduced energy spread at simultaneously increased peak charge density.

The laser pulse energy showed the strongest influence on the transverse beam parameters, allowing to fine-tune beam divergence and beam emittance, a crucial prerequisite to optimize electron beams for the transport with electron beam optics.

The broad parameter scans could be reproduced with Particle-In-Cell (PIC) simulations, providing an in-depth understanding of the injection and acceleration dynamics in the ionization injection scheme. The presented results and the identified scalings can give a guideline for the operation regime for future experiments and to develop improved plasma targets to further enhance the electron beam quality.

Zusammenfassung

Das Beschleunigen von Elektronen auf relativistische Energien durch die Interaktion eines intensiven Laserfelds und eines Plasmas ist eine vielversprechende Technologie um zukünftige Anwendungen, wie zum Beispiel kompakte Lichtquellen, zu betreiben. Solche Anwendungen setzen jedoch ein hohes maß an Strahlqualiät vorraus. Es ist deshalb notwendig, den Injektions- und Beschleunigungsprozess genau zu kontrollieren, um damit die Parameter der *laser-plasma* beschleunigten Elektronenstrahlen einzustellen.

In dieser Arbeit wird die Erzeugung von Elektronenstrahlen mittels Ionisationsinjektion in einem Stickstoff dotierten Wasserstoff Plasma hinsichtlich der Durchstimmbarkeit und des Optimierungspotentials untersucht. Eine, auf einer Kapillare basierende, Plasmaquelle wurde mittels 3D Computational Fluid Dynamics (CFD) Simulationen entwickelt und charakterisiert. Mit dieser Plasmaquelle konnten umfasse Parameter Scans durchgeführt werden. Eine weitreichende Durchstimmbarkeit der Elektronenstrahleigenschaften konnte nachgewiesen werden, indem die Fokusposition des Lasers, die Pulsenergie, die Plasmadichte und die Stickstoffkonzentration verändert wurden. Die erzeugten Elektronenstrahlen hatten Spitzenenergien im Bereich von 200 MeV bis 350 MeV, Strahlladungen zwischen 100 pC und 350 pC bei einer Schuss-zu-Schuss Stabilität die im Bereich von wenigen Prozenten lag. Der Beschleunigungsprozess wurde optimiert , indem *beam laoding* Effekte mit der Stickstoffkonzentration und der Pulsenergie des Laser angepasst wurden. Dies reduzierte die Energiebreite der Elektronenstrahlen während die Spitzenladungsdichte gleichzeitig erhöt wurde.

Die transversalen Eigenschaften der Elektronenstrahlen waren sehr sensitiv auf die Pulsenergie des Laser. Damit war es möglich, die Divergenz und die Emittanz der Elektronenstrahlen sehr genau zu verändern. Dies stellt eine wichtige Voraussetzung dar, um die Elektronenstrahlen für den Transport mit Elektronenoptik zu optimieren.

Die Ergebnisse der weitreichenden Parameter Scans konnten mit *Particle-In-Cell* (PIC) Simulation bestätigt werden. Dadurch konnte ein tiefreichendes Verständniß von den Injektions- und Beschleunigungsprozossen im Bereich der Ionisationsinjektion erlangt werden. Die Ergebnisse und die gezeigten Zusammenhänge können den Parameterraum in dem der Beschleuniger in zukünftigen Experimenten betrieben werden soll vorgeben und helfen bei der Entwicklung neuer Plasmaquellen, um die Strahlqualität weiter zu verbessern.

Contents

List of Figures

List of Tables

1 Introduction

Laser-Plasma Accelerators (LPAs) have achieved great progress since they were first proposed by Tajima and Dawson in 1979 [1], producing GeV-class electron beams [2–4] with femtosecond bunch durations [5], nanocoulombs of bunch charge [6], kiloampere peak currents [7] and normalized emittances on the mm mrad level [8]. These electron beam parameters are achieved in only few centimeter long plasma stages, leading to LPAs being envisaged as compact drivers for future applications, such as light and radiation sources [9–13] or even for Free-Electron-Lasers (FELs) [14–16].

In laser-plasma acceleration, the radiation pressure of a high-intensity laser pulse creates an electron density modulation in a plasma medium, called plasma target, resulting in a charge separation and strong electric fields. These wakefields provide large longitudinal acceleration fields with gradients on the order of several tens of GVm^{-1}, which exceeds what Radio Frequency (RF) based accelerators can provide [17]. Thus, electrons experiencing these fields can gain ultra-relativistic energies within short distance. Recently, a beam energy of 8 GeV from a just 20 cm long laser-plasma interaction has been reported [4]. The accelerating cavity of the wakefield, called bucket or bubble, further provides strong transverse focusing fields. The length scale of this cavity is covered by the plasma wavelength λ_p and typically in the range of a few tens of micrometers [17]. Combined with the strong focusing fields, this results in electron beams with an intrinsically short bunch duration and extremely small transverse beam size [5]. It is these electron beam parameters which make LPAs promising candidates to replace RF based accelerators as driver for future applications at reduced size and cost.

Although LPAs offer beam energies and bunch charges comparable to state-of-the-art conventional accelerators, they can typically not compete in rep-rate, beam quality, especially in terms of energy spread. In addition, as the accelerating cavity is created dynamically, laser-plasma acceleration is very sensitive to laser pulse and plasma properties and therefore often suffers from shot-to-shot variations in electron beam parameters [18]. These limitations have to be addressed in order for LPAs to become applicable as drivers for future applications. Furthermore, such applications inevitable relay on complex electron beam optics and bunch shaping devices, required for electron phase-space manipulation [14–16]. These devices allow to optimize the electron beam quality but can typically only be operated in a narrow parameter space. Thus, stable, reproducible

and tunable electron beam generation is mandatory for the daily operation of a complex, laser-plasma driven beamline.

Control and optimization of laser-plasma generated electron beams can be addressed from two sides: either by the parameters of the high-power laser driver, or by the properties of the plasma source. Amongst the online accessible parameters of todays laser systems affecting the acceleration are the laser pulse energy, pulse length, the focal spot position and the spectral phase [17, 19, 20]. There are, of course, even more laser parameters influencing the electron beam quality, for example focal spot size, laser wavefront, or spatial-temporal couplings [19, 21]. However, these parameters are not readily accessible online.

On the plasma source side, beam parameters are mainly determined during injection, referring to the process of electrons entering the accelerating region of the wakefield. [17]. In general, an electron is trapped if it co-propagates with the wakefield at equal velocity, i.e. the laser group velocity which roughly coincides with the speed of light. This can be achieved two-fold, either by increasing the electron velocity or by reducing the phase velocity of the wakefield. The most simple method to increase the electron velocity is to drive the wakefield with such high laser intensities that the wakefield structure collapses [22, 23]. At this point, some plasma background electrons gain enough momentum while scattering at the back of the bucket to reach the accelerating phase of the wakefield. The so called self-injection scheme has generated mono energetic electron beams but is limited in stability and control over the injection phase due to the highly non-linear and statistical nature of the process. Therefore, several advanced techniques have been proposed to trigger injection at preferred phase and longitudinal position in the plasma target to more precisely control electron beam parameters.

Amongst those techniques are plasma density transition injection schemes reducing the phase velocity of the wakefield [24–26] such that electrons can easily catch up, optical schemes using an additional heater laser to locally increase the electron momentum [27–29], or ionization induced injection, where inner shell electrons of a high-Z gas are born and are trapped inside the laser electric field [30–32]. The last one mentioned is a widely used injection scheme as it is easy to implement and allows for robust electron beam generation.

The ionization injection scheme utilizes the large gap in the ionization potential between inner shell electrons of a high-Z gas to trigger and localize injection [33]. This is achieved by adding a small amount of high-Z gas, for example nitrogen, to the low-Z gas, typically hydrogen, forming the plasma background. Electrons are ionized at different locations inside the laser field, depending on their binding potential. Hydrogen and the five nitrogen L-shell electrons are immediately ionized by the leading edge of the laser pulse, whereas the strongly bound Nitrogen K-shell electrons are only ionized close to the intensity peak of the laser pulse, for typical peak intensities $> 10^{18} \, \mathrm{Wcm}^{-2}$. Only the inner

shell electrons are born at a correct phase, are trapped by the wakefield and accelerated. Not only the intensity threshold for the injection is reduced compared to self-injection [34, 35] which results in robust electron trapping, but electron beam parameters can also be tuned in a wide range with several laser pulse and plasma properties.

The drawback of the injection scheme is the continuous longitudinal injection of electrons in the mixed gas length, typically resulting in electron beams with a broad spectrum [33]. Several techniques were investigated to reduce the energy spread, including separation of injection and acceleration in two subsequent stages, plasma density tailoring [36, 37] and using multiple laser beams [38, 39]. However, these methods require a complex set-up, precise alignment and the operation is often limited to a small parameter space. Thus, electron beam generation with ionization injection in a single stage plasma target with continuous mixed gas length is still a vivid research topic.

This thesis reports on the detailed experimental study of ionization induced injection in a single stage plasma target. Electron beams were generated in a nitrogen doped hydrogen plasma with laser pulses from the 200 TW peak power laser system ANGUS at the Laser-driven Undulator X-ray (LUX) beamline in Hamburg, Germany [9]. Previously reported results of ionization injected electron beams were mostly focused on reducing the energy spread [36, 38–41]. Although electron beams with a small energy spread are required for most of the applications which are considered to be driven by a LPA, other beam parameters such as bunch charge, beam divergence and beam emittance are of equal importance. Due to the stable performance of the ANGUS laser system and the technical layout of the LUX beamline, it was possible to perform broad parameter scans and to generate over 15000 electron beams in a single campaign, allowing to investigate the effect of several laser and plasma properties on the these electron beam parameters simultaneously. Tuning of electron beam parameters in a wide range and percent level shot-to-shot accelerator stability are presented.

This thesis is structured as follows. The fundamentals required to discuss laser-plasma acceleration are presented in chapter 2. The experimental setup including the ANGUS laser system, the LUX beamline and the relevant laser and electron beam diagnostics are presented in chapter 3. The design of a capillary type plasma target with 3D Computational Fluid Dynamics (CFD) simulations and the gas supply and diagnostics setup are discussed in chapter 4. Injection and acceleration dynamics in the plasma target allowing for a more theoretical interpretation of the experimental results are discussed with Particle-in-Cell simulations (PIC) in chapter 5. The characteristics features of the electron beams generated within this thesis and a discussion on the accelerator stability are presented in chapter 6. Finally, the results on electron beam generation with ionization injection are discussed in chapter 7. A conclusion and suggestions for further improvements to achieve higher electron beam quality are given in chapter 8.

2 Fundamentals

This chapter provides the theoretical background relevant for the interpretation of the experimental results on electron beam generation with ionization injection presented in chapter 7. A model of the driver laser is established in section 2.1. Section 2.2 covers the ionization mechanism of atoms in the presence of a laser field, which is the basis for the formation of the plasma medium in which electrons are accelerated. The principles of laser-plasma acceleration including the different wakefield regimes and a detailed description of the ionization injection scheme are presented in section 2.3. Modulation of the driver laser by non-linear effects during propagating in the plasma affecting the injection and acceleration dynamics are discussed in section 2.4.

2.1 Laser Model

The spatial intensity profile of a laser pulse is defined in two optical fields, the near-field and the far-field. The near-field corresponds to the region directly behind the emitting facet of the laser system. The far-field concerns the pulse properties at greater distance from the source, i.e. in the focal plane. Both regions are related by the spatial Fourier transformation [42]. Laser pulses of the ANGUS laser system used for the electron acceleration at LUX, see section 3.2, have a super Gaussian intensity profile in the near-field. In the far-field, the intensity profile is well approximated with a Gaussian function, i.e.

$$I(r, z) = I_0 \left(\frac{w_0}{w(z)} \right)^2 \exp \left(\frac{-2r^2}{w(z)^2} \right), \tag{2.1}$$

$$w(z) = w_0 \sqrt{1 + \left(\frac{z}{z_R} \right)^2}, \tag{2.2}$$

with $r = \sqrt{x^2 + y^2}$ being the the radial coordinate, I_0 the peak intensity in the focal plane, $w(z)$ the transverse $1/e^2$ beam radius, w_0 the beam radius in the focal plane and $z_R = \pi w_0^2 / \lambda_l$ the Rayleigh Range with λ_l being the central laser wavelength [43]. The

Rayleigh Range is the distance from the focal plane where the beam radius is increased by a factor of $\sqrt{2}$ and the intensity reduced by a factor of two.

In general, the electric field of a laser pulse can be expressed by its normalized vector potential $a = e\vec{A}/m_e c^2$, where e is the elementary charge, m_e the electron mass and c the speed of light. In analogy to eq. (2.1), the normalized vector potential of a linear polarized Gaussian pulse reads

$$a = a_0 \exp(-r^2/r_0^2)cos(k_l z - \omega_l t), \tag{2.3}$$

where $\omega_l = ck_l$ is the angular frequency with $k_l = 2\pi/\lambda$ being the wavenumber [17]. The peak amplitude a_0, also called laser strength parameter, is generally used to describe the strength of a laser pulse when discussing laser-plasma acceleration and is related to the laser peak intensity by

$$a_0 = \sqrt{\frac{2e^2\lambda_l^2 I_0}{\pi m_e^2 c^5}} \simeq 8.54 \times 10^{-10}\sqrt{I_0\left[\text{Wcm}^{-2}\right]}\lambda_l\left[\mu\text{m}\right]. \tag{2.4}$$

Furthermore, a_0 is used to distinguish between the quasi-linear, $a_0 \ll 1$, and non-linear regime, $a_0 \gg 1$, of laser-plasma acceleration, see section 2.3.1.

The propagation of a laser pulse in plasma is governed by the interaction of the electromagnetic field and the unbound plasma electrons. The response of the protons to the laser pulse can be neglected when discussing first order effects, because of their large mass. For the following discussion, constant laser pulse properties during propagating are assumed, implying low laser intensities, $a_0 \ll 1$. At higher laser intensities, the non-linearity of the plasma leads to a modulation of the spatial and temporal laser pulse properties, see section 2.4. The characteristic time scale on which electrons respond to the electromagnetic field is given by the plasma frequency

$$\omega_p = \sqrt{\frac{n_e e^2}{m_e \epsilon_0}}, \tag{2.5}$$

where n_e is the electron density and ϵ_0 the vacuum permittivity [44]. The 1D dispersion relation of an electromagnetic wave propagating in a plasma reads

$$\omega_l^2 = \omega_p^2 + c^2 k_l^2, \tag{2.6}$$

[44]. From this, the refractive index of the plasma is given by

$$\eta = \sqrt{1 - \frac{\omega_p^2}{\omega_l^2}}. \tag{2.7}$$

The refractive index becomes imaginary for $\omega_l < \omega_p$ and an electromagnetic wave is reflected by the plasma. The critical electron density, i.e. where $\omega_l = \omega_p$, is defined by $n_c = \omega_l^2 m_e \epsilon_0 / e^2$ or in practical units by

$$n_c \left[\text{cm}^{-3}\right] \simeq 1.12 \times 10^{21} \lambda_l^{-2} \left[\mu\text{m}\right], \tag{2.8}$$

[44]. A plasma is called underdense if $n_e < n_c$ and overdense if $n_c < n_e$. Laser-plasma accelerators driven by laser pulses with a wavelength of 800 nm are therefore operated in an underdense regime with electron densities below a critical density of $n_c \simeq 1.75 \times 10^{21}\,\text{cm}^{-3}$. The refractive index of the plasma is frequency dependent, causing the individual spectral components of the laser pulse to propagate at different phase velocities of

$$v_{ph} = \frac{c}{\eta} = \frac{\omega_l}{k_l} = \frac{c}{\sqrt{1 - \frac{\omega_p^2}{\omega_l^2}}}, \tag{2.9}$$

[45]. The pulse envelope containing all spectral components propagates with a group velocity of

$$v_g = \frac{\partial \omega_l}{\partial k_l} = \frac{c^2 k_l}{\omega_l} = c\sqrt{1 - \frac{\omega_p^2}{\omega_l^2}}, \tag{2.10}$$

[45]. As the laser pulse is the driver behind the electron density modulation in the palsma, it can be inferred that the phase velocity of the wakefield equals the laser group velocity, i.e. $v_p \simeq v_g$. It is shown in section 2.3.2 that the phase velocity of the plasma wakefield plays a crucial role in triggering electron injection.

2.2 Ionization

The plasma medium in which electrons are accelerated is created by ionization of a neutral gas density distribution confined in so called plasma targets, see chapter 4. Ionization can either be induced with an externally applied electric field, such as a high current discharge, or by the leading edge of the laser pulse driving the acceleration itself. The last one mentioned is relevant for the experiments conducted within this thesis. The following

discussion, if not otherwise stated, is based on the theory given by P. Gibbon in [45].

The atomic Coulomb potential $V(r)$ of an atom in the presence of an alternating electric field, such as that of a laser pulse, is given by

$$V(r) = -\frac{Ze^2}{r} - eE_l r, \tag{2.11}$$

where Z is the charge state of the ion, E_l the laser electric field and r the distance. An electron is freed with a probability of one if the electric field is strong enough to suppress the Coulomb potential below the binding potential of the bound electron. This process is called Barrier Suppression Ionization (BSI) and illustrated in figure 2.1a.
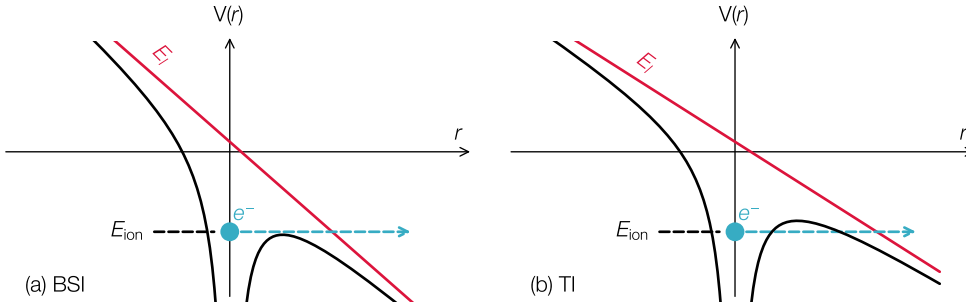
Figure 2.1 – Suppression of the atomic Coulomb potential $V(r)$ (black) by an alternating electric field E_l (red) frees an electron either through Barrier Suppression Ionization (BSI) (a) or Tunnel Ionization (TI) (b).

The required intensity to reach Barrier Suppression Ionization is called appearance intensity and is approximated in practical units by

$$I_{\mathrm{app}} \left[\mathrm{Wcm}^{-2} \right] \simeq 4 \times 10^9 E_{\mathrm{ion}}^4 \left[\mathrm{eV} \right] Z^{-2}, \tag{2.12}$$

where E_{ion} is the ionization potential characteristic for the charge state Z. The BSI model states the intensity threshold for ionization of a certain charge state with a probability of one. An atom is fully ionized if the laser intensity exceeds the appearance intensity of the most deeply bound electron and partially ionized otherwise. In the experiments performed within this thesis, the plasma was formed from a hydrogen-nitrogen gas mixture. The ionization potentials, the appearance intensity and the corresponding laser strength parameters of these atoms are listed in table 2.1.

Table 2.1 – Ionization potentials E_{ion} [46] and appearance intensities I_{app} of the relevant hydrogen and nitrogen ions, calculated with eq. (2.12). The laser strength parameter a_0 is calculated with eq. (2.4) for $\lambda_l = 800\,\mathrm{nm}$.

ion	$E_{\mathrm{ion}}\,(e\mathrm{V})$	$I_{\mathrm{app}}\,(\mathrm{Wcm^{-2}})$	a_0
H^{1+}	13.6	1.37×10^{14}	0.008
N^{1+}	14.53	1.78×10^{14}	0.009
N^{2+}	29.6	7.68×10^{14}	0.019
N^{3+}	47.45	2.25×10^{15}	0.032
N^{4+}	77.47	9.0×10^{15}	0.065
N^{5+}	97.89	1.47×10^{16}	0.082
N^{6+}	552.1	1.03×10^{19}	2.18
N^{7+}	667	1.61×10^{19}	2.73

If the laser intensity is below the appearance intensity, ionization occurs through Tunnel Ionization (IT) where an electron passes through the Coulomb barrier with a certain probability $\leqslant 1$, see figure 2.1b. The most common model used to describe Tunnel Ionization is the Ammosov, Delone and Krainov (ADK) model [47]. The tunnel ionization probability with an initial energy ϵ in the presence of a linearly polarized laser field is given by

$$\Gamma_{\mathrm{ADK}} \sim \exp\left(-\frac{2}{3}\left[\frac{\lambda_l}{\lambda_c} a^3 \gamma_K^3 \frac{E_k}{|E(\tau)|} + \frac{\gamma_k^3 \epsilon}{\hbar\omega} \right] \right), \tag{2.13}$$

where $\lambda_c = h/m_e c$ is the Compton wavelength with h being the Planck constant, $\gamma_k = (\alpha_f/a)(E_{ion}/E_{\mathrm{H}})^{1/2}$ the Keldysh parameter with $\alpha_f = e^2/\hbar c \simeq 1/137$ the fine structure constant, $E_{\mathrm{H}} = 13.6\,\mathrm{eV}$ the ionization potential of hydrogen, $E(\tau)$ the laser electric field as a function of time and $E_k = m_e c^2/e$. Figure 2.2 shows the ADK ionization probabilities for the relevant hydrogen and nitrogen ions calculated with eq. (2.13) as a function of longitudinal position inside the laser electric field. Hydrogen and the five nitrogen L-shell electrons are immediately ionized by the leading edge of the laser pulse. Ionization of the first nitrogen K-shell electron N^{6+}, on the other hand, only is significant inside the laser electric field close to the intensity peak. The ionization probability of the second nitrogen K-shell electron N^{7+} is comparably low with $10\,\%$ as the laser intensity is not sufficiently high to suppress the atomic Coulomb potential up to this charge state.
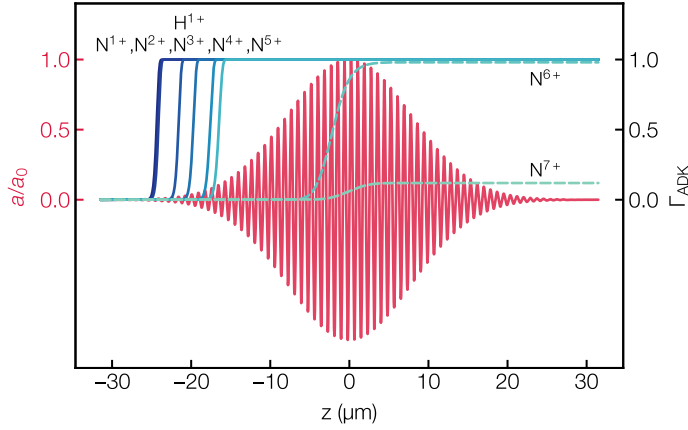
Figure 2.2 – ADK Tunnel Ionization probabilities of hydrogen and nitrogen ions calculated with eq. 2.13, inside a laser electric field (red) with $a_0 = 2.2$, $\tau = 35\,\mathrm{fs}$ (FWHM) and $\lambda_l = 800\,\mathrm{nm}$.

The different ionization locations of electrons within the laser electric field is the key principle employed in the ionization injection scheme to control electron trapping. It is shown in section **??** that only inner shell electrons born close to the intensity peak of the laser pulse have the correct phase to be trapped by the wakefield, whereas electrons born at the leading edge of the laser pulse only contribute to the plasma background.

2.3 Principles of Laser-Plasma Acceleration

Laser-Plasma Accelerators exploit the high electric fields of plasma waves to accelerate electrons to relativistic energies. These plasma waves result from an electron density modulation created by a high intense laser pulse. Figure 2.3 schematically illustrates the laser-plasma interaction. A laser pulse propagating through an initially homogeneous plasma expels the electrons transversely from its propagation axis towards regions of weaker field strength via the ponderomotive force

$$F_p = -\frac{e^2}{4m_e\omega}\nabla E^2 = -m_e c^2 \nabla \frac{a^2}{2}, \tag{2.14}$$

where E is the electric field of the laser pulse [17]. The ponderomotive force is obtained by averaging the Lorentz force over one oscillation cycle of the laser field and can be understood as radiation pressure. The ponderomotive force also acts on the plasma ions but they only gain negligible momentum due to their large mass and can be treated to be at rest during the timescale of the interaction. Thus, the ponderomotive force introduces a space charge separation in the plasma, resulting in electric fields acting to restore the
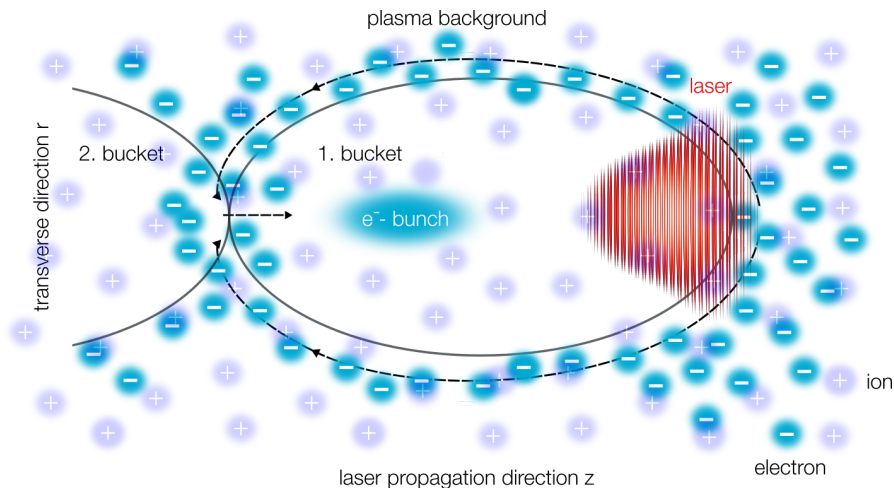
Figure 2.3 – Illustration of laser-plasma acceleration. Plasma electrons (-) are transversely expelled from the laser (red) propagation axis (red) by the ponderomotive force while the heavy plasma ions (+) stay at rest. The electron density modulation is called wakefield and each period is referred to as bubble or bucket.

equilibrium. The displaced electrons are therefore accelerated back towards the laser propagation axis once the pulse has passed. They overshoot their initial equilibrium position and start to oscillate around the laser propagation axis with the plasma frequency ω_p. As a result, the laser pulse creates alternating regions of higher and lower electron density when propagating through the plasma. It is the resulting longitudinal, quasi static electric fields between the two regions which are utilized to accelerate an electron witness bunch. The density modulation is referred to as wakefield and each acceleration cavity to as bubble or bucket.

The peak acceleration gradient of the wakefield scales with the electron density of the plasma according to

$$E_0 \left[\mathrm{Vm}^{-1}\right] \simeq 96\sqrt{n_e \left[\mathrm{cm}^{-3}\right]}. \tag{2.15}$$

Considering a typical electron density of $\times 10^{18}\,\mathrm{cm}^{-3}$, $E_0 = 96\,\mathrm{GVm}^{-1}$, which is orders of magnitude larger than what conventional Radio-Frequency (RF) based accelerators can provide [17]. Electron bunches externally injected or created within these wakefields can thus gain GeV-level energies within only a few millimeter distance. In addition to the large longitudinal accelerating fields, the wakefield structure provides strong transverse focusing forces on the order of $100\,\mathrm{MVm}^{-2}$ keeping electrons well confined in a small volume during acceleration [17]. The wakefield characteristic depend on the plasma properties as well as on the laser intensity. The different regimes of laser-plasma acceleration are discussed in the following section, see 2.3.1.

2.3.1 Regimes of Laser-Plasma Acceleration

Wakefield excitation and the characteristics of the plasma waves depend on the intensity of the laser pulse and can be separated into the linear, $a_0 \ll 1$, and non-linear, $a_0 \gg 1$, regime. The structure of the wakefield is derived by solving the differential equation for the scalar potential ϕ. The remaining wakefield parameters such as the electron density modulation $\delta n = n_e - n_0$ and the longitudinal electric field E_z can then be deduced from ϕ. The following section introduces the governing equations of the scalar potential to illustrate the characteristics of both regimes, but is not aimed to give a full derivation of wakefield excitation. For a more detailed and in depth discussion it is referred to [17, 45].

Linear Regime: $a_0 \ll 1$
The differential equation for the scalar potential in the linear regime reads

$$\left(\frac{\partial^2}{\partial \xi^2} + k_p^2 \right) \phi = -k_p^2 \Phi_L, \tag{2.16}$$

where $\Phi_L = -1/2 \left\langle a^2 \right\rangle$ is the ponderomotive potential averaged over one laser period and $\xi = z - v_g t$ the position behind the laser pulse [45]. Figure 2.4a shows the wakefield parameters derived from eq. (2.16). The electron density modulation and the electric field show a sinusoidal shape as the plasma electrons are not expelled noticeably by the comparably weak laser field and mainly oscillate around their initial position. The length scale of the oscillation is given by the plasma wavelength

$$\lambda_p \, [\mu m] = 3.3 \times 10^{10} \sqrt{n_0 \, [cm^{-3}]}, \tag{2.17}$$

[17]. For a typical electron density of $n_0 = 10^{18} \, cm^{-3}$, $\lambda_p \sim 33 \mu m$. The gray shaded areas in figure 2.4a indicate the regions of accelerating, $E_z < 0$, and transverse focusing, $\delta n / n_0 < 0$, fields are present.

Non-Linear Regime: $a_0 \gg 1$
The motion of the plasma electrons becomes relativistic in a strong laser field and the mass increase has to be considered. The differential equation for the static potential in the non-linear regime reads

$$\frac{\partial^2 \phi}{\partial \xi^2} = k_p^2 \gamma_p^2 \left(\beta_p \left(1 - \frac{1 + a^2}{\gamma_p^2 (1 + \phi)^2} \right)^{-1/2} - 1 \right), \tag{2.18}$$

where $\gamma_p = 1/\sqrt{(1 - \beta_p^2)}$ is the relativistic Lorentz factor and $\beta_p = v_p/c$ the normalized phase velocity of the wakefield [45]. The non-linear wakefield parameters resulting from eq. (2.18) are shown in figure 2.4b. The plasma electrons accumulate in smaller and more distanced regions than in the liner case. The electron density modulation is therefore strongly peaked instead of sinusoidal and the resulting electric field approaches a sawtooth shape with large gradients. The plasma wavelength in the non-linear regime is given by

$$\lambda_{Np} = \lambda_p \begin{cases} 1 + 3(E_{max}/E_0)^2/16, & E_{max}/E_0 \ll 1 \\ (2/\pi)(E_{max}/E_0 + E_0/E_{max}), & E_{max}/E_0 \gg 1 \end{cases}, \qquad (2.19)$$

[17]. It is seen by the gray shaded areas in figure 2.4b that the plasma wavelength and hence the accelerating and focusing regions are elongated compared to the linear regime. Thus, electrons can be accelerated to higher energies before they outrun the laser pulse and reach the decelerating region of the wakefield. This effect, called dephasing, is discussed in section 2.3.4.

Blowout/Bubble Regime
A special regime within the non-linear regime is reached when the laser intensity is sufficiently high such that all plasma electrons are expelled from the laser propagation axis. The resulting electron void behind the laser pulse has the shape of a bubble, giving the regime its name [48]. The threshold for this complete electron blowout is given by

$$\frac{a_0^2}{\sqrt{1 + a_0^2}} \geqslant \frac{k_p^2 w_0^2}{4}. \qquad (2.20)$$

The condition is either fulfilled for a laser intensities of $a_0 \geqslant k_p^2 w_0^2/4$ or laser spot sizes of $w_0 \leqslant (2/k_p)\sqrt{a_0}$. Using a 2D analytical model, W. Lu et al. found that wakefield excitation is strongest for $a_0 \geqslant 4$, leading to a nearly spherical bubble with a radius of

$$r_b \simeq (2/k_p)\sqrt{a_0}, \qquad (2.21)$$

[48]. Blowout also occurs for laser intensities of $2 \lesssim a_0 \lesssim 4$ but the cavity does not have a perfectly spherical shape [48]. The analytical model of the blowout regime is commonly used to derive the scaling laws of laser-plasma acceleration since it was found to agree well with experimental data as well as Particle-In-Cell simulations. The scaling laws and limitations of laser-plasma acceleration are discussed in section 2.3.4.
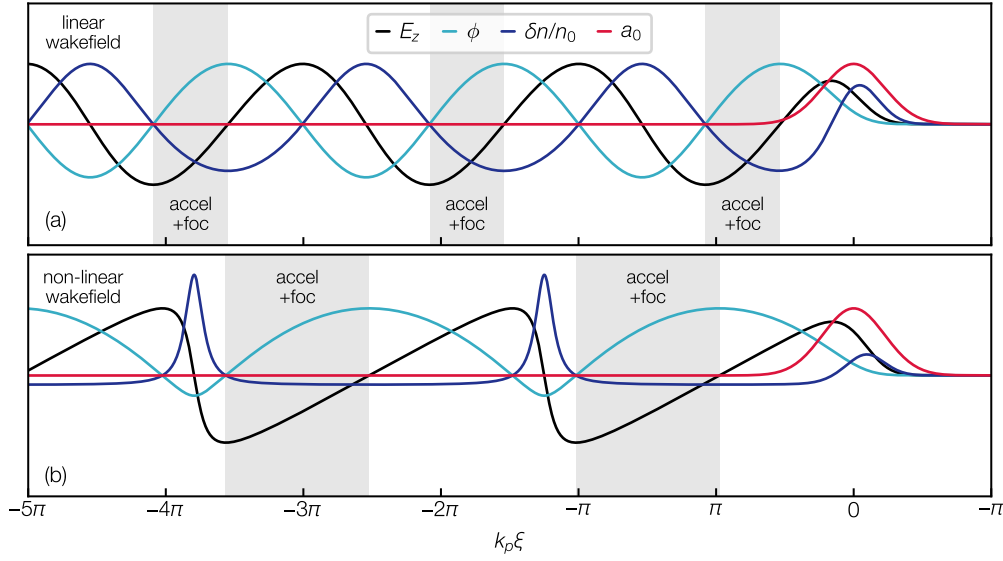
Figure 2.4 – Wakefield parameters in the linear, $a_0 \ll 1$, (a) and non-linear, $a_0 \gg 1$, (b) regime of laser-plasma acceleration. Figures show the laser intensity a_0 (red), the scalar potential of the wakefield ϕ (light blue), the normalized electron density modulation $\delta n/n_0$ (blue) and the laser electric field E_z (black), derived from eq. (2.16) and eq. 2.18, respectively. The gray shaded areas indicate the regions where accelerating and focusing fields are present. The wakefield parameters are given in arbitrary units and the amplitudes are scaled for a better illustration.

2.3.2 Injection Schemes: Ionization Injection

Controlling the injection of electrons into the accelerating region of the wakefield is required to tune and enhance final electron beam parameters. The following section gives an overview of injection schemes and provides the theoretical background on ionization injection, the relevant injection scheme for the experimental campaign performed within this thesis, see chapter 7.

In general, it is aimed to trigger electron injection at preferred phase and longitudinal position in the plasma target. Injection or trapping refers to the process of electrons entering the accelerating region of the wakefield. This is challenging, since the phase velocity of the wakefield is equal to the laser group velocity and thus close to c, whereas the plasma electrons have little initial longitudinal momentum. For electrons to become trapped, it is thus required that they reach a velocity close to the phase velocity of the wakefield [17]. Several injection schemes have been proposed following mainly two approaches: either to increase the electron velocity or to decrease the phase velocity of the wakefield.

The most simple injection schemes is self-injection or wave breaking injection of plasma background electrons [22]. Injection occurs when the wakefield reaches the wave breaking limit and collapses. Electrons then gain enough momentum to be injected while scattering at the back of the bucket. However, self-injection only offers limited control over the electron beam parameters and lacks in stability due to its highly non-linear and statistical nature.

Actively increasing the electron velocity can be achieved with a counter-propagating laser pulse [27, 28]. A beat-wave pattern is formed at the collision point of the main driver and the auxiliary laser locally heating the background plasma and increasing the momentum of the electrons. This scheme allows to injected electrons at a preferred phase and reduces the transverse injection volume, but imposes a complex set up and alignment procedure.

Amongst the schemes employed to reduce the phase velocity of the wakefield are density down-ramp and shock-front injection [24, 25]. Here, the correlation between the plasma wavelength and the electron density $\lambda_p \propto 1/\sqrt{n_e}$ is utilized to elongate the wakefield in negative density gradients. Thus, the phase velocity of the wakefield locally decreases at the back of the bucket and electrons are more easily trapped. These density gradients can be created either with specially designed capillary type plasma targets or by inserting a knife edge into a gas jets type plasma target. The typically small longitudinal injection distance minimizes phase variations and thus the energy spread.

A simple to implement scheme allowing to control the injection phase is called ionization injection [30–32]. By adding a small fraction of a high-Z gas to the low-Z gas forming the plasma background, injection of inner shell electrons of the high-Z gas is localized to the peak intensity of the laser pulse. In the experiments presented in chapter 7, the plasma was formed from a hydrogen-nitrogen gas mixture. Nitrogen was chosen because of the large gap in the ionization potential between the L-shell electron, N^{5+}, and the first K-shell electron, N^{6+}. In section 2.2, it was shown that the five nitrogen L-shell electrons are ionized with a laser strength parameter of $a_0 \simeq 0.08$, which is immediately reached by the leading edge of the laser pulse, for typical laser intensities of $> 10^{18}\,\mathrm{Wcm}^{-2}$. These electrons are not born at the correct phase for injection and only contribute to the background plasma forming the wakefield. The two K-shell electrons, on the other hand, require a laser strength parameter of $a_0 \simeq 2$ and $a_0 \simeq 2.7$, which are only reached at the intensity peak of the laser. As they are born inside the wakefield structure, they gain enough momentum while traversing to the back of the bubble and are trapped. This does not only reduce the intensity threshold for trapping compared to self-injection, but also allows to directly control the amount of injected charge with the concentration of the high-Z gas [49].

Principles of Ionization Injection

The following discussion closely follows the theory given by J. Faure et al. in [50]. It is restricted to a 1D description where only electron motion in the longitudinal direction z, at a position $\xi = z - v_g t$ behind the laser pulse is considered. Furthermore, the non-linear regime of laser-plasma acceleration, $a_0 \gg 1$, is assumed. The scalar potential ϕ is given by eq. (2.18). The laser pulse is represented by its normalized vector potential a, see eq. (2.3).

The Hamiltonian describing the electron trajectory in phase space reads

$$H = \sqrt{1 + u_\perp^2 + u_z^2} - \beta_p u_z - \phi(\xi),$$
$$u_\perp = p_\perp/m_e c, u_z = p_z/m_e c, \tag{2.22}$$

where $u_\perp$ and u_z are the normalized transverse and longitudinal momenta and $\beta_p = v_p/c$. It is convenient to introduce the canonical momentum $\vec{P} = \vec{p} + q\vec{A}$. In normalized units $\vec{P}$ is denoted by $\vec{U} = \vec{P}/m_e c$ and it follows since the laser pulse only has transverse component in the 1D limit that $U_z = u_z$ and $U_\perp = u_\perp - a$. Inserting these correlations into eq. (2.22) states the Hamiltonian

$$H = \sqrt{1 + (U_\perp + a)^2 + u_z^2} - \beta_p u_z - \phi(\xi). \tag{2.23}$$

The transverse canonical momentum is conserved in 1D, i.e.

$$\dot{U}_\perp = -\frac{\partial H}{\partial r_\perp} = 0 \rightarrow u_\perp(\xi) - a(\xi) = \text{const.} \tag{2.24}$$

Eq. (2.24) shows that the Hamiltonian is time independent which implies that electrons move on trajectories where the energy of the system is conserved. The longitudinal momentum u_z of an electron with an initial energy H_0, as a function of the wakefield potential ϕ, is found from

$$u_z = \beta_p \gamma_p^2 (H_0 + \phi) \pm \gamma_p \sqrt{\gamma_p^2 (H_0 + \phi)^2 - \gamma_\perp^2}, \tag{2.25}$$

with $\gamma_p = (1 - v_p^2/c^2)^{-1/2}$ the Lorentz factor and $\gamma_\perp{}^2 = 1 + u_\perp^2$. For a known laser vector potential $a(\xi)$ and wakefield potential $\phi(\xi)$, eq. (2.25) gives the electron trajectory in phase-space. The characteristic electron trajectories are shown in the lower plot in figure 2.5. Depending on its initial position ξ and energy H_0, an electron moves either on open (gray lines) or closed (dashed green lines) orbits, which are separated by the so called separatrix (red line). Open orbits are also referred to as cold fluid orbits and correspond to electrons being initially at rest in front of the laser pulse with $u_z(\xi_i) = u_\perp(\xi_i) = 0$

and $H_0 = 1$. These electrons are not trapped by the wakefield and only contribute to the plasma background. The Hamiltonian on the separatrix is given where $H(\gamma_s, \xi) = H(\gamma_p, \xi_{min})$ and reads

$$H_s = \gamma_\perp(\xi_{min})/\gamma_p - \phi_{min}, \tag{2.26}$$

with $\phi_{min} = \phi(\xi_{min}) < 0$. An electron moves on a closed orbit and is trapped by the wakefield for $H \leqslant H_s$. Considering an initially warm plasma behind the laser pulse with a thermal momentum of $u_t < 1$ and $H = H_t \sim 1 - \beta_p u_t$, trapping occurs for

$$\phi_{min} \leqslant -1 + \gamma_p^{-1} + \beta_p u_{th}, \tag{2.27}$$

[33]. Following these considerations, the trapping conditions for electrons born inside the laser field, as it is the case in ionization injection, can be derived. The transverse canonical momentum of an electron born at rest and phase ξ_{ion} inside a laser field reads $u_\perp(\xi) = a_\perp(\xi) - a_\perp(\xi_{ion})$. In case an electron is born at the peak of the laser field $a_\perp(\xi_{ion}) = 0$ and the momentum is reduced to $u_\perp \simeq a_\perp(\xi)$. However, some electrons will be born off-peak with a finite $a_\perp(\xi_{ion})$ if the laser intensity exceeds the ionization potential of the electron. Thus, $a_\perp(\xi_{ion}) \neq 0$ which results in an additional transverse momentum gained by the electron from the laser field. Its Hamiltonian is found from eq. (2.22), i.e.

$$H_{ion} = \gamma_\perp(\xi_{ion}) - \phi(\xi_{ion}) = 1 - \phi(\xi_{ion}). \tag{2.28}$$

After the electron leaves the laser field, it is $\gamma_\perp = (1 + a_\perp^2(\xi_{ion}))^{1/2}$. Considering the beforehand derived necessary condition of $H_{ion} \leqslant H_s$, the trapping condition for the phase of ionization induced electron trapping reads

$$\phi_{min} - \phi(\xi_{ion}) \leqslant \frac{\gamma_\perp}{\gamma_p} - 1 = \frac{(1 + a_\perp^2(\xi_{min}))^{1/2}}{\gamma_p} - 1. \tag{2.29}$$

Here, it was assumed that the electron is trapped behind the laser pulse, i.e. $a_\perp(\xi_{min}) = 0$. The left side of the in-equation can be related to the maximum energy an electron gains after being ionized and traversing to the rear of the bucket. For typical parameters of interest, i.e. $\gamma_p > 10$, $\Delta\phi = \phi_{min} - \phi(\xi_{ion}) \leqslant -1$. The second trapping condition is that the laser pulse has to be intense enough to ionize the inner shell electrons of the high-Z gas. In case of nitrogen, this states an intensity threshold of $a_0 \sim 1.4$ and hence requires the operation in the non-liner regime of laser-plasma acceleration.

The top plot in figure 2.5 shows the region within the longitudinal laser intensity envelope where the first nitrogen K-shell electrons N^{6+} are ionized and fulfill the former mentioned trapping conditions. First injection occurs for electrons born at phase $\xi_{ion,1}$, i.e. as soon as the laser intensity exceeds the ionization potential of the electrons and $\Delta\psi \leqslant -1$. Both trapping conditions are fulfilled for electrons born within the green shaded area. Injection stops when the laser intensity has decreased below the ionization potential at phase $\xi_{ion,2}$. Exemplary phase-space trajectories of electrons born at phase $\xi_{ion,1}$ and $\xi_{ion,2}$ are shown alongside the separatrix and the cold fluid orbits in the bottom plot of figure 2.5.

It is noted that injection only stops in the co-propagating frame of the laser pulse but not in the longitudinal direction along the plasma target. Electrons are injected continuously when the high-Z gas is present and the laser intensity sufficiently high to ionize the inner shell electrons. As a result, electron beams generated with ionization injection typically show a low-energy tail. The longitudinal injection dynamics of ionization injection are discussed with PIC simulations in chapter 5.
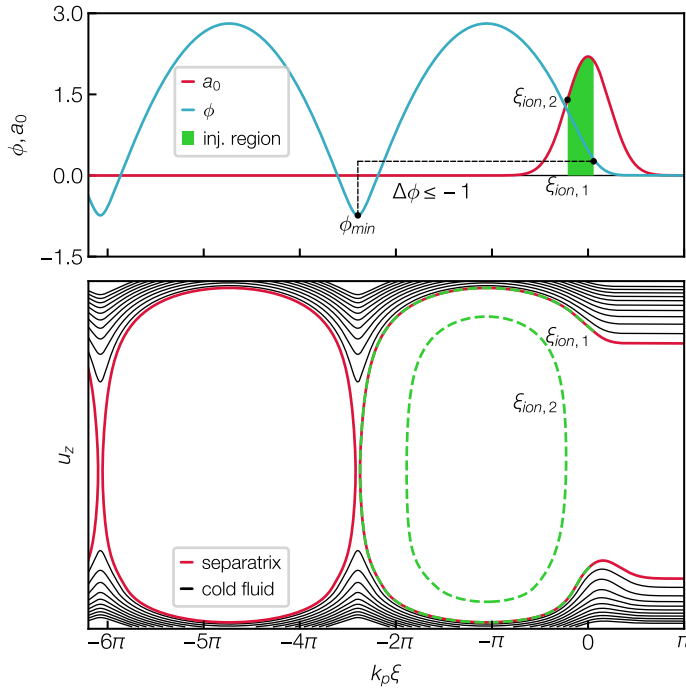
Figure 2.5 – Longitudinal laser intensity envelope for $a_0 = 2.2$ (red) and wakefield potential ϕ (blue) in the non-linear regime of laser-plasma acceleration, with $\gamma_p = 30$ and $n_e = 3 \times 10^{18}\,\mathrm{cm}^{-3}$ (top plot). Nitrogen K-shell electrons born between phase $\xi_{ion,1}$ and $\xi_{ion,2}$ (green shaded area) are ionized at the correct phase and are trapped by the wakefield. Phase-space trajectories of trapped electrons (dashed green), un-trapped electrons (black) and electrons on the separatrix (red) are shown in the bottom plot. Figure is reproduced from [50].

2.3.3 Beam Loading

Laser-Plasma Accelerators can generate nanocoulomb class electron bunches with fem-
tosecond duration leading to kilo ampere peak currents [6, 7]. At such high currents,
the space charge field of the electron bunch drives its own wakefield superimposing and
modulating the laser wakefield. This effect is known as beam loading and imposes a limit
on the accelerated charge, energy gain, and beam quality.

A 1D analytical description of beam loading was first introduced by T. Katseouleas et
al. in [51]. It was found that for a uniform transverse bunch distribution much larger
than c/ω_p, the number of particles which can be loaded into the wakefield before the
acceleration field is canceled out reads

$$N_{max} = \frac{n_0 A_b}{k_p} \frac{E_z}{E_0} \simeq 5 \times 10^5 \frac{E_z}{E_0} A_b \left[\text{cm}^{-2}\right] \sqrt{n_0 \left[\text{cm}^{-3}\right]}, \tag{2.30}$$

where A_b is the cross section of the bunch, n_0 the unperturbed electron density and
E_z/E_0 the normalized electric field. For $N_e = N_{max}$, a beam loading efficiency of $100\,\%$
is reached and the energy of the wakefield completely absorbed by the bunch.

A more vivid, 3D description of beam loading in the framework of laser-plasma acceler-
ation in the blow-out regime, valid for $a_0 \gtrsim 2$, was given by W. Lu et al. in [52]. They
investigated beam loading in the self-injection regime with a theoretical model and PIC
simulations. Expressed in practical units, the maximum number of electrons which can
be accelerated is given by

$$N_{max} \simeq 2.5 \times 10^9 \frac{\lambda_l \left[\mu\text{m}\right]}{0.8} \sqrt{P\left[\text{TW}\right]/100}, \tag{2.31}$$

where P is the laser power. The longitudinal half-width bunch length in their simulations
was $\sim 1c/\omega_p$. It is seen that the number of electrons which can be accelerated depends on
the laser power. For the LUX accelerator driven by the ANGUS laser system with a peak
power of $200\,\text{TW}$ and a central wavelength of $800\,\text{nm}$, eq. (2.31) predicts a maximum
bunch charge of $\sim 0.6\,\text{nC}$.

For an unshaped bunch distribution, a fully loaded wakefield results in a large spread in
energy gain across the bunch length. While electrons located at the head of the bunch
experience the undisturbed wakefield and gain high energies, electrons located at the
tail of the bunch experience the perturbed wakefield and gain less energy or are even
decelerated. Thus, the energy chirp of the bunch increases. This can be overcome by
properly shaping the witness bunch such that the charge density decreases from the head
towards the tail and thus matching the longitudinal electric field gradient of the wakefield.

However, this technique requires external electron injection combined with complicated bunch shaping.

In case of internally injected plasma background electrons, the beam quality can be enhanced by properly loading the wakefield. For an optimum amount of injected charge, the wakefield driven by the electron bunch and the laser wakefield are balanced such that the accelerating field along the bunch length becomes constant. Electrons situated in the head and tail of the bunch thus experience the same electric fields and thus gain similar energies. Figure 2.6 illustrates beam loading at different longitudinal positions along the plasma target with PIC simulations.

The inset plot in each panel shows the modulation of the longitudinal electric field E_z by the electron bunch. The unloaded wakefield at an early stage of the laser-plasma interaction where the cavity starts to form and first electrons are trapped is shown in figure 2.6a. Beam loading is first visible in figure 2.6b, where the gradient of the electric field starts to become reduced. Optimum loading is achieved in figure 2.6c with a nearly constant electric field and thus energy gain across the bunch length. Figure 2.6d depicts the overloaded case with a strongly modulated electric field. Simulations also reveal that not only the slope of the electric field is modulated but also its amplitude reduced. Thus,
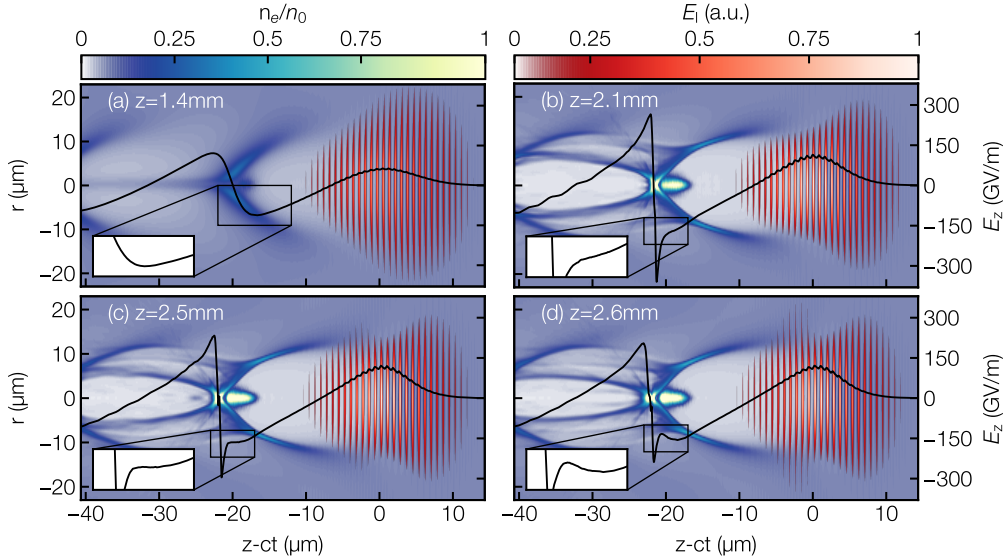
Figure 2.6 – PIC simulation of ionization injection illustrating beam loading effects. The panels (a-d) show the electron density modulation (background), the laser electric field (red) and the beam loaded electric field E_z (black) at different longitudinal positions z along the plasma target. Panel (a) corresponds to position $z = 1.4\,$mm, panel (b) to $z = 2.1\,$mm, panel (c) to $z = 2.5\,$mm and panel (d) to $z = 2.6\,$mm in the plasma density profile derived from CFD simulations, see figure 4.5. Simulation parameters: $E_p = 3.5\,$J, $\tau = 35\,$fs (FWHM), $w_0 = 26\,\mu$m (FWHM), $n_e = 2.3 \times 10^{18}\,$cm^{-3}, nitrogen concentration of 0.5 %.

electron energy gain decreases with increasing bunch charge when operating in a beam loaded regime. Experimental results presented in chapter 7 confirm these assumption.

As beam loading modulates the wakefield structure and hence determines the final electron beam quality, it is necessary to control beam loading effects via the amount of injected charge. Experimental results presented in section 7.4 will show how to tune the bunch charge in the ionization injection scheme with the concentration nitrogen added to the plasma background.

2.3.4 Scaling Laws and Limitations

In the non-linear regime of laser-plasma acceleration for $2 \lesssim a_0 \lesssim 4$, electron energy gain scales with the average longitudinal electric field $E_{z,\text{avg}}$ and the acceleration length L_{acc} according to

$$\Delta E = q E_{z,\text{avg}} L_{\text{acc}}, \tag{2.32}$$

$$\frac{e E_{z,\text{avg}}}{m_e c \omega_p} \simeq \sqrt{a_0}, \tag{2.33}$$

[52]. The effective acceleration length is limited either by laser diffraction, pump depletion or dephasing, depending on which effect is first reached [17].

The laser spot size evolves according to eq. (2.2), leading to a decrease in intensity and thus limiting acceleration due to diffraction to a few Rayleigh lengths. A pre-formed parabolic plasma channel either created with an additional laser pulse or a high-voltage discharge can be utilized to guide the laser beam over several Rayleigh lengths to increase the acceleration distance and hence electron energy gain [53, 54].

As the laser pulse propagates through the plasma it will subsequently transfer a large fraction of its energy into the wakefield, referred to as pump depletion. The distance on which the laser pulse looses its energy is given by

$$L_{pd} = \frac{\lambda_p^3}{\lambda_0^2} \times \begin{cases} 2/a_0^2 & a_0^2 \ll 1 \\ (\sqrt{2}/\pi)a_0 & a_0^2 \gg 1. \end{cases} \tag{2.34}$$

Electrons gain relativistic energies during acceleration and will eventually reach velocities exceeding the laser group velocity and thus outrun the wakefield. The propagation distance over which electrons slip from the back of the bubble into the decelerating phase of the wakefield is called dephasing length which is given by

$$L_{deph} = \frac{\lambda_p^3}{2\lambda_0^2} \times \begin{cases} 1 & a_0^2 \ll 1 \\ (\sqrt{2}/\pi)a_0/N_p & a_0^2 \gg 1, \end{cases} \tag{2.35}$$

where N_p is the number of plasma periods behind the laser pulse [55]. The characteristic length scales in the linear regime are $L_{pd} \sim 45\,\text{cm}$ and $L_{deph} \sim 2.8\,\text{cm}$ for typical laser-plasma parameters, i.e. $a_0 = 0.5$ and $n_e = 10^{18}\,\text{cm}^{-3}$ ($\lambda_p \sim 33\,\mu\text{m}$). In the non-linear regime for the same plasma properties but $a_0 = 2$, $L_{pd} \sim 5\,\text{cm}$ and $L_{deph} \sim 1\,\text{cm}$. Since $L_{pd} \propto n_e^{-3/2}$ and $L_{deph} \propto n_e^{-3/2}$, both the pump depletion length as well as the dephasing length can be increased by decreasing the electron density of the plasma.

2.4 Laser Modulation in Plasma

So far, the temporal and spatial properties of the laser pulse have been considered constant during propagation and wakefield excitation. This does not hold for high laser intensities, $a_0 \gg 1$, anymore. The non-linear refractive index of the plasma as well as the electron density modulation results in a transverse and longitudinal modulation of the laser pulse properties. The two major effects are relativistic self-focusing and self-compression [56, 57].

Self-Focusing
The dispersion relation of the plasma wave changes at high laser intensities due to the relativist mass increase of the electrons. The plasma frequency is modified to $\omega_{p,\text{rel}}^2(r) = (\omega_{p,0}/\gamma(r))n(r)/n_0$ and the refractive index is altered to

$$\eta_{\text{rel}}(r) \simeq 1 - \frac{\omega_{p,0}^2}{2\omega_l^2}\frac{n(r)}{n_0\gamma(r)} \tag{2.36}$$

with $\gamma(r)$ being the Lorentz factor and $n(r)$ the radial density profile [17]. Eq. 2.36 shows that the refractive index is altered by the density modulation as well as the relativistic factor. A Gaussian laser pulse with a radially decreasing intensity distribution thus sees a varying refractive index across its profile since $\gamma(r) \simeq (1 + a^2)^{1/2}$. The refractive index is maximum on-axis and decreases radially with the distance r. The phase velocity of the laser pulse is therefore lower on-axis than off-axis, resulting in a curved wavefront. The plasma thus acts as a focusing lens, reducing the spot size and counteracting diffraction to some extend.

The laser power required for relativistic self-focusing can be approximated in practical units by

$$P_c\,[\mathrm{GW}] = 17.4(\omega_l/\omega_p)^2. \tag{2.37}$$

A laser pulse diffracts if $P < P_c$ and focused if $P > P_c$ [58]. For a typical electron density of $n_e = 1 \times 10^{18}\mathrm{cm}^{-3}$ and a laser wavelength of 800 nm, the laser power required for self focusing is $\sim 30\,\mathrm{TW}$. Electron beams were generated with laser powers between 50 TW and 70 TW in the experimental campaign presented in chapter 7. Thus, self-focusing is expected to occur. The longitudinal evolution of the laser spot size and the laser intensity in the plasma target designed within this thesis is discussed with PIC simulations in section 5.2.

Self-Compression
The laser pulse further experiences a longitudinally altered plasma density and hence refractive index. The leading edge of the laser pulse travels in regions of higher electron density, whereas the rear is located inside the ion column where most of the plasma electrons are expelled. The distance between the wavefronts thus increases during propagation, which causes a frequency up-shift, often referred to as red-shift [17]. The group velocity, on the other hand, decreases with increasing electron density, causing the end of the pulse to catch up. The pulse therefore is compressed during propagation. In a similar way than self focusing, this can increase the intensity significantly.

3 Experimental Design

Experiments on electron beam generation with ionization injection performed within this thesis have been carried out at the Laser-driven Undulator X-ray source LUX in Hamburg, Germany. This section covers the experimental setup and introduces the relevant laser and electron beam diagnostics. First, an overview of the beamline is given in section 3.1, followed by a description of the driver laser system ANGUS and its diagnostics in section 3.2. The electron beam optics is discussed in section 3.3. The diagnostics for electron beam energy, charge and transverse beam profile are presented in sections 3.4, 3.5 and 3.6. The plasma target is discussed in detail in the following chapter, see 4.

3.1 LUX Electron Beamline Overview

The LUX electron and X-ray beamline combines the relatively young research topic of laser-plasma acceleration and the knowledge, as well as equipment of state of the art conventional accelerators into a complex laser-plasma driven light source [59]. A schematic of the beamline and the main components are shown in figure 3.1.

The compressed laser pulses from the 200 TW peak power laser system ANGUS are guided by a 30 m long transport beamline (not shown in the figure) from the top floor of the building into the accelerator tunnel located in the basement. The laser beam is coupled into the final-focusing chamber with two motorized mirrors, which are further used to align the beam onto its design axis. The final-focusing chamber is equipped with an off-axis parabolic mirror (parabola) with a focal length of 2025.4 mm. The laser pulse properties are optimized and characterized at the beginning of an experimental campaign with an offline pre-target diagnostic setup. Laser pulse properties after the laser-plasma interaction are recorded online with the outcoupling diagnostic setup (OCD). The ANGUS laser system and the relevant diagnostics are discussed in section 3.2.

Electron beams are mostly generated with ionization injection in capillary type plasma targets with an acceleration distance between 4 mm and 10 mm. The generated electron beams typically have peak energies between 150 MeV and 800 MeV and bunch charges between 50 pC and 400 pC. The plasma target is operated with continuous gas flow to reduce gas pressure and hence density fluctuations for stable and reproducible electron

beam generation. The plasma target and the gas supply and diagnostic setup are introduced in chapter 4.

Electron beams are characterized with a set of diagnostics, including two cavity type beam position monitors (BPM1, BPM2) for non-invasive bunch charge and position measurement, two retractable electron screen stations (ESS1, ESS2) to measure beam pointing and transverse beam profile and a permanent magnet dipole spectrometer to resolve the energy spectrum. The electron beam diagnostics are presented in sections 3.4, 3.5 and 3.6.

The electron beam optics consists of a tunable high-gradient quadrupole doublet (Q_1, Q_2) used to focus the beam into the undulator or onto the various diagnostics to increase the resolution. In addition, four corrector dipoles (D_{1-4}) rae installed to align the electron beams onto the design axis and to compensate for initial beam pointing out of the plasma target. The electron beam optics is introduced in section 3.3.

A small period permanent magnet undulator can be driven into the electron beam path to generate X-rays. The X-rays are focused with a toroidal mirror into the spectrometer which is equipped with a transmission diffraction grating. The setup was used to generated spontaneous undulator radiation with wavelengths between 4 nm and 8 nm [60].
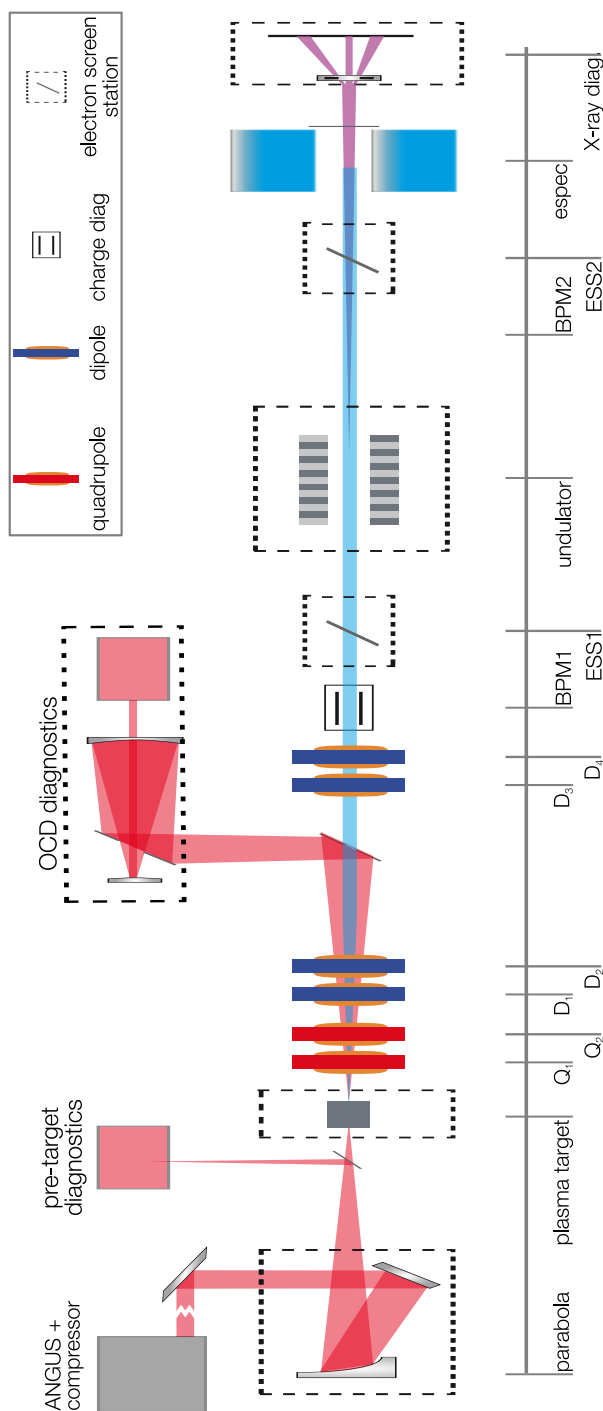
Figure 3.1 – Overview of the LUX electron and X-ray beamline. Laser pulses from the ANGUS laser system are focused by the parabola into a capillary type plasma target to generate electron beams. Laser pulse properties are measured and optimized with the offline pre-target diagnostic setup and the online, high power diagnostic setup (OCD). Electron beams are characterized with two cavity-type beam position monitors (BPM1, BPM2), two retractable electron screen stations (ESS1, ESS2) and a permanent magnet dipole electron spectrometer. The electron beam optics consists of a high-gradient quadrupole doublet (Q_1, Q_2) and four corrector dipoles ($D_{1,2,3,4}$). The X-ray section includes a short period undulator and a spectrometer equipped with a transmission diffraction grating. Image courtesy of Andreas R. Maier.

3.2 ANGUS Laser System

The Ti:Sapphire laser system ANGUS is utilized as a driver for the electron beam generation at LUX. The system is based on Chirped Pulse Amplification (CPA) and is capable to deliver a peak power of 200 TW at 5Hz repetition rate [61]. Measurements performed by V. Leroux et al. showed that the diffraction grating pair in the pulse compressor deforms during operation at full specification. This alters the laser wavefront and worsens the spatial and temporal pulse quality [62]. The repetition rate was therefore decreased to 1 Hz in the experimental campaign conducted within this thesis. The five consecutive amplification stages of the system can be divided into two sections, the kHz and the 1 Hz section. The layout of the system and the pulse properties after each stage are illustrated in figure 3.2.

kHZ Section
Seed pulses from a mode-locked oscillator are first stretched and then amplified to 500 μJ in the regenerative amplifier REGEN and the repetition rate is decreased from 83 MHz to 1 kHz with a pulse picker. Laser pulses are then re-compressed before being sent into the XPW where cross polarized wave generation is used to improve the temporal pulse contrast by a few orders of magnitude [63]. Compression is necessary to reach the high intensities required for the non-linear process. Laser pulses with an energy of 40 μJ are then stretched again and sent into the pulse shaper Dazzler [64]. This acousto-optic programmable dispersive filter diffracts individual spectral components of the pulse by exciting an acoustic wave in a crystal [65]. This allows to pre-compensate phase distortions acquired in the subsequent amplification stages and to online fine adjust the on-target temporal laser pulse properties. Laser pulses are then amplified in the BOOSTER to 50 μJ and the repetition rate decreased to 1 Hz. The REGEN as well as the BOOSTER are pumped by the diode based Nd:YLF laser JADE.

1 Hz Section
The 1 Hz section compromises three multi-pass amplification stages. The laser pulse energy is first increased to 30 mJ in the Pre-amplifier, then to 1.4 J in the first amplification stage AMP1. AMP1 is pumped with three flash lamp based Nd:YAG lasers. The final amplification stage AMP2 increases the pulse energy up to 5 J. AMP2 is pumped by the flash lamp based laser GAIA. An attenuator, made of a motorized waveplate and four thin film polarizers, is used to online tune the pulse energy by adjusting the rotation angle of the waveplate. The beam size is afterwards increased to ∼ 80 mm with an telescope and the beam sent onto a deformable mirror. A closed loop operation with the wavefront sensor installed in the pre-target laser diagnostics allows for wavefront optimization at the beginning of an experimental campaign. Laser pulses are then temporally re-compressed with a pair of diffraction grating in the pulse compressor and afterwards

coupled into the laser transport beamline. For a more detailed description of the system it is referred to [66].
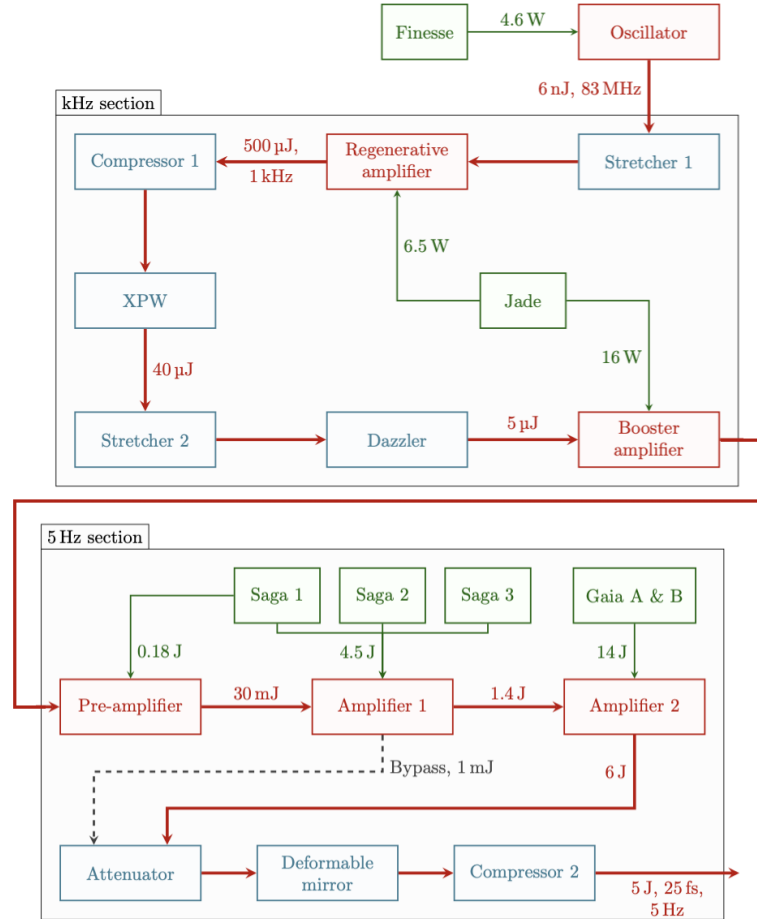
Figure 3.2 – Overview of the ANGUS laser system and laser pulse properties after each amplification stage. Figure taken from [66].

3.2.1 Laser Diagnostics

The laser diagnostics for the fully amplified beam are illustrated in figure 3.3. The laser beam is coupled into the pulse compressor with two motorized mirrors. A leak-through of the last mirror is used to monitor near- and far-field.

The diagnostic and the motorized mirrors are operated in a closed loop to automatically stabilize beam pointing into the pulse compressor. After compression, a fraction of the beam is sent out of vacuum and into a wavefront sensor to monitor online the wavefront
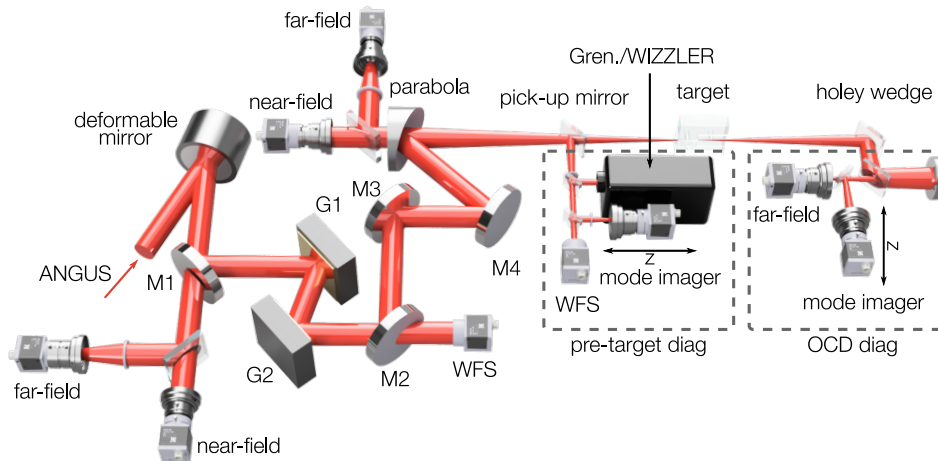
Figure 3.3 – CAD Rendering of the diagnostics for the fully amplified ANGUS laser beam. A leak-through of the last mirror (M1) in front of the pulse compressor (G1, G2) is used record near- and far-field. A wavefront sensor (WFS) online records the wavefront in high-power operation with a leak-through of the mirror M2. Mirrors M3 and M4 are used to align the laser beam onto the parabola. Laser Pointing into and transverse position in the beamline are recored with near- and far-field cameras installed behind the parabola. The pre-target diagnostic is used to characterize and optimize the focal spot quality. The outcoupling diagnostics (OCD) records the high-power laser properties after the laser-plasma interaction.

during high-power operation. The beam is then guided over a $\sim 35\,\text{m}$ long laser transport beamline to the electron beamline. Two motorized mirrors are used to align the beam onto the off-axis focusing parabola and towards the plasma target. A leak-through of the parabola is used to online monitor near- and far-field. The motorized mirrors (M3, M4) and the diagnostics are used to steer the electron beams by changing the pointing of the laser beam into the plasma target. The experimental results of the alignment procedure are presented in section 7.1.

Pre-Target Diagnostics
Prior to full power operation, the beam is sent out off vacuum and into the pre-target diagnostics setup to offline measure and optimize the focal spot quality of the fully amplified but attenuated beam. Two well characterized neutral density filters are therefore temporarily placed after the attenuator to further reduce the pulse energy to $1\,\text{mJ}$. Spatial laser diagnostics include a wavefront sensor and a mode imager. The wavefront sensor is connected to the deformable in the laser system. A closed loop operation allows the deformable mirror to correct wavefront aberrations originating from the beam transport and to optimize focal spot quality. The deformable mirror is further used to shift the longitudinal focus position in the target chamber by manually adjusting the divergence of the beam. The mode imager consists of a CCD camera and a 4-fold microscope objective

mounted onto a linear translation stage. Images of the transverse laser beam profile are taken at several longitudinal positions in front and behind the focal plane to extract the focal spot size, the Rayleigh range, and the intensity evolution.

Temporal laser pulse properties are measured either with a Wizzler [67] or a GRENOUILLE [68]. The Wizzler relays on Self-Referenced Spectral Interferometry (SRSI) in which a reference pulse with a flat spectral phase and broad spectrum is generated from a fraction of the main pulse via cross-polarized wave generation (XPW) [69]. Both pulses are then overlapped with a small time delay in a spectrometer, resulting in a spectral interference signal from which the pulse properties can be obtained. The Wizzler offers high dynamic range and is used in combination with the pulse shaper Dazzler to adjust the compression of the beam and optimize the spectral phase in the beginning of an experimental campaign. The GRENOUILLE is based on frequency-resolved optical gating (FROG) [70]. The input beam is split into two beamlets with a Fresnel biprism which are then overlapped in space and time in a crystal for second-harmonic generation (SHG). The SHG signal is imaged onto a CCD camera which allows to reconstruct the pulse length, as well as spatial-temporal pulse properties. The GRENOUILLE is used to align the pulse compressor gratings with respect to each other to minimize pulse front tilt and spatial chirp, which can affect electron beam parameters and especially electron beam pointing, see section 7.1.

It s noted that the laser pulse properties are measured and characterize out of vacuum and that the beam therefore has to pass through a window. The window adds additional second-order phase distortions (GDD) which increases the pulse length. Therfore, GDD has to be subtracted with the DAZZLER for the optimization and added afterwards again to achieve shortest pulse length in-vacuum. In addition to phase distortions, the window as well as the other optical elements in the setup can introduce wavefront aberrations if not perfectly aligned. Thus, beam properties optimized out of vacuum must not necessarily correspond to optimized in-vacuum pulse properties. It can therefore be necessary to fine-tune the spectral phase with the DAZZLER to online optimize the electron beam parameters. An online optimization in high-power operation of the wavefront is so far not possible at LUX but is currently being implemented with an updated deformable mirror.

Post Plasma Interaction Diagnostics
The outcoupling diagnostic setup (OCD) allows to record the high-power laser properties after the laser-plasma interaction and is equipped with CCD cameras for near- and far-field detection, a spectrometer and an energy sensor. The far-field camera is mounted onto a linear stage similar to the pre-target diagnostics to measure the laser beam evolution around the focal plane.

3.2.2 Laser Pulse Properties

This section summarizes the optimized temporal and spatial laser pulse properties relevant for the experimental campaign presented in chapter 7. The data was recorded with the pre-target diagnostic setup introduced in the section before.

Spatial Laser Pulse Properties
A closed loop operation of the deformable mirror and the wavefront sensor was used to optimize the wavefront and a Strehl ratio of 0.84 was achieved. The laser intensity profile along the laser propagation direction z are shown in the horizontal x and vertical plane y in figures 3.4a and 3.4b, respectively. The data is reconstructed from a total of 100 images taken in steps of $\Delta z = 150\,\mu m$ with the mode imager. The horizontal and vertical FWHM beam size as function of z are derived from a 1D Gaussian function fitted to the projected signals of each image. Fitting the evolution of the beam waist, i.e. $w_z = w_0\sqrt{1 + (z/z_\mathrm{R})^2}$, to the beam size as a function of z yields a focal spot size of $(26.5 \pm 1.15)\,\mu m \times (24 \pm 1.6)\,\mu m$ and a Rayleigh length of $z_\mathrm{R} = (1.7 \pm 0.2)\,mm$.
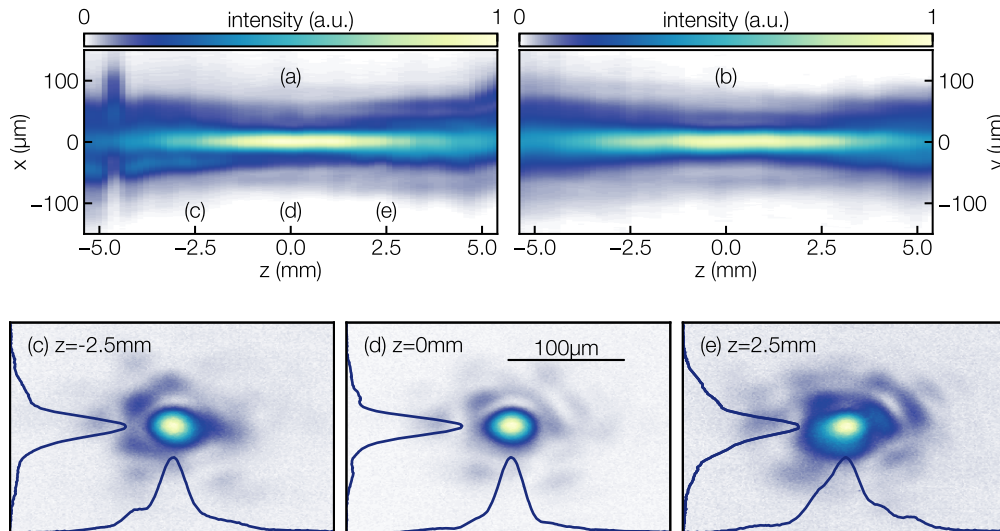
Figure 3.4 – Horizontal (a) and vertical (b) laser intensity profile in laser propagation direction z. Image of the transverse laser beam profile and the projected signals of the images (blue lines) taken 2.5 mm in front of the focal plane (c), in the focal plane (d) and 2.5 mm behind the focal plane (e). Data is taken with the mode image at a pulse energy of $\sim 1\,mJ$.

The transverse laser beam profile recorded 2.5 mm in front of the focal plane, in the focal plane and 2.5 mm behind the focal plane are depicted in figures 3.4c to 3.4e. The intensity is well confined within a radius of 150 μm, which is smaller than the capillary edge length of the plasma target of 500 $\mu m \times 500\,\mu m$. However, high dynamic range focal

spot measurements performed by V. Leroux revealed that the focal spot can show higher-order modes containing significant intensity on the level of $\sim 10^{15}\,\text{Wcm}^{-2}$ at a radius of $\sim 500\,\mu\text{m}$ [66]. In order to protect the plasma target from damage, a small ceramic plate with an inner diameter of $300\,\mu\text{m}$ is installed at its entrance to block those higher order spatial modes.

Temporal Laser Pulse Properties
Next, the beam was sent into the Wizzler to optimize the spectral phase. Using the former mentioned DAZZLER, second-order (GDD) and third-order (TOD) phase dispersion were adjusted to compress the pulses and to enhance the temporal phase contrast. Temporal and spectral laser pulse properties after optimization are summarized in figure 3.5.
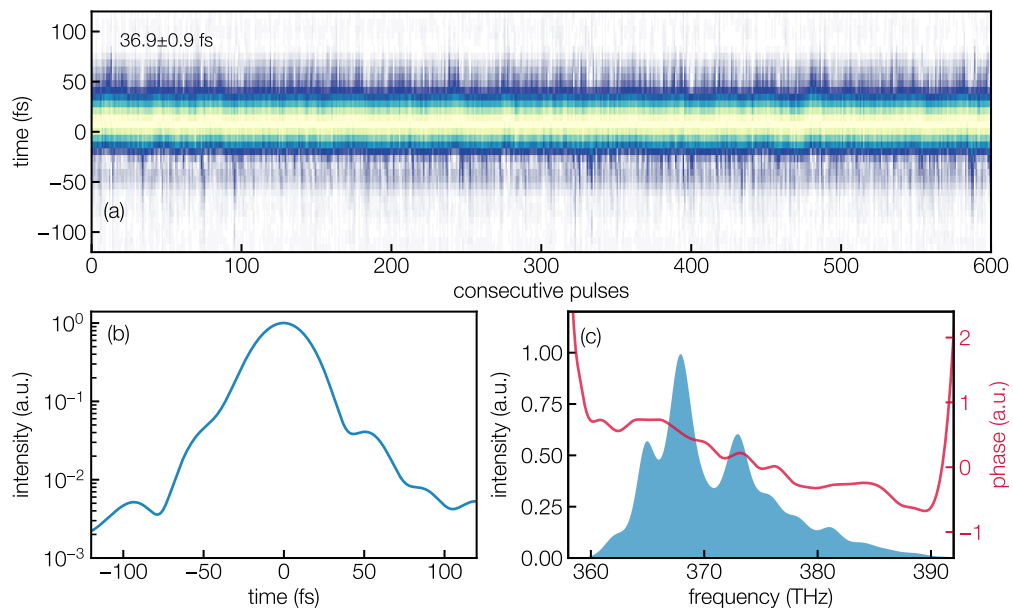
Figure 3.5 – Waterfall plot of the temporal laser intensity profile of 600 consecutive laser pulses recorded with the Wizzler (a) and corresponding normalized mean intensity profile (b). Laser pulse intensity in the frequency domain (blue) and spectral phase (red) (c).

A FWHM pulse duration of $(36.9 \pm 0.9)\,\text{fs}$ and a rms stability of $\pm 2.4\,\%$ were measured over 600 consecutive laser pulses, i.e. 10 minutes acquisition time. The Fourier-transform-limited pulse duration was $\sim 35\,\text{fs}$. The intensity profile in figure 3.5b shows a contrast better than 0.04 within $\pm 50\,\text{fs}$. The post pulse at $50\,\text{fs}$ is a result of the small ripples seen in the spectral phase in figure 3.5c. The linear slope in the phase does not affect the pulse duration, it only causes a shift in the arrival time of the pulse [71]. Spatial and temporal laser pulse properties are summarized in table 3.1.

The former section only names a small fraction of the implemented laser diagnostics but summarizes the most important detectors and laser pulse properties for this thesis.

Diagnostics for electron beam parameters are introduced in the following.

Table 3.1 – Spatial and Temporal on-target laser pulse properties measured at the beginning of the experimental campaign presented in chapter 7. The normalized vector potential a_0 is calculated with eq. 2.4 from the laser pulse energy measured in front of the pulse compressor, including a beamline transmission of $60\,\%$.

parameter	value
pulse energy E_l	$1.76\,\mathrm{J} - 2.85\,\mathrm{J}$
peak intensity I_0	$5.4 \times 10^{18}\,\mathrm{Wcm^{-2}} - 8.8 \times 10^{18}\,\mathrm{Wcm^{-2}}$
normalized vector potential a_0	$1.6 - 2$
focal spot size w_0	$(26.5 \pm 1.15)\,\mathrm{\mu m} \times (24 \pm 1.6)\,\mathrm{\mu m}$
Rayleigh length z_R	$(1.7 \pm 0.2)\,\mathrm{mm}$
pulse duration τ	$(36.9 \pm 0.9)\,\mathrm{fs}$

3.3 Electron Beam Optics

The LUX beamline is equipped with a high-gradient quadruple doublet and two sets of corrector dipoles for electron phase-space manipulation, beam transport and beam alignment. The quadrupoles, $Q_{1,2}$, are modified versions of XQA type magnets, initially developed for the european XFEL facility. Extra pole tips are attached to each magnet to reduce the gap size to $12\,\mathrm{mm}$ in the first quadrupole and to $22\,\mathrm{mm}$ in the second one to increase the magnetic field as well as to ensure a clip-free transmission of the post-plasma laser beam. Hall probe measurements performed by P. Winkler in [72] showed a maximum magnetic field gradient of $160\,\mathrm{T/m}$ for Q_1 and $80\,\mathrm{T/m}$ for Q_2, which allows to capture and focus electron beams with energies up to $450\,\mathrm{MeV}$. The four TCA type corrector dipoles, D_{1-4}, are installed pairwise and allow to compensate initial electron beam offset out of the plasma target and beam pointing into the beamline. The specification of the magnets are listed in table 3.2.

The quadrupole doublet was used during the experimental campaign to focus electron beams onto the spectrometer screen to reconstruct the transverse beam emittance and beam divergence. The technique is described in section 3.4.4 and the experimental results presented in section 7.5.

Table 3.2 – Specifications of the LUX electron beam optics. Focusing quadrupoles $Q_{1,2}$ and corrector dipoles D_{1-4} at longitudinal position z behind the plasma target.

element	specification	longitudinal position z (mm)	gap size (mm)
Q_1	$160.4\,\mathrm{T/m}$ at $180\,\mathrm{A}$	150	12
Q_2	$80.6\,\mathrm{T/m}$ at $180\,\mathrm{A}$	350	22
D_1	$150.2\,\mathrm{mT}$ at $3\,\mathrm{A}$	560	40
D_2	$129.4\,\mathrm{mT}$ at $3\,\mathrm{A}$	740	50
D_3	$150.5\,\mathrm{mT}$ at $3\,\mathrm{A}$	2110	40
D_4	$150.5\,\mathrm{mT}$ at $3\,\mathrm{A}$	2310	40

3.4 Electron Spectrometer

The energy spectrum of the laser-plasma accelerated electron beams is highly sensitive to laser and plasma properties. Beam energy as well as energy spread can be tuned with multiple parameters. Further, shot-to-shot variations on the spectrum can be present. A suitable electron spectrometer must therefore provide a large dynamic range with sufficient resolution and allow for single-shot measurements. The conceptual design and energy calibration of the LUX electron spectrometer is covered in section 3.4.1, followed by a discussion of the pointing and beam divergence limited resolution in section 3.4.2. Data post-processing is presented in section 3.4.3. Focusing the electron beam onto the spectrometer screen with the high-gradient quadrupole doublet allows to reconstruct the beam emittance and beam divergence in the horizontal plane, see section 3.4.4.

3.4.1 Design and Calibration

Design

The LUX electron spectrometer consists of a permanent magnet dipole mounted on top of a narrow vacuum chamber as shown in figure 3.6. The dipole is made out of four c-shaped yokes each equipped with 12 permanent magnets. It was originally designed by HZDR [73]. The total length of the dipole is $400\,\mathrm{mm}$ with a gap size of $40\,\mathrm{mm}$, resulting in a magnetic peak field strength of $\sim 0.95\,\mathrm{T}$. Electron beams enter the chamber and are vertically deflected by the magnetic field onto a $4\,\mathrm{cm} \times 80\,\mathrm{cm}$ large CAWO OG 16 scintillation screen which is directly glued to the 45 degree angled backside of the chamber [74]. The electron spectrometer has a high dynamic range covering energies between $25\,\mathrm{MeV}$ and $2.5\,\mathrm{GeV}$. The scintillation light is imaged over a mirror by two CCD cameras to reconstruct the energy spectrum. The full energy spectrum is detectable for a single shot.
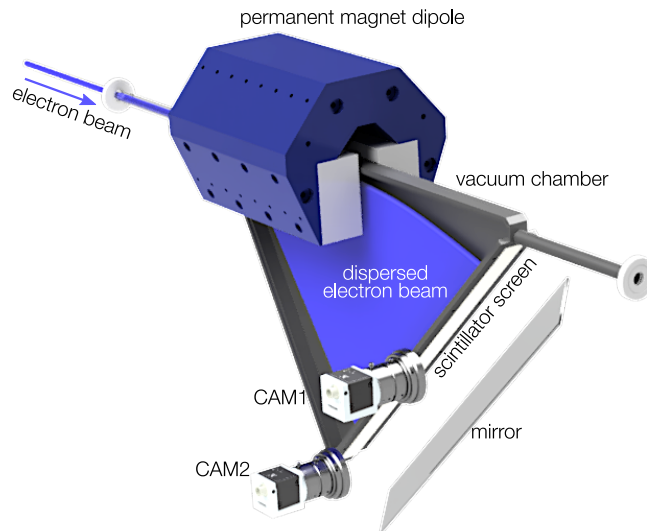
Figure 3.6 – CAD rendering of the LUX electron spectrometer. A 0.95 T peak field permanent dipole magnet (dark blue) is mounted on top of a narrow, triangular vacuum chamber. Electron beams are dispersed onto the spectrometer screen which is glued to the backside of the chamber. The scintillation light is collected with two cameras over a mirror. Simultaneously detectable energy range reaches from 25 MeV to 2.5 GeV.

Energy calibration

The working principle of the electron spectrometer is the energy dependent deflection of electrons in a magnetic field. An electron entering a dipole field will be deflected onto a curved trajectory with a radius ρ, given by

$$\frac{1}{\rho} = e \cdot \frac{B}{\gamma m_0 c},\tag{3.1}$$

with B being the magnetic field component perpendicular to the trajectory [75]. Electrons with higher energies are less deflected than electrons with lower energies and will hit a screen placed behind the magnetic field at a different position. The on screen position thus yields the electron energy for a known magnetic field strength. Eq. 3.1 is only valid for a single electron and an ideal homogeneous magnetic field with sharp edges. For a more precise calibration including fringe fields and inhomogeneities, the particle tracking algorithm ASTRA was used [76]. Electrons with energies between 25 MeV and 2.5 GeV were tracked through the measured 3D magnetic field map onto a screen. The distance and angle between dipole exit and screen corresponded to the actual setup. The main component of the magnetic field B_x and exemplary trajectories of electrons with different energies are shown in figure 3.7a.
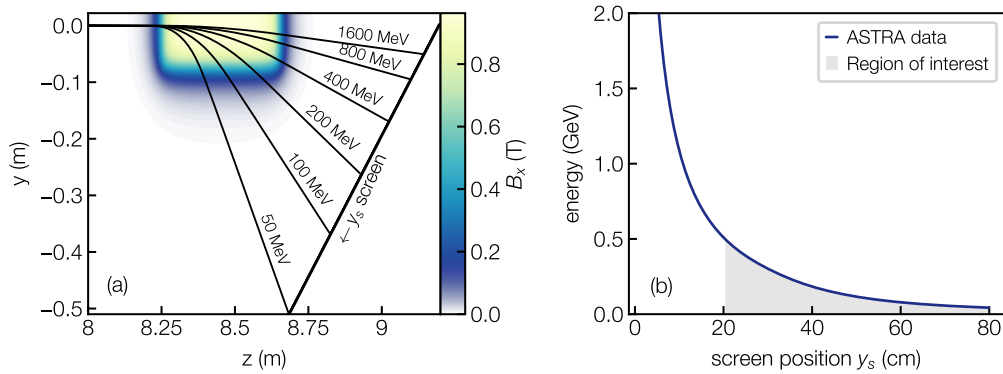
Figure 3.7 – ASTRA simulated trajectories for electrons with different energies in in the dipole field of the electron spectrometer (a). Spectrometer Screen position to energy calibration (b). The gray shaded area indicates the energy range relevant for this thesis between 50 MeV and 500 MeV.

The deduced correlation between screen position and electron energy is shown in figure 3.7b. The high dynamic range comes with the expense of resolution for higher energies if the beam is not focused onto the spectrometer screen with the quadrupole double. When using the quadrupole doublet, the resolution of the focused energy is on the order of 0.1 %. The relevant energy range between 50 MeV and 500 MeV for the experimental campaign presented in chapter 7 is indicated with the gray shaded area. The spectrometer resolution for unfocused electron beams in this energy range is discussed in the following section 3.4.2.

A charge calibration of the spectrometer screen was not available during the experimental campaign. The charge density of the electron beams can hence only be given in relative units. To measure the total bunch charge, two cavity type beam profile monitors (BPMs) are installed in the LUX beamline, see section 3.6.

3.4.2 Spectrometer Resolution

The resolution and accuracy of the electron spectrometer depend on the beam energy, beam divergence and beam pointing, i.e. the electron beam direction into the spectrometer. The spectrometer assembly is placed 8.2 m behind the exit of the plasma target and has an entrance aperture with a diameter of 22.1 mm. This yields an acceptance angle of 2.48 mrad (full angle). For a larger beam divergence and/or beam pointing only the core part of the electron beam is sampled onto the spectrometer screen. The resolution of the spectrometer was investigated with a matrix formalism, commonly used to track particles through an accelerator. The following discussion closely follows the theory given in [77].

An electron is represented by the vector $X = (x, p_x, y, p_y, \delta l, \frac{\Delta z}{p_0})$, where x and y are the horizontal and vertical coordinates, p_x and p_y the corresponding canonical momenta, δz the path length difference from the reference particle and $\frac{\Delta p}{p_0}$ the central momentum deviation. Using a series of linear transformations, the electron can be translated section wise from its initial position i to a final position s by

$$X_s = M_n \cdot M_{n-1} \cdots M_1 \cdot X_i, \tag{3.2}$$

where M_n are 6×6 transport matrices, each representing a specific element of the accelerator, for example a free drift section or the various beam optical elements. The transport matrix of the spectrometer was obtained via particle tracking with ASTRA to fully describe the electron beam dynamics through the spectrometer dipole including the fringe field effects and path lengths for all considered energies. Electron beams with various mean energies, beam divergence and beam pointing were generated and tracked through the measured 3D magnetic field map on the spectrometer screen in a similar way than for the energy calibration. The individual matrix elements are then deduced from the correlation between input and on-screen electron parameters. The final matrix does not only include fringe fields but also edge-focusing effects which act focusing in the vertical and de-focusing in the horizontal plane. For the LUX electron spectrometer, this results in a demagnification of the electron beam in the vertical plane by a factor of 2-3 a magnification on the horizontal plane also by a factor of 2-3.

Matrices were also constructed for the other beam optical elements in the LUX beamline, i.e. the quadrupole doublet and the corrector dipoles. Thus, by multiplying the individual matrices according to eq. 3.2, the electron beams can be tracked from the plasma target to every position in the LUX beamline. For a more detailed discussion on the tracking formalism for the LUX beamline it is referred to [78, 79].

Spectrometer Resolution: Beam Pointing and Beam Divergence
Delta peak like energy distributions between 50 MeV and 500 MeV, each consisting out of 10^7 individual electrons have been tracked from the plasma target onto the spectrometer screen to estimate the beam pointing and divergence dependent resolution.

Figure 3.8a shows that vertical beam pointing into the spectrometer causes an energy shift. The beam divergence in both planes was 1.5 mrad for all generated electron beams. Beam pointing into the spectrometer causes a shift on the spectrometer screen thus resulting in an energy shift. The energy resolution at 264 MeV is independent of beam pointing as electrons are directly imaged onto the spectrometer screen. Electrons with energies below 264 MeV and negative pointing are shifted towards lower energies while electrons with positive pointing are shifted towards higher energies. For electrons with energies above 264 MeV, the effect is reversed and positive pointing causes a negative

shift and vice versa. The relative energy resolution depending on the beam divergence is shown in figure 3.8b.

The mono energetic input peak becomes broadened with increasing beam divergence as the beam size in the dispersive plane of the spectrometer is larger and the resolution hence less. The resolution further decreases for electrons with energies smaller and larger than 264 MeV which are not perfectly imaged onto the spectrometer screen.
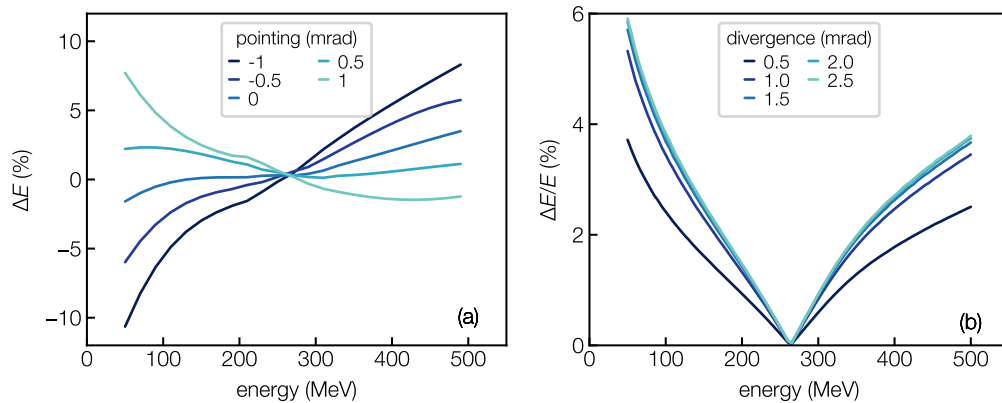
Figure 3.8 – Electron spectrometer resolution depending on electron beam pointing (a) and beam divergence (b).

Electron beams generated within the experimental campaign presented in chapter 7 have a high-energy peak between 200 MeV and 360 MeV, a relative energy spread from 12 % to 30 % and a beam divergence between 0.5 mrad and 2.5 mrad. Thus, the energy resolution for the relevant part of the energy spectrum, without focusing the beam, is limited to $\sim 4\,\%$. As mentioned before, when focusing, the energy resolution is on the oder of $\sim 0.1\,\%$.

3.4.3 Imaging System and Data Processing

The scintillation light of the spectrometer screen is collected with two Basler acA2000-50gm [80] CCD cameras with a chip size of 2048×1088 px, each equipped with a KOWA LM12HC ($f = 12.5$ mm) objective [81]. The two cameras (CAM1, CAM2) are positioned such that camera one covers the low energy range from 50 MeV to 175 MeV and camera two the high energy range from 108 MeV to 814 MeV. Figure 3.9 shows the raw images of each camera with electron signal. The region of the images from which the energy spectra are reconstructed is indicated with the red box. It is seen that the electron signal exceeds this region in the non dispersive plane x. This part can not be taken
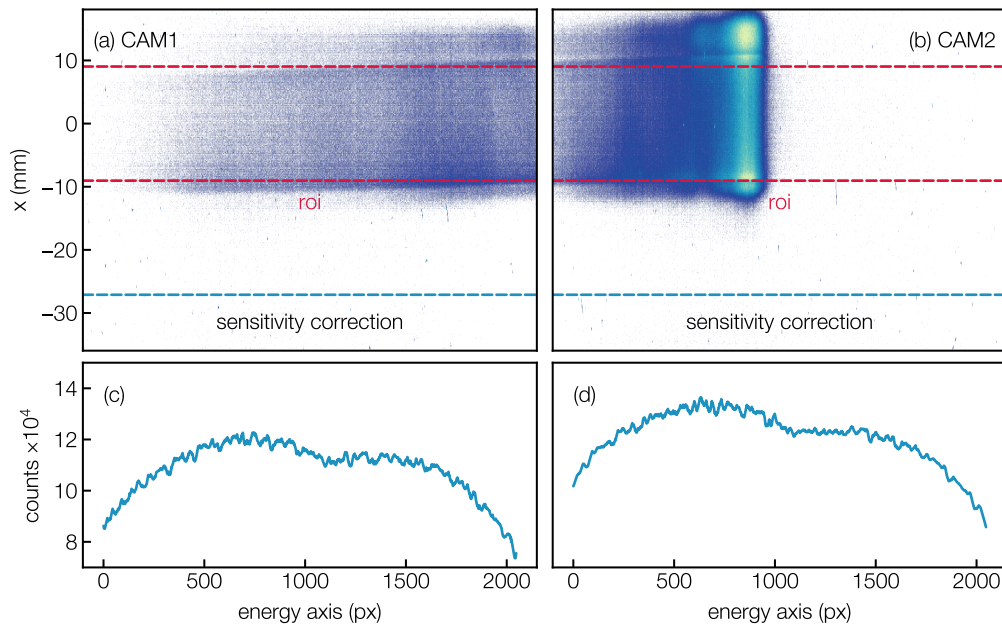
Figure 3.9 – Raw spectrometer screen image with electron beam signal recorded with CAM1 (50 MeV to 175 MeV) (a) and with CAM2 (108 MeV and 814 MeV) (b). The red boxes indicate the region of interest for the reconstruction of the energy spectrum. Projected signal along the dispersive plane of the spectrometer for CAM1 (c) and CAM2 (d). The blue boxes show where the signal is taken to correct for the insensitivity of the CCD chip.

into account as it corresponds to the edges of the vacuum chamber where the welding is located. The chamber is unevenly thick in this region and electrons are scattered. This also explains the spots with increased intensity at $x = 11$ mm and $x = $-10 mm in the image of CAM2. The non-dispersive plane of the spectrometer shows the beam divergence. As the screen is comparably small and the electron spectrometer positioned ~ 8 m behind the plasma target, the signal of high divergent electrons is outside the region of interest. The reconstructed spectra of unfocused beams thus only corresponds to the core of the beam. When focusing the beams with the quadrupole doublet onto the screen, the whole electron signal is inside the region of interest. The bunch charge is measured with two cavity type beam position monitors and therefore not affected by the loss of electrons, see section 3.6.

The two cameras have a non flat electric sensitivity such that the intensity of the projected background, without electron signal, varies across the image, see figures 3.9c and 3.9d.

The projections are taken from the blue regions in figure 3.9a and figure 3.9b. The counts of the background signal decrease by nearly 40 % towards the edges of the chip and both curves show a small dip around pixel 1200. In addition, the background inhomogeneity varies from shot-to-shot. The camera sensitivity also applies to the electron signal and

therefore has to be de-convoluted to retrieve the pure electron signal proportional to the charge density. In particular to retrieve the same signal in the overlap region of the camera field of view.

To account for these inhomogeneities, background images without electron beam signal are taken and normalized. These normalized background images are then rescaled to the mean count, taken from the blue boxes in figures 3.9a and 3.9b, for each image containing an electron signal. The raw images are then divided by those modified background images. The individual steps of the post-processing are exemplary shown in figure 3.10.

Figure 3.10a shows the projected raw signal of both cameras images. The spectra after the former mentioned sensitive correction are shown in figure 3.10b. A baseline is subtracted to remove remaining electronic noise and the spectra stitched together in the overlap region. The resulting energy spectrum is shown in figure 3.10c. The scintillation signal has to be wighted such that the counts per pixel on the camera correspond to counts per energy interval. This is necessary since the electron energies are unevenly mapped onto the linear axis of the CCD cameras by the spectrometer dipole. Therefore, the energy spectrum is multiplied with the derivation of the screen position to energy calibration function. The resulting spectrum is shown in figure 3.10d. In a last step, two artificial peaks resulting from reflection of the scintillation light at small metallic parts, directly attached next to the screen to reference the position of the spectrometer, are removed. The final reconstructed spectrum is shown in figure 3.10e.
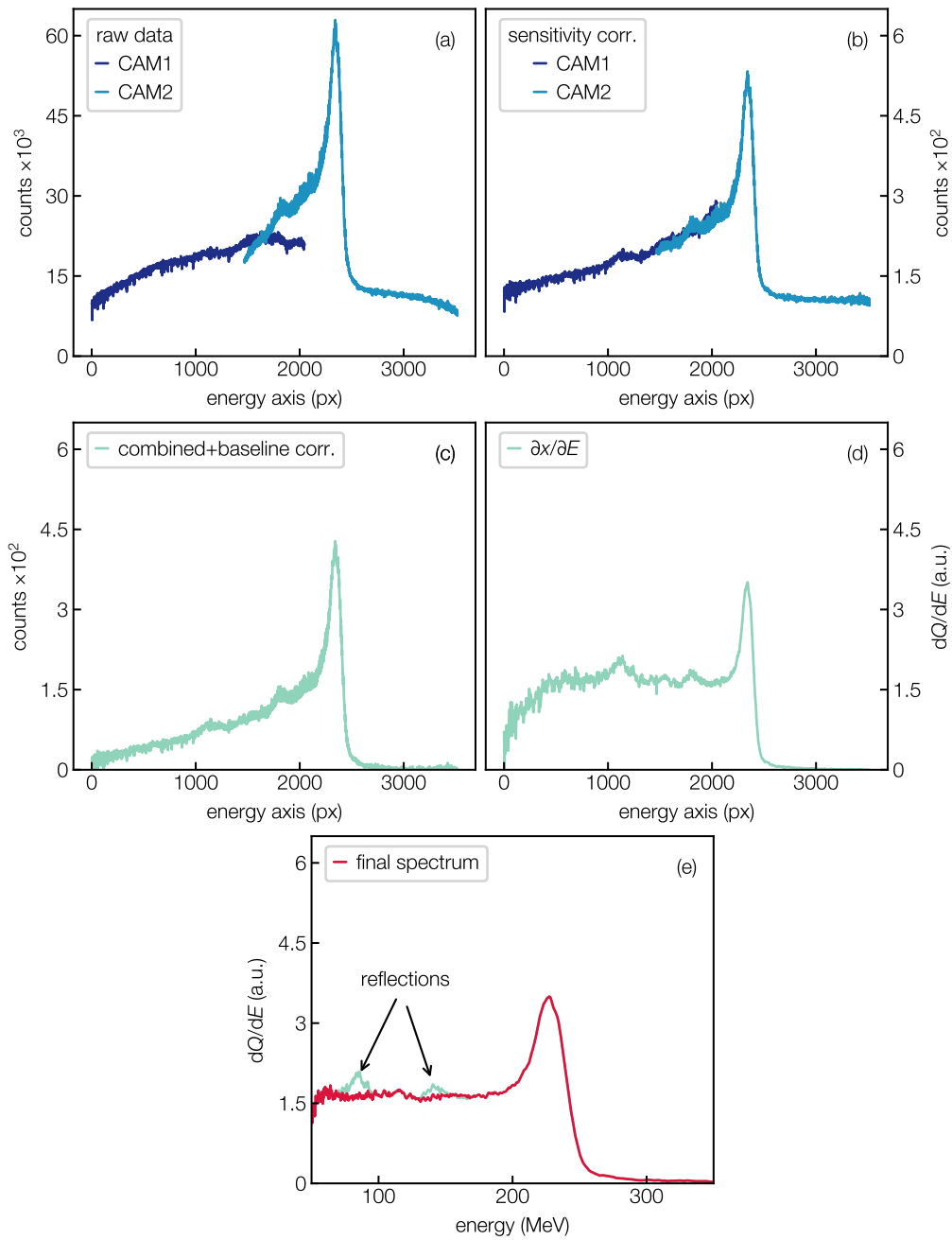
Figure 3.10 – Processing of spectrometer screen images. Projected signal of the raw images of CAM1 (dark blue) and CAM2 (light blue) (a). Sensitivity correction (b). Baseline subtracted and combined spectrum (c). Rescaling from counts per pixel to counts per energy interval (d). Final energy calibrated spectrum (red) after subtraction of two artificial peaks originating from reflections (teal) (e).

3.4.4 Emittance Reconstruction

The beam emittance describing the phase-space volume occupied by the electrons, is an important quantity when discussing electron beam quality. A low beam emittance is required to focus electron beams to a small spot size. Emittance measurements at LUX are based on a single-shot reconstruction technique where the beam is focused with the quadrupole doublet onto the spectrometer screen. The technique was developed by Weingartner et al. [8] and implemented by P. Winkler [79]. In the following, only the fundamental principles of the technique are discussed. For a more sophisticated description it is referred to [79].

The focusing of the quadrupole doublet is chromatic. Only the focused energy is imaged directly onto the spectrometer screen while lower energies are focused in front and higher energies behind the screen. The focused energy therefore seems to have a minimal spot size in the non-dispersive plane on the spectrometer screen while unfocused energies appear to be larger. The characteristic spectrometer screen image with electron signal is shown in figure 3.11a.
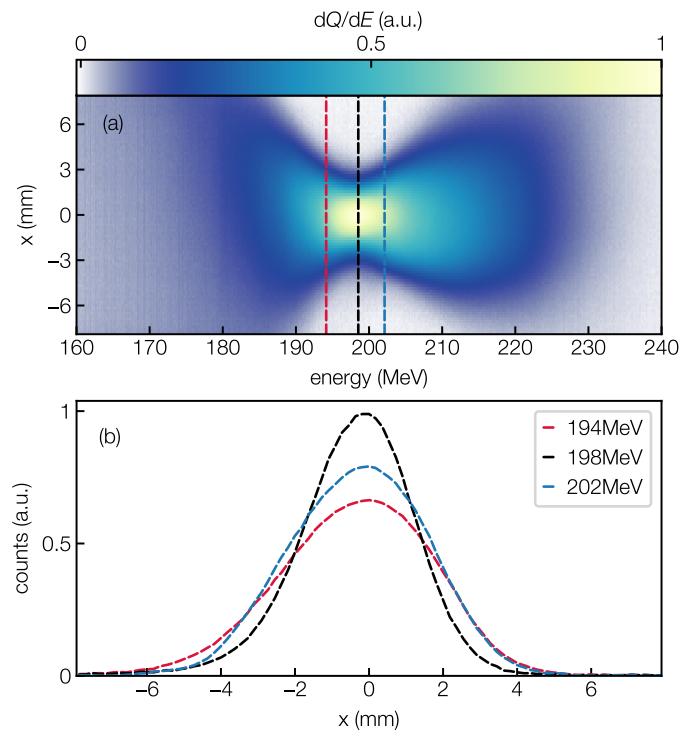
Figure 3.11 – Image of a beam profile measured on the spectrometer screen (a). The focusing was set to image a beam energy of 194 MeV. Colored lines indicate the range of ± 2 % around the focused energy from which the on-screen rms beam sizes are determined. The projected signal of these three lineouts are shown in (b).

In this case, the focusing was set for a beam energy of 198 MeV. The rms width of single energy slices in an interval $\pm 2\,\%$ around the focused energy are taken to determine the energy dependent on screen beam size. Three energy slices are exemplary indicated with the colored lines in figure 3.11a and the corresponding projections in figure 3.11b. Without further derivation, an equation can be found connecting the measured on-screen rms beam size $x_{\mathrm{rms}} = \langle x^2 \rangle_s^{1/2}$ to the rms beam size $x_{\mathrm{rms}} = \langle x^2 \rangle_o^{1/2}$, the rms beam divergence $x'_{\mathrm{rms},o} = \langle x'^2 \rangle_o^{1/2}$, and the correlation between electron position and angle $\langle xx' \rangle_o$ at the source, i.e. behind the plasma target. Fitting these equation to the measured beam sizes as a function of energy directly yields the transverse beam emittance

$$\varepsilon_{\mathrm{x}} = \sqrt{\langle x^2 \rangle_o \langle x'^2 \rangle_o - \langle xx' \rangle_o^2}. \tag{3.3}$$

When focusing, beam size and beam divergence change constantly during propagation from the plasma target to the electron spectrometer while the phase space volume and hence the beam emittance are conserved. This assumption only holds if no acceleration fields are present and for a small energy variation within the beam. It is thus common to normalize the beam emittance to the beam energy, i.e. $\varepsilon_{\mathrm{n,x}} = \gamma \epsilon_x$. The normalized beam emittance is also a conserved quantity under acceleration.

The single-shot reconstruction technique allows for energy resolved measurements of the transverse beam emittance and beam divergence in the horizontal plane, which corresponds to the laser polarization axis at LUX. The technique was used to investigate the beam emittance and beam divergence in dependence of the laser pulse energy within this thesis. The experimental results are presented in section 7.5.

3.5 Electron Screen Station

Two electron screen stations (ESS1, ESS2) are installed in the LUX beamline to measure the transverse beam profile and beam pointing 3.12 m and 7.65 m behind the plasma target. In the following, only the calibration of ESS1 is given as ESS2 was not used during the experimental campaign.

Design and Specification
The electron screen station was developed by the MDI devision at DESY and initially designed for the EUROPEAN XFEL [82]. It consists of a Cerium doped Lutetium based scintillation crystal (LYSO) which can be inserted into the electron beam bath with a motorized linear stage. The LYSO screen emits light in the visible regime at the position an electron beam passes through it. The intensity of the signal scales linearly with the charge density of the beam. The screen is imaged from the backside under an angle of

45 degree through a view port installed at the vacuum chamber The scintillation light is collected over a likewise tilted mirror with a Makro-Symmar $f = 120$ mm objective and a Basler avA2300-25gm CCD camera [83, 84]. The optical configuration follows the Scheimpflug principle, which ensures that the whole screen plane is imaged sharply. The imaging setup has a magnification factor of two. The individual components of the setup and their specifications are summarized in table 3.3.

Table 3.3 – Specification and Resolution of the electron screen station ESS1. Data taken from [83, 84].

type	specification	characteristic
scintillation screen	LYSO	size: $(35.5 \times 20 \times 0.2)$ mm
CCD camera	Basler avA2300-25gm	chip size: (2330×1750) px
objective	Schneider Makro/Symmar	$f = 120$ mm

Resolution	
spatial	(57.6×46.2) µm
charge detection limit	~ 30 pC

Resolution and Charge Detection Limit

The LYSO screen has a size of (35.5×20) mm and is 200 µm thick. The acceptance angle of freely drifting electrons from the source to the screen station is $x' = \pm 2.85$ mrad in the horizontal and $y' = \pm 4.4$ mrad in the vertical plane, considering the distance to the plasma target of 3.12 m. The CCD camera has a chip size of (2330×1750) px yielding a spatial resolution of (57×46.2) µm/px. The high spatial resolution of the optical setup with respect to the small electron beam size comes with the expense of charge sensitivity. The counts per camera pixel are comparably low and signal is lost in the noise. Only the core of the transversal intensity profile of the electron beam with a charge density above the noise level is therefore detectable with the screen station. Figure 3.12 shows the summed pixel counts of the camera image as a function of total bunch charge measured with BPM1, see section 3.6. The linear function fitted to the data shows a zero crossing of the image sum at ~ 30 pC, indicating the lowest detectable bunch charge. For an ideal, non sensitivity limited diagnostic, the linear fit should show a zero crossing of the image sum at zero bunch charge. Electron beams were tuned with the laser-plasma settings in this dataset. Beam divergence, beam energy, bunch charge and thus the charge density of the electron beams are expected to vary strongly. The charge detection limit can
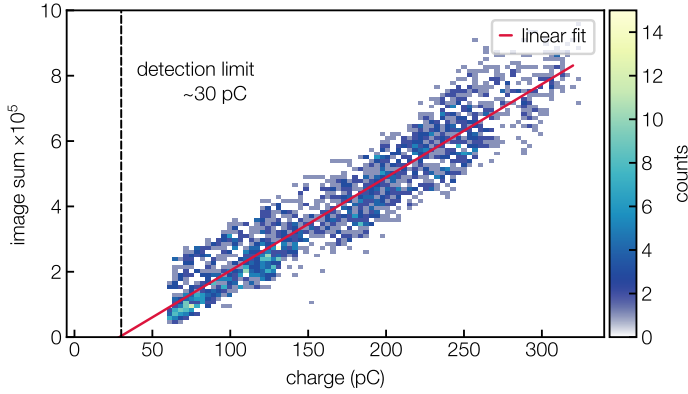
Figure 3.12 – Charge Detection limit of the electron screen station ESS1. Image as a function of total bunch charge Q_{tot} (measured with BPM1). A linear fit reveals the charge detection limit of $\sim 30\,\text{pC}$. Electron beams were generated with various laser pulse energies between $1.76\,\text{J}$ and $2.84\,\text{J}$ and nitrogen concentrations from $0.3\,\%$ to $5\,\%$, at a constant plasma density of $n_e = 2.55 \times 10^{18}\,\text{cm}^{-3}$.

therefore be understood as a mean detection limit. The single shot charge detection limit for electron beams with a small beam divergence and high bunch charge can be less and vise versa. It is further noted that no electron beams with a bunch charge less than $60\,\text{pC}$ were detected in this particular dataset, explaining that no data points below this value are seen in figure 3.12.

Due to the charge detection limit of the screen station, beam divergence measurements were cross checked with the single-shot reconstruction technique introduced in section 3.4.4. Electron beams were generated with the same laser-plasma settings in a short time frame ensuring similar beam properties for the comparison. The beam divergence reconstructed from the electron spectrometer screen was by a factor of 2.3 larger than the directly measured beam divergence from the screen station. The beam divergence from the reconstruction technique is given for a narrow energy range around the high-energy peak of the spectrum, whereas the beam divergence from screen station measurements is given energy integrated. Typical energy spectra of electron beams generated within this thesis and used for the comparison are shown in figure 6.2. PIC simulations presented in section 5.4 show that the beam divergence varies across the energy spectrum and is smaller for higher energies. Thus, the beam divergence measured on the screen station mainly corresponds to the low divergent, high energy part of the spectrum which exceeds the charge density detection limit of the diagnostic. However, from the comparison it is obtained that the screen station still underestimates the beam divergence of the core by a factor of 2.3. To account for this, beam divergence measurements on the screen station presented within this thesis are multiplied by this correction factor. It is noted that the single-shot reconstruction technique only allows to measure the horizontal beam divergence. However, as the charge detection limit does not depend on the screen orientation,

it is expected that the vertical beam divergence is underestimated by the same factor. A new screen station with improved sensitivity is currently being designed for LUX but was not available during the experimental campaign conducted within this thesis.

Image Processing

Step-by step-processing of a screen station image is illustrated in figure 3.13. Figure 3.13a shows the raw image of a transverse electron beam profile. A background image without electron signal but laser light is subtracted to remove ambient light. The resulting image is shown in figure 3.13b.
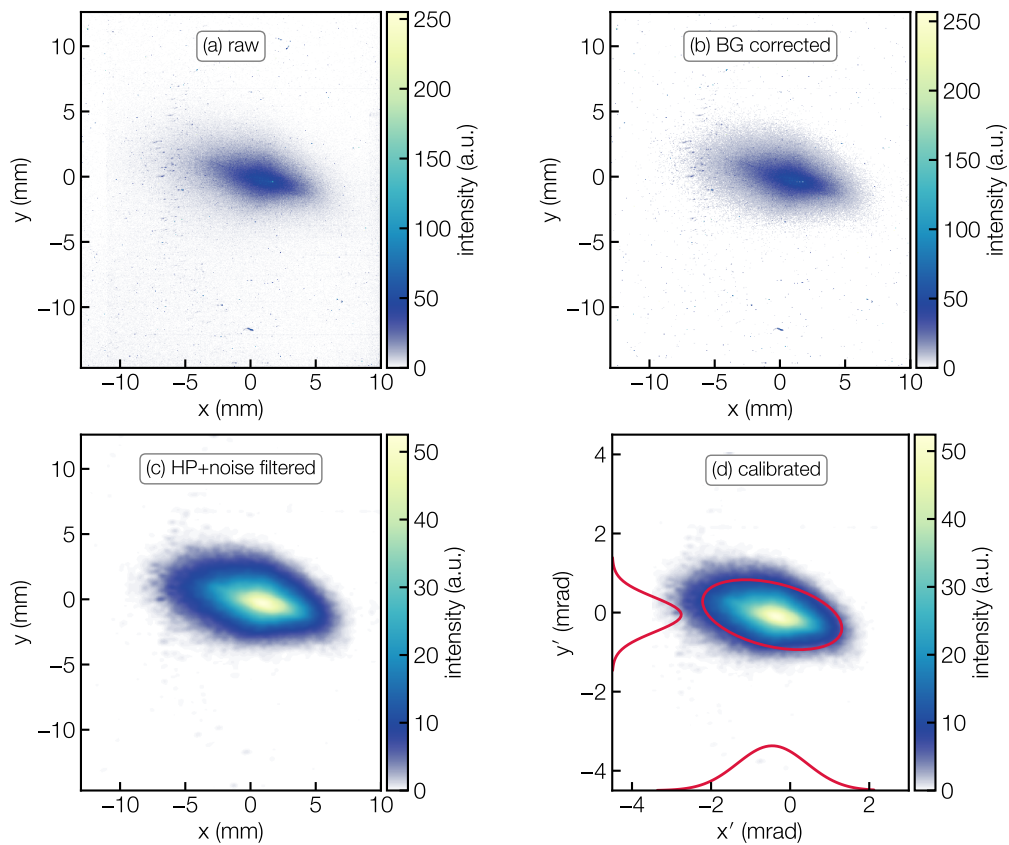
Figure 3.13 – Processing of an image recorded with ESS1. Raw image (a), background subtracted and base level removed (b). A median filter is used to remove hot-pixels and the intensity of one standard deviation is subtracted to remove electronic noise (c). Final calibrated image (d). Horizontal x'_{rms} and vertical y'_{rms} beam divergence are determined from the rms width of the projected signals (red lines) of a 2D Gaussian fit (red ellipse).

Next, a median filter averaging the signal over three adjacent pixels is applied to remove hot-pixels. A base level is taken from a part of the raw image without electron signal and subtracted to remove noise. The corresponding image is shown in figure 3.13c. The final

image after cropping to a region of interest and calibration from millimeter to milliradiant is shown in figure 3.13d.

A 2D Gaussian function is then fitted to the image to determine the rms beam divergence from the projected signal of the fit. As mentioned before, the rms beam divergences in both planes are multiplied by a factor of 2.3 to account for the low charge sensitivity of the screen station.

3.6 Cavity Type Beam Position Monitor

The electron bunch charge is typically obtained from scintillation light of the electron spectrometer in the framework of laser-plasma accelerators. Although the commonly used screen types have been characterized and their response functions are well documented, these calibrations do not take the individual optical components and their sensitivity into account [85]. As one of the first laser-plasma accelerators, to our knowledge, LUX is equipped with two cavity type beam position monitors (BPMs) for non-invasive charge and position measurement. These BPMs have been developed and build for the European XFEL [86]. A BPM is a resonator cavity which picks up the electric field of an electron beam passing through. The electron beam excites a monopole and a dipole mode in the cavity. The electric field of the monopole scales with the beam charge, whereas the electric field of the dipole mode gives the transverse position of the electron beam inside the cavity.

The bunch charge measurement return the total sum of electrons in the beam. It is energy independent and also not affect by beam divergence, as long as the beam is not clipped by an aperture. The transverse position of the electron beam given for the center of mass of the electron distribution passing through the cavity. The position measurement is thus affected by electron phase-space distribution and also beam divergence. For the operation of the LUX beamline, however, only the position of the low divergent core of the beam is relevant, as only this part is typically filtered out and transported with the electron beam optics. Thus, to more precisely determine the position of the core of the electron beam in the beamline, the position measurement of the BPMs were calibrated with position measurements on the electron screen stations. As mentioned before, the screen stations only detect the core part of the electron beam due to their charge detection limit, see section 3.5.

Figure 3.14 shows the correlation between beam position measurements using BPM1 and ESS1. The data is taken from the experimental campaign presented in chapter 7 and includes electron beams generated at different laser-plasma settings. Thus, electron beam properties cover a wide parameter space, ensuring accurate calibration.

The correlation between the position measurements is not 1. In fact, the slope of the linear fit in the horizontal plane is -1.60 and 1.89 in the vertical plane. As mentioned before, the BPM returns the center of mass of the electron distribution, whereas the electron screen station returns the position of the core of the electron beam. This difference causes the discrepancy between the two diagnostics. The slopes of the linear fits yield the calibration factors which are applied to the raw position readings of the BPMs. A similar measurement was performed for BPM2 and ESS2 but is not shown here. The calibration functions for both BPMs are listed in table 3.4.
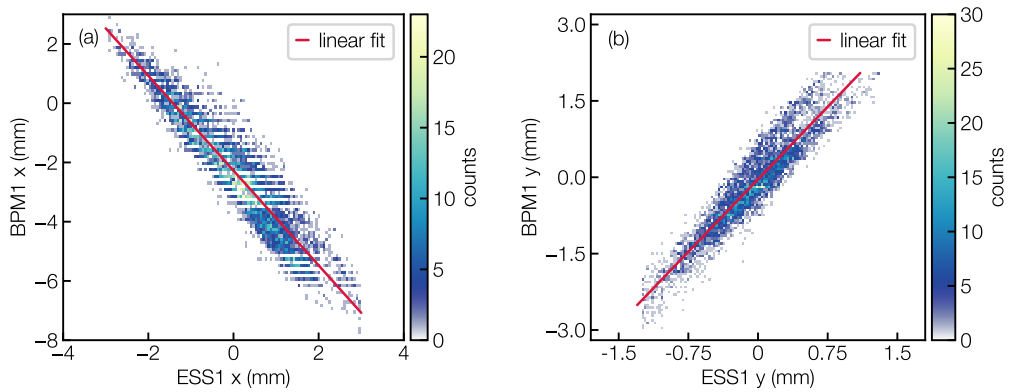
Figure 3.14 – Electron beam position measured with BPM1 in the horizontal (a) and vertical plane (b) as a function of the beam position measured with ESS1. A linear fit is used to get the calibration factor for the BPM position measurement, see table 3.4.

Table 3.4 – Calibration functions for the beam position measurement of BPM1 and BPM2.

	BPM1 (mm)	BPM2 (mm)
Horizontal plane	$x = \text{-}1.60\,x_{\mathrm{raw}} \pm 0.2$	$x = 1.31\,x_{\mathrm{raw}} \pm 0.3$
Vertical plane	$y = 1.89\,y_{\mathrm{raw}} \pm 0.2$	$y = 1.37\,y_{\mathrm{raw}} \pm 0.3$

4 Plasma Target and Diagnostics

Electron beams are generated in so called plasma targets providing the neutral gas density distribution from which the plasma is formed. Beside laser pulse properties, electron injection and acceleration are determined by the gas respectively plasma properties within these plasma targets, especially by the longitudinal profile. Two common types of plasma targets are super sonic gas jets [87–90] and capillary or gas cell type plasma targets [91–93]. Compared to super sonic gas jets, capillary type plasma targets can be operated with continuous gas flow at low backing pressures. This results in a static longitudinal gas pressure and hence plasma density profile which reduces density fluctuations and shot-to-shot variations in electron beam parameters [18]. In addition, the longitudinal plasma density profile is tailored depending on the inlet and capillary design of the plasma target. This enables, for example, to create plasma density ramps at the exit of the plasma target to match the electron beam size into vacuum and to reduce the beam divergence [94, 95]. These are the underlying reasons why capillary type plasma targets are used in the LUX beamline for the electron beam generation.

This chapter covers the capillary type plasma target specifically designed to study and optimize laser-plasma acceleration with ionization injection. Its design, based on Computational Fluid Dynamics (CFD) simulations is presented in section 4.1. The characteristic longitudinal gas pressure profile used as input for accompanying PIC simulations is introduced in section 4.2. Electron beams were generated within this thesis in a nitrogen doped hydrogen plasma. Special care was therefore taken if the nitrogen gas affects the fluid dynamics and the longitudinal gas pressure profile. A diagnostics to online monitor the gas pressure directly at the capillary is introduced in section 4.3. The two channel gas mixing device allowing to precisely control the gas flow into the plasma target as well as the ratio of the hydrogen-nitrogen gas mixture is presented in section 4.4. The electron density of the plasma n_e is referred to as plasma density and the gas pressure to pressure in the following discussion.

4.1 Plasma Target Design

Figure 4.1 shows an image of the plasma target. It consists out of two sapphire plates each with a size of $(10 \times 10 \times 3)$ mm.
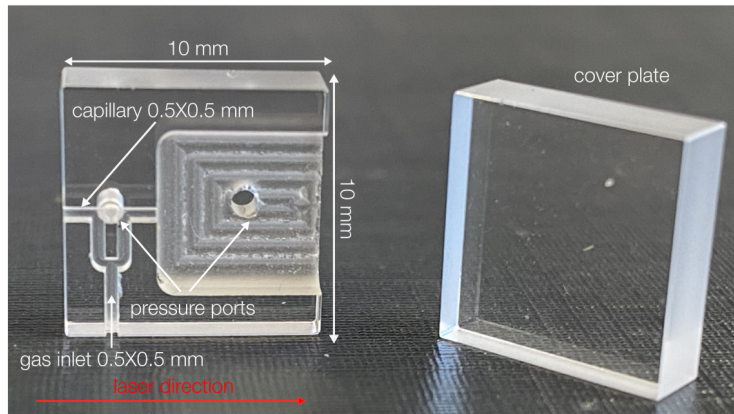
Figure 4.1 – Capillary type plasma target made out of two sapphire plates. Each plate has a size of $(10 \times 10 \times 3)$ mm. The laser-plasma interaction channel (capillary) and the gas inlet have a cross section of (500×500) μm. The capillary has a longitudinal length of 4 mm and the cut-out volume of 6 mm. The pressure ports have a diameter of 500 μm. Plates are mounted face to face to close the structure.

Sapphire was chosen as material for longevity, due to its hardness, high melting point, high thermal conductivity and resistance towards electric fields [96]. The capillary where the laser-plasma interaction takes place and the gas inlet both have rectangular cross sections of (500×500) μm and are machined into a single plate with a commercial supersonic milling machine. A second un-machined sapphire plate is used to seal the structure when both plates are mounted face-to-face into a specially designed holder. Gas is fed into the plasma target with a single inlet coming from the bottom which is then splitted into two before connecting with the 4 mm long horizontal interaction channel. A rectangular volume was cut out at the exit to create smooth plasma-vacuum transition. This reduces the beam divergence, see section 5.3. Two holes, each with a diameter of 500 μm are drilled from the back side of the sapphire plate onto the capillary at its center and in the cut-out volume, respectively. These drillings, from now on called pressure ports, are connected over the target holder to two out of vacuum pressure gauges, allowing to online monitor the pressure, see section 4.3.

4.2 CFD Simulations

This section covers the CFD simulation of the gas dynamics in the plasma target utilizing the open source software package OpenFOAM [97]. As the plasma target is operated in experiments with different hydrogen-nitrogen gas mixtures, the influence of the fluid properties on the longitudinal pressure and velocity profile are investigated in section 4.2.2.

4.2.1 Simulation Environment

The motion of a fluid and the interaction with a surfaces are governed by the Navier-Stokes equations [98]. The coupled set of differential equations describes the relation between pressure, velocity, density and temperature of the fluid. In CFD simulations, these equations are discretized onto a mesh, representing the simulation domain, in our case the plasma target. Different discretization schemes and solvers are included in the OpenFOAM package where the usage depends on the fluid properties and the flow regime. The *sonicFoam* solver was used to simulate the plasma target [99]. The solver is applicable for compressible gases in the laminar and turbulent flow regime with transsonic to supersonic velocities. The PISO algorithm (Pressure-implicit with Splitting Operators) is used to solve the Navier-Stokes equation with pressure and velocity as dependent variables. Turbulences are implemented with the k-omega model. A more detailed description of the *sonicFoam* solver is found in [99].

Mesh Generation
The 3D mesh, created from a CAD model using the *snappyHexMesh* toolbox is illustrated in figure 4.2. The mesh consists of approximately 200000 hexahedral finite volume cells on which the simulation is discretized. It contains the geometry of the plasma target in the center and two additional boxes (outlets) at the left and right sides, modeling the ambient vacuum. The cell size was varied across the mesh to reduce computational time. A cell size of $(62.5 \times 62.5)\,\mu m$ was set for regions with large pressure and velocity gradients such as the body of the plasma target and the transition into the vacuum. The cell size was increased to $(500 \times 500)\,\mu m$ for the outlets. The gas is fed into the plasma target from the bottom through the inlet patch (red).
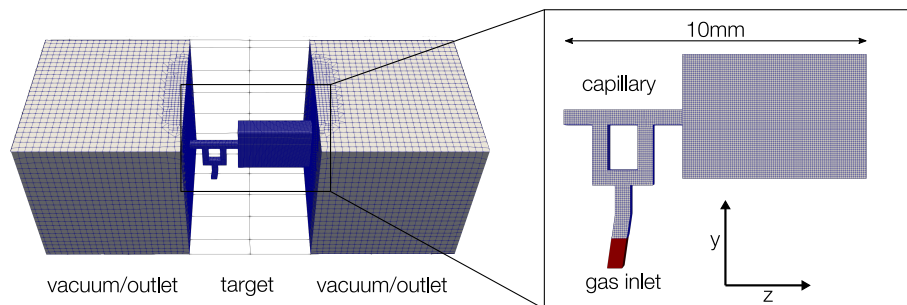
Figure 4.2 – Simulation mesh containing the plasma target (center) and two additional boxes (left and right sides) to model the ambient vacuum (outlets). The size of the hexahedral cells for the capillary and the gas inlets is $(62.5 \times 62.5)\,\mu m$ and $(500 \times 500)\,\mu m$ for the outlets. The gas is fed into the capillary from the bottom (red patch).

Boundary Conditions

Suitable boundary conditions, describing the interaction of the fluid with the walls of the mesh have to be applied to the different regions of the mesh to create a well-posed simulation environment. The *zeroGradient* boundary condition for pressure (pressure gradient normal to the wall is zero) and the *fixedValue* boundary condition for velocity ($v = 0\,\mathrm{m/s}$ at the walls) were assigned to the regions of the mesh representing the plasma target. For the vacuum outlets, the boundary conditions *WaveTransmissive* for pressure and *inletOutlet* for velocity were assigned. A zero gradient condition is applied for flux pointing out of the plasma target and the velocity set to $v = 0\,\mathrm{m/s}$ for flux pointing inwards. Thus, back-flow into the plasma target is suppressed. Pressure and velocity at the gas inlet are specified with the boundary condition *pressureInletOutletVelocity*. A generic inlet flow at a total pressure is applied and back-flow suppressed by setting $v = 0\,\mathrm{m/s}$ in case of inwards pointing flux. The temperature across the whole simulation domain was set to $298\,\mathrm{K}$. A more detailed documentation of the boundary conditions can be found in [100].

Simulation

Simulations were run in parallel on the DESY Maxwell HPC Cluster. The mesh was decomposed into eight subparts and each part computed on an individual CPU. After the simulation was finished, the parts are reconstructed into a single domain. The time dependent simulation was performed with an automatic time step adjustment to ensure convergence and high accuracy of the results. A stability criterium of the numerical algorithm is given by the Courant–Friedrichs–Lewy number (CFL), i.e. in 3D by

$$C = \Delta t \left(\sum_{i=1}^{3} \frac{u_{x_i}}{\Delta x_i} \right), \tag{4.1}$$

where Δt is the time step, u_{x_i} the magnitude of the fluid velocity, and Δx_i the length interval in each direction [101]. A calculation can be assumed to be stable for $C < 1$ which states that the fluid only propagates through one cell in one time step. To fulfill the condition on the complete mesh, the time step has to be chosen with respect to the smallest cell size and highest expected velocities. As the velocity and the cell size vary across the mesh, the computation time is rather long, i.e. a day for the presented plasma target. As a solution, a maximum CFL number of $C < 0.7$ was specified and the time step is automatically adjusted for each cell size and velocity locally to stay below the maximum. This reduces the simulation time to $\sim$ 4-6 hours, depending on the inlet and outlet pressure.

4.2.2 Fluid Properties

A thermo physical model is used to calculate the fluid properties based on temperature and velocity. The fluid is modeled as an ideal, compressible gas. The equation of state is given by

$$\rho = \frac{1}{RT}p, \tag{4.2}$$

with ρ being the density, R the gas constant, T the temperature and p the pressure [98]. The thermodynamic properties are assumed to be constant during transport, i.e. the fluid viscosity η, the specific heat capacity at constant volume c_v and at constant pressure c_p, and the Prandtl number $P_r = c_p\eta/\kappa$, with κ being the thermal conductivity do not change with temperature [102]. The Prandtl number connects the velocity and the temperature of the fluid. Electron beams were generated with ionization injection within this thesis. The plasma is therefore formed from a hydrogen-nitrogen gas mixture. The OpenFOAM simulations, however, did not allow to directly specify two gas species and to evaluate their mixing due to the constant transport model. The input gas species is defined in the thermo physical model by means of viscosity η, specific heat capacity $c_{v,p}$, Prandtl number P_r and the Molecular weight M. These parameters, can be defined for a binary gas mixture depending on their ratio with the following set of equations. The calculated parameters are then used to specify the input gas species in the simulation. The relevant parameters for hydrogen and nitrogen are listed in table 4.1.

Table 4.1 – Gas properties of hydrogen and nitrogen at 1 atm pressure level and 298 K. Taken from [103, 104]

Species	M	c_v (J/kg/K)	c_p (J/kg/K)	η (Pas)	κ (W/mK)	P_r
H_2	2.016	10221	1431	8.963×10^{-6}	0.185	0.69
N_2	28.013	743	1040	17.84×10^{-6}	0.0258	0.718

The molecular weight and the specific heat capacity of a binary mixture of gases are the sum of the fraction of each species, i.e.

$$
\begin{aligned}
M_{\text{tot}} &= (1 - x_1)M_1 + x_1 M_2 \\
c_{v_{\text{tot}}} &= (1 - x_1)c_{v_1} + x_1 c_{v_2},
\end{aligned}
\tag{4.3}
$$

with x_1 being the mole fraction of one of the gas species [105]. The viscosity of a gas mixture can be calculated with a method from *Herning-Zipperer*, which is based on a first-order kinetic approach and reads for a binary gas mixture

$$\eta_{\mathrm{mix}} = \frac{x_1\eta_1}{x_1 + x_2\phi_{12}} + \frac{x_2\eta_2}{x_2 + x_1\phi_{21}}$$

$$\text{with}$$

$$\phi_{12} = \left(\frac{M_2}{M_1}\right)^{1/2} = \phi_{21}^{-1}, \tag{4.4}$$

with $x_{1,2}$ being the mole fractions and $\eta_{1,2}$ the viscosities of each gas species [105]. The thermal conductivity κ, relevant for the calculation of the Prandtl number, is given by the *Wassiljewa* equation, i.e.

$$\kappa_{mix} = \sum_{i=1}^{n} \frac{x_i\kappa_i}{\sum_{j=1}^{n} x_j\phi_{ij}},$$

$$\text{with}$$

$$\phi_{ij} = \frac{\left(1 + \left(\frac{\mu_i}{\mu_j}\right)^{0.5}\left(\frac{M_j}{M_i}\right)^{0.25}\right)^2}{\sqrt{8}(1 + (M_i/M_j))^{0.5}}, \tag{4.5}$$

where x_i is the mole fraction of the each gas species [106]. The main effect of adding nitrogen to the hydrogen gas is an increase of the fluid viscosity which gives a measure of the flow resistance to deformation, or its thickness. A larger viscosity implies that the flow rate Q and hence the velocity v of the fluid decrease. An estimation of the flow rate at the exit of a circular pipe can be given with the *Hagen-Poiseuille* (HP) equation for compressible fluids and reads

$$Q\left[\mathrm{m^3s^{-1}}\right] = \frac{\pi R^4}{16\eta L}\left(\frac{P_i^2 - P_o^2}{P_o}\right), \tag{4.6}$$

with R and L being the radius and length of the pipe and $P_{i,o}$ the inlet respectively outlet pressure [107]. Eq. 4.6 predicts that the flow rate decreases with the viscosity for a constant pipe geometry and pressure drop $P_i - P_o$. The HP model was used to verify the applicability of the above derived calculations for the properties of a gas mixture. A validation simulation case was set up where a single pipe with a radius of 0.5 mm and a length of 5 mm is connected to a box with vacuum conditions. A slice through the center of the simulation domain is shown in figure 4.3.
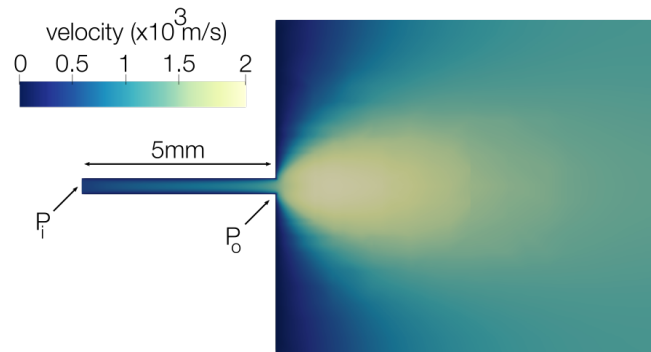
Figure 4.3 – Transverse slice through the validation case. A circular pipe with $r = 500\,\mu m$ and a length of $5\,mm$ is connected to vacuum. The colormap shows the magnitude of the velocity field. P_i and P_o denote the inlet and outlet pressure, respectively.

Various hydrogen-nitrogen gas mixtures were applied at the inlet patch. The simulations were run with the solver and boundary conditions stated previously. In steady state, the simulations showed an inlet pressure of $P_i = 88\,mbar$ and an outlet pressure of $P_o = 0.7\,mbar$. The pressure difference between inlet and outlet is independent of the gas mixture as the solver automatically adjusts the input flow rate to reach a steady state. Thus, P_i and P_o were used to calculate the flow rates with eq. 4.6 and kept constant while varying the viscosity. The flow rates in the simulations were obtained by integrating the fluid velocity over the cross sectional area of the pipe at the transition to the vacuum.

The comparison between simulated and calculated flow rate as a function of the nitrogen concentration C_{N_2} and hence the viscosity are shown in figure 4.4. Here, $C_{N_2} = 0\,\%$ corresponds to pure hydrogen and $C_{N_2} = 100\,\%$ to pure nitrogen.

Both, simulations and the *Hagen-Poiseuille* model show the same asymptotic decrease of the flow rate for increasing nitrogen concentration. The absolute decrease, especially for higher nitrogen concentration, is larger in the simulations. The difference can be explained by the influence of other fluid properties such as the Prandtl number, or the thermal conductivity which are not covered with the HP model. In addition, the HP model only considers the fluid motion in 1D, whereas the CFD simulation is in 3D. The predicted decrease in the relevant operation range for the conducted experiments of $C_{N_2} = 0.1\,\%$ to $C_{N_2} = 5\,\%$, on the other hand, is in very good agreement. It shows that the fluid velocity is mainly affected by the viscosity for comparable low nitrogen concentrations and thus proving the applicability of the above derived formalism to model the mixing of two gas species in OpenFOAM.
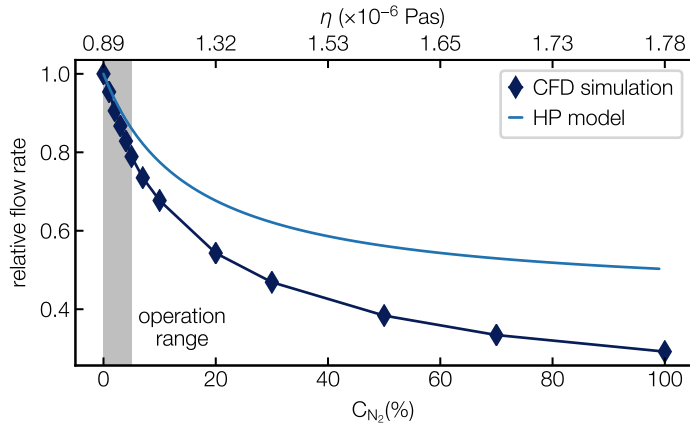
Figure 4.4 – Simulated (dark blue) and calculated (light blue) flow rates, according to eq. (4.6) with $P_i = 88\,\text{mbar}$ and $P_o = 0.7\,\text{mbar}$, as a function of the nitrogen concentration C_{N_2}. The gray shaded area indicates the relevant operation range for this thesis between $C_{N_2} = 0.1\,\%$ and $C_{N_2} = 5\,\%$.

4.2.3 Simulation Results

Having established the simulation environment, the fluid dynamics in the plasma target are derived in this section. The plasma target is operated in the experiments with continuous gas flow and the pressure is measured at the center of the capillary with a absolute calibrated pressure gauge, see section 4.3. In the simulations, the inlet pressure was chosen to reproduce typical experimental conditions, i.e. pressures between $30\,\text{mbar}$ and $70\,\text{mbar}$. As the pressure drops from the inlet patch to the center of the capillary where the reference pressure is taken, higher pressures than measured have thus to be set in the simulation. The vacuum pressure in all simulations was set to $10^{-3}\,\text{mbar}$.

The characteristic longitudinal pressure and velocity profile in laser propagation direction z for an inlet pressure of $100\,\text{mbar}$ and pure hydrogen are shown in figure 4.5.

The profiles are taken from a lineout through the center of the capillary which is extended by $1\,\text{mm}$ to the left and right sides to include the transition into vacuum. The geometry of the plasma target is illustrated in the background with the colormap showing the 2D pressure distribution. The pressure decreases from the inlet into vacuum resulting in a symmetric profile between $z = 0\,\text{mm}$ and $z = 6\,\text{mm}$ with an up-ramp at the entrance followed by a $1.2\,\text{mm}$ long plateau with a constant pressure of $48\,\text{mbar}$ and a down-ramp with a similar gradient as the up-ramp.

Noticeable is the pressure ramp starting at $z > 6\,\text{mm}$ which is caused by the former mentioned cut-out volume where the conductance is higher than if the capillary would open directly into vacuum. This characteristic feature of the plasma target enhances the evolution of the transverse electron beam parameters out of the target. The slowly
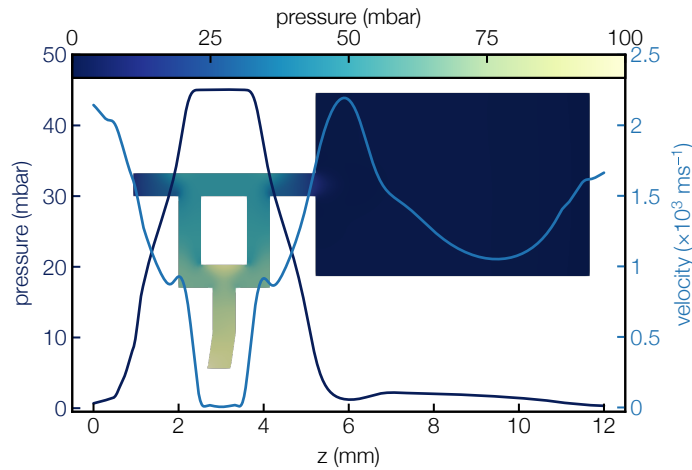
Figure 4.5 – Longitudinal pressure (dark blue) and velocity profile (light blue) in the plasma target simulated with an inlet pressure of 100 mbar and pure hydrogen. The plasma target geometry including the cut-out volume is illustrated in the background. The colormap shows the 2D pressure field.

decreasing pressure acts as an adiabatic extraction section, gradually decreasing the focusing fields of the wakefield. This counteracts the rapid expansion of the beam size compared to a sharp plasma-vacuum transition. The effect will be discussed with PIC simulations in section 5.3.

The velocity strongly varies along the capillary. The velocity is highest with ~ 2200 m/s at the exit of the plasma target where the gas enters vacuum. In the center where the pressure plateau is formed, on the other hand, the velocity is minimal with ~ 0 m/s. The zero net velocity in this region allows to directly measure the static pressure in the capillary to deduce the plasma density, see section 4.3.

The pressure and velocity profile for the relevant hydrogen-nitrogen gas mixtures with nitrogen concentrations of 1 %, 3 % and 5 % as well as for pure hydrogen and pure nitrogen are shown in figure 4.6. An inlet pressure of 100 mbar was applied in all simulations. The pressure profile is nearly independent of the nitrogen concentration, only the plateau pressure slightly increases with the nitrogen concentration. The velocity, on the other hand, is greatly reduced at higher nitrogen concentrations. The reason being is the decrease of the fluid velocity for increasing viscosity and hence nitrogen concentration, as was discussed with the simulation validation case and the *Hagen-Poiseuille* model, see figure 4.4.

The decrease of the fluid velocity for increasing nitrogen concentrations affects the operation of the plasma target in daily operation. As was mentioned before, the inlet flow rate of the gas mixture is regulated to set a specific plateau pressure. If the concentration is increased at constant flow rate, the pressure in the capillary rises as the fluid velocity
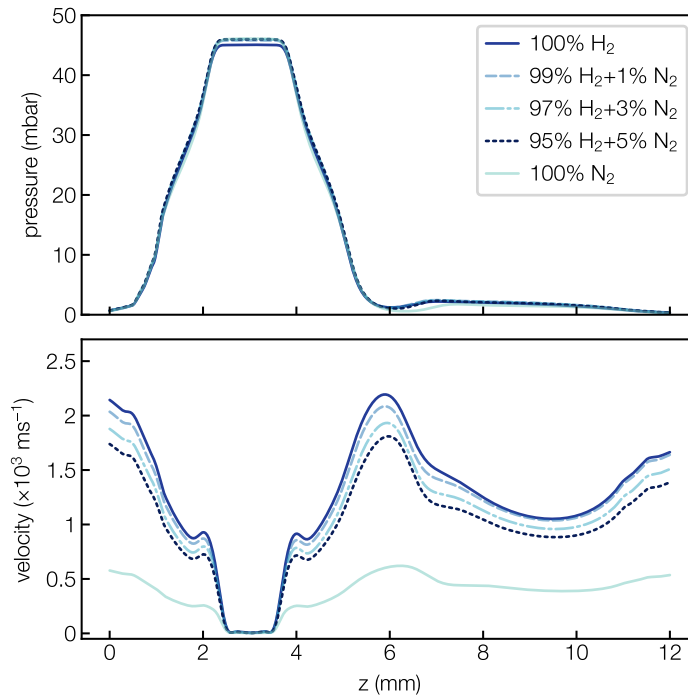
Figure 4.6 – Longitudinal pressure (top) and velocity profile (bottom) for various hydrogen-nitrogen gas mixtures and an inlet pressure of 100 mbar.

decreases and vise versa. The flow rate has therefore to be adjusted with the nitrogen concentration to keep the pressure in the capillary constant.

4.3 Online Pressure Diagnostic

The pressure exerted in the capillary by the moving fluid is given by the sum of the velocity pressure p_v and static pressure p_s [98]. Velocity pressure is measured by placing a so called *Pitot Tube* directly into the flow. Static pressure is measured perpendicular to the flow direction where the fluid is at rest [108]. In contrast to velocity pressure, static pressure can be measured without interacting with the on-axis fluid. Due to the operation of the target with continuous gas flow, such a region with zero net velocity is formed between the gas inlets, as was shown with simulations in section 4.2.3. The pressure can hence be directly measured through a drilling, the pressure ports, in the back of the capillary. The measurement technique is illustrated in figure 4.7.

The two sapphire plates of the plasma target are placed into a precisely fitting extraction in the target holder and pressed together with an additional frame (not shown). For a better visibility, only the target back plate with the capillary and inlet structure is shown.
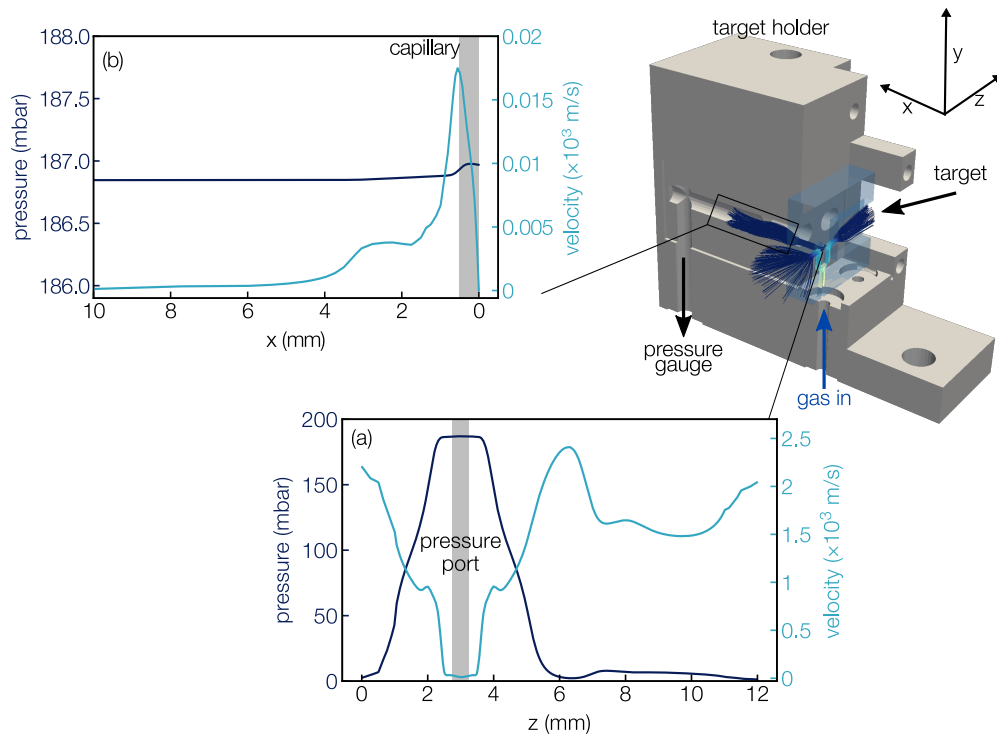
Figure 4.7 – Cut view of the target holder illustrating the direct pressure measurement technique. The gas flow is directed into the target from the bottom over the target holder. The pressure port is connected through the holder to an out-of-vacuum Pfeiffer CMR 361 capacitive pressure gauge. Longitudinal pressure and velocity profile in the capillary in laser propagation axis (a). Transverse pressure and velocity profile in the pressure port and the backside of the target holder (b). The gray shaded areas indicate the location of the pressure port. The Simulation was run with an inlet pressure of 500 mbar.

The gas is coming from the bottom of the holder. The flow direction is indicated with the stream lines. The pressure port is accessed from the back of the holder with a 90 degree drilling coming from the bottom. A sealing between the back of the target plate and the holder ensures a leak tight connection. The target holder assembly is mounted onto the in-vacuum positioning system which is connected to the out-of vacuum gas system. The system consists of a gas mixing device, see section 4.4 and an absolute calibrated Pfeiffer CMR 361 capacitive pressure gauge with sub percent-level resolution [109]. The components and their specifications are listed in table 4.2.

A CFD simulation was set up to verify the working principle of this technique, see figure 4.7. An extra volume which was exactly modeled after the cut out volume in the target holder was attached to the target representing the gas line to the pressure gauge. An inlet pressure of 500 mbar was set to reduce computational time and to ensure convergence, as the mesh is significantly increased with the extra volume. The comparison between

pressure and velocity in the capillary and in the pressure port are shown in figure 4.7a and 4.7b, respectively. The overlap between pressure port and the capillary is indicated with the gray shaded area. The longitudinal profiles in the capillary are the same as in the simulations performed without the extra volume. The pressure port does hence not affect the fluid dynamics in the capillary which ensures a non-invasive measurement. The pressure in the extra volume slightly decreases from the center of the capillary towards the back of the target holder by $\sim 0.2\,$mbar. The deviation between the pressure along the pressure port and at the center of the capillary, however, is on the sub percent-level, verifying the applicability of the technique. Thus, it is assumed that the pressure measured out of vacuum in the experiments corresponds to the plateau pressure in the capillary.

Pressure Calibration Measurement

The assembly of the gas supply and diagnostics system consists of several individual parts with connections for the gas flow between them. Proper sealing of these connections is crucial to ensure accurate measurements. The system was therefore cross checked with a second independent measurement. The target chamber was evacuated below $10^{-1}\,$mbar pressure level and subsequently filed with hydrogen in several discrete steps. The pressure readings at the capillary at an identical pressure gauge, directly installed at the target chamber, are then compared after a constant pressure was reached. The data of both pressure gauges for the different intermediate steps is shown in 4.8. A deviation of only $\sim 2\,\%$ was obtained from a linear fit, indicating that the system is in fact leak tight.
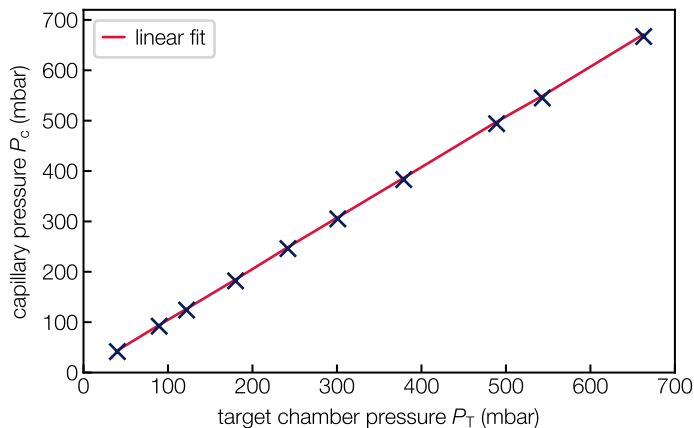
Figure 4.8 – Capillary pressure as a function of target chamber pressure, recorded with two identical Pfeiffer CMR 361 capacitive pressure gauges (crosses). Linear fit $P_{\mathrm{c}}(\mathrm{mbar}) = 1.02 P_{\mathrm{T}} + 2\,$mbar (red).

In the framework of laser-plasma acceleration, the gas distribution is typically described in terms of gas density, i.e. electrons per unit volume. The gas density can be calculated from the measured pressure with the ideal gas law $pV = N k_{\mathrm{b}} T$, where k_{B} is the

Boltzmann constant [108]. Simulations showed that the temperature at the plateau corresponds to the input temperature of the gas and does not change significantly. The real temperature at the capillary could not be determined experimentally. For the conversion of measured capillary pressures into gas density and subsequently into plasma density, room temperature, i.e. $T = 294\,\mathrm{K}$ is assumed.

Simulations and calibrations show that the peak plateau pressure can be measured with high accuracy. CFD simulation results of the longitudinal pressure profile could not be verified experimentally within the framework of this thesis as no diagnostics was available at the LUX beamline. However, a similar plasma target design was characterized in previous work with Raman-spectroscopy. The results were in good agreement with CFD simulations [110]. Thus, the simulated pressure profiles were used as input for PIC simulations, presented in chapter 5.

4.4 Gas Mixing Device

The gas flow into the plasma target and the composition of the gas mixture is controlled online with the two channel mixing device GMS_2CH [111]. A picture of the device is shown in figure 4.9.

Figure 4.9 – Two channel gas mixing device GMS_2CH with two Sensirion SFC5400 mass flow controllers (MFC1, MFC2) to adjust the gas flow and the mixing ratio of two gas species. MFC1 has a full scale of $1\,\mathrm{l_n/min}$ and is used for hydrogen (blue), whereas MFC2 has a full scale of $0.05\,\mathrm{l_n/min}$ and is used for nitrogen (yellow).

Two Sensirion SFC5400 mass flow controllers (MFC1, MFC2) [112], each factory calibrated for a range of specific gas species, are used to mix two input gas streams into a

single output gas stream at a user defined ratio and flow rate. The achievable mixing ratio depends on the specified output flow rate and is determined by the full range of the mass flow controllers. MFC1 is calibrated for hydrogen, the main gas species, and has a full range of $1\,l_n/min$. MFC2 is used for the dopant gas and calibrated for nitrogen, argon and neon with a full range of $0.05\,l_n/min$. The specifications are summarized in table 4.2.

Table 4.2 – Specifications of the gas supply and diagnostics system. Data taken from [109, 111, 112].

.

Device	Range	Accuracy
direct pressure measurement		
Pfeiffer CMR 361	$0.1\,mbar$ - $1000\,mbar$	$0.2\,\%$ of read out
gas mixing device GMS_2CH		
SFC5400 (MFC1 H_2)	$0\,l_n/min$ - $1\,l_n/min$	$0.8\,\%$ of setting
SFC5400 (MFC2 N_2)	$0\,l_n/min$ - $0.05\,l_n/min$	$0.8\,\%$ of setting

Stable gas flows and mixing ratios are required to ensure constant gas and hence plasma properties during electron beam generation. In the experimental campaign, data was collected at nitrogen concentrations between $0.1\,\%$ and $5\,\%$ and typical acquisition times of 10 minutes or 100 consecutive shots. The mixing stability over this timespan is exemplary shown for nitrogen concentrations of $0.1\,\%$, $1\,\%$ and $5\,\%$ in figure 4.10.

The output flow rate for all concentration was set to $0.5\,l_n/min$. The flow rate of each controller was recorded individually over 10 minutes and the concentration calculated from the ratio of the flow rates of each controller. The gas mixing device constantly measures and adjusts the flow rate of each channel at a rate of $1\,kHz$, which results in sub percent-level mixing stability for the explored range of nitrogen concentrations. The total output flow rate which gives the pressure in the capillary showed stabilities on the same order. This allows for stable gas properties in the plasma target.

With the direct pressure measurement technique and the gas mixing device, it is possible to determine the operation range of the plasma target in terms of achievable plasma density for nitrogen concentrations between $0.1\,\%$ and $5\,\%$. This was done in the following steps: First, the nitrogen concentration was set to $5\,\%$ and the output flow rate increased in several steps from $0.05\,l_n/min$ to $1.05\,l_n/min$ while recording the capillary pressure. The measured pressures were then transformed into neutral gas density with the ideal gas law. The electron density of a background plasma formed from a hydrogen-nitrogen gas mixture is given by
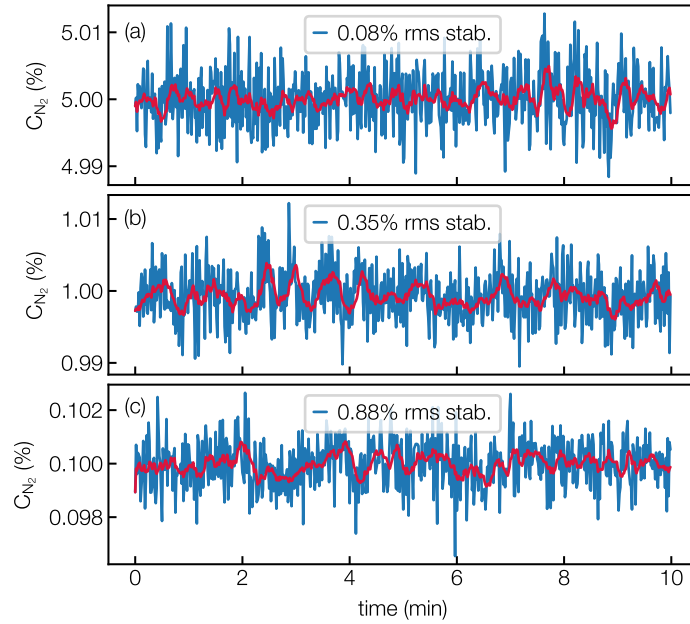
Figure 4.10 – Stability of the gas mixing device for nitrogen concentrations of 5 % (a), 1 % (b) and 0.1 % (c) recorded over 10 minutes at an output flow rate of $0.5\,l_n/min$. Blue lines show single shot data and the red lines a rolling mean over 10 seconds.

$$n_e = 2n_{at}\left[(1 - C_{N_2}) + 5C_{N_2}\right], \tag{4.7}$$

where n_{at} is the neutral atom density and C_{N_2} the nitrogen concentration [113]. Here, it is assumed that the plasma is formed from full ionization of hydrogen and the five nitrogen L-shell electrons by the leading edge of the laser pulse, see section 2.2.

Figure 4.11 shows a 2D map of the achievable plasma densities calculated with eq. 4.11 from measured flows rates and capillary pressures for nitrogen concentrations between 0 % and 5 %. With the specific mass flow controllers and the plasma target, the highest achievable plasma density at LUX is $\sim 4 \times 10^{18}\,cm^{-3}$ at a nitrogen concentration of 5 %.
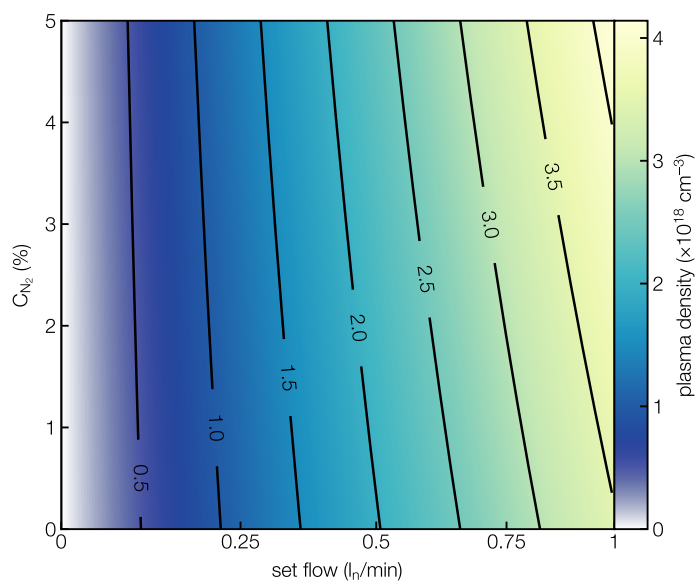
Figure 4.11 – Plasma density as a function of inlet flow rates and nitrogen concentration, calculated from measured inlet flow rats and resulting capillary pressures using eq. 4.7.

5 Injection and Acceleration Dynamics from PIC Simulations

A set of Particle-In-Cell (PIC) simulations was performed to analyze the injection and acceleration dynamics in the newly designed plasma target presented in chapter 4. The simulation environment and the input parameters are presented in section 5.1. The longitudinal dynamics of electron beam generation and laser pulse modulation are discussed in section 5.2, followed by a discussion of the evolution of the transverse electron beam parameters along the plasma target in section 5.3. There, the focus is on the plasma density ramp at the exit of the plasma target matching the betatron motion of the electrons into vacuum and reducing the beam divergence. These findings allow for a more confident interpretation of the experimental results presented in chapter 7.

5.1 PIC Simulation Environment

Simulations were performed with the code FBPIC [114]. In contrast to other PIC algorithms, FBPIC uses a set of 2D radial grids instead of a full 3D cartesian grid. Each radial grid represents a single azimuthal mode of a Fourier decomposition of the fields. For a near symmetrical problem, only the lowest modes are relevant, and thus, allows to transform a complex 3D problem to a low number of 2D problems. In addition, FBPIC simulations can be run in the boosted frame using a Lorentz transformation where the reference frame is moving with the velocity close to the speed of light. Compared to the lab frame, the laser pulse therefore appears to be stretched and the plasma target compressed, which reduces the required time steps in the simulation. Both, the reduction to a 2D problem as well as the boosted frame drastically reduce computational time and allow for extensive parameter scans.

The moving frame in the following simulations had a dimension of $100\,\mu\mathrm{m} \times 220\,\mu\mathrm{m}$ in the longitudinal z respectively transverse plane r and a total of 6000×660 grid points. The boost factor of the Lorentz transformation was set to $\gamma = 4$. Laser parameters and plasma properties were chosen to closely reproduce experimental conditions and are summarized in table 5.1.

Table 5.1 – PIC simulation Input laser parameters and plasma properties.

laser parameters			
E_l	w_0 (FWHM)	τ (FWHM)	a_0
1.7 J	27 μm	37 fs	1.56
plasma properties			
n_e	C_{N_2}	z_{focus}	
$2.54 \times 10^{18} cm^{-3}$	1 %	3.04 mm	

The laser was represented by linearly polarized pulses with a flat top intensity profile in the near-field, a FWHM pulse duration of 37 fs and an in-vacuum focal spot size of 27 μm. The laser pulse energy was set to 1.7 J ($a_0 \sim 1.56$). The longitudinal plasma density profile was derived from CFD simulations, see section 4.2.3. The background plasma was formed from a 99 % H_2+1 % N_2 gas mixture. The plateau plasma density was set to reach 2.54×10^{18} cm^{-3} after pre-ionization of hydrogen and the five nitrogen L-shell electrons. The vacuum focus was positioned in the electron density up-ramp, corresponding to $z = 3.04$ mm in figure 5.1. Electron bunch properties were derived from particles trapped in the first bucket with an energy cut-off below 25 MeV. The maximum bunch energy is given where the peak charge density has decreased by 90 % at the highest electron energy.

5.2 Longitudinal Injection and Acceleration Dynamics

This section discusses the longitudinal evolution of the laser spot size w, the intensity a_0 as well as the total charge Q_{tot} and the maximum energy E_{max} of the electron bunch along the plasma target. These parameters are shown alongside the longitudinal plasma density profile derived from CFD simulations in figure 5.1. The vertical lines labeled a-f in figure 5.1 show the positions to which the panels in figure 5.2 correspond to.

Laser Pulse Properties
Figure 5.1a shows that the laser pulse undergoes strong self-focusing during the first four millimeters of propagation since the vacuum pulse power is ~ 4 times larger than the critical power required for self-focusing. As a result, the spot size decreases compared to the vacuum spot size by by nearly a factor of 3, which in turn increases the laser intensity by a factor of ~ 2. The maximum normalized vector potential of $a_0 = 3.5$ is reached close to the center of the density plateau at $z = 3.8$ mm. The oscillation between $z = 4$ mm and

$z = 6\,\text{mm}$, where the spot size first increases before decreasing shortly afterwards again, shows that the laser pulse is not perfectly guided. This is not caused by an error in the simulation but by not perfectly matched laser spot size and plasma density and thus also expected to occur in the experiments.
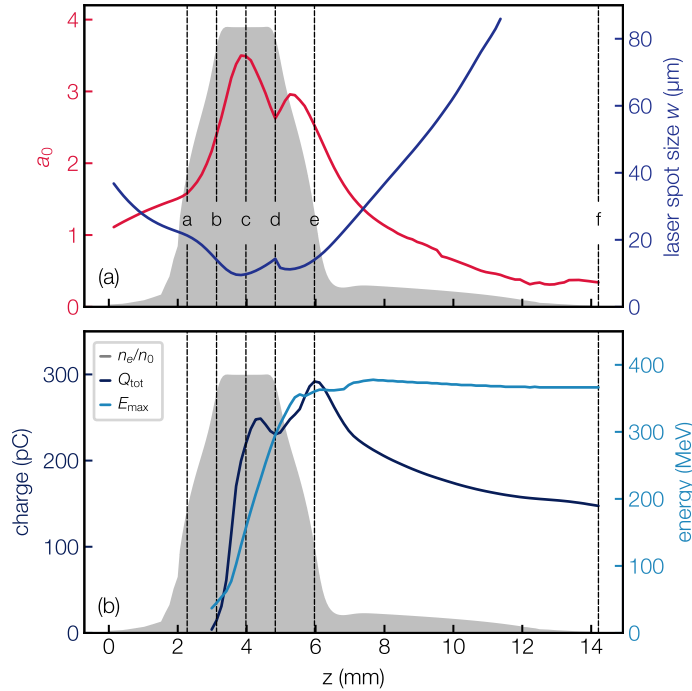
Figure 5.1 – Evolution of laser spot size w (blue) and normalized vector potential a_0 (red) as a function of the longitudinal position z in the plasma target (a). Evolution of total bunch charge Q_{tot} (blue) and maximum bunch energy E_{max} (teal) in the plasma target (b). The gray shaded areas indicate the normalized plasma density profile derived from CFD simulations. The vertical lines labeled a-f show the positions where the panels in figure 5.2 are taken from.

Electron Beam Parameters

Figure 5.1b shows that electrons are trapped and reach energies of $\sim 25\,\text{MeV}$ at $z \sim 3.1\,\text{mm}$. At this position, the normalized vector potential is $a_0 \sim 2.4$. This is below the self injection threshold of plasma background electrons of $3 \lesssim a_0 \lesssim 4$ but above the appearance intensity of the first nitrogen K-shell electron N^{6+} with $a_0 = 2.18$. Although the simulations did not allow to distinguish between different particle species, this confirms that the injected charge originates from ionization of the nitrogen K-shell. In addition, a simulation performed with pure hydrogen, but otherwise identical parameters, did not show self-injected electron bunches. Electrons keep being injected over the subsequent

$\sim 3.1\,\text{mm}$, until the bunch charge is maximized at $z \sim 6\,\text{mm}$. The bunch charge afterwards decreases again, showing that trapping is suppressed and electrons slip out of the accelerating phase of the wakefield. The bunch energy is maximized at $z \sim 7.7\,\text{mm}$ and stays nearly constant afterwards. Acceleration is terminated at this position by beam loading which cancels out the laser wakefield.

Electron Phase-Space

A deeper understanding of the injection mechanism can be gained from the electron density modulation and the longitudinal electron phase-space distribution, illustrated in figure 5.2.
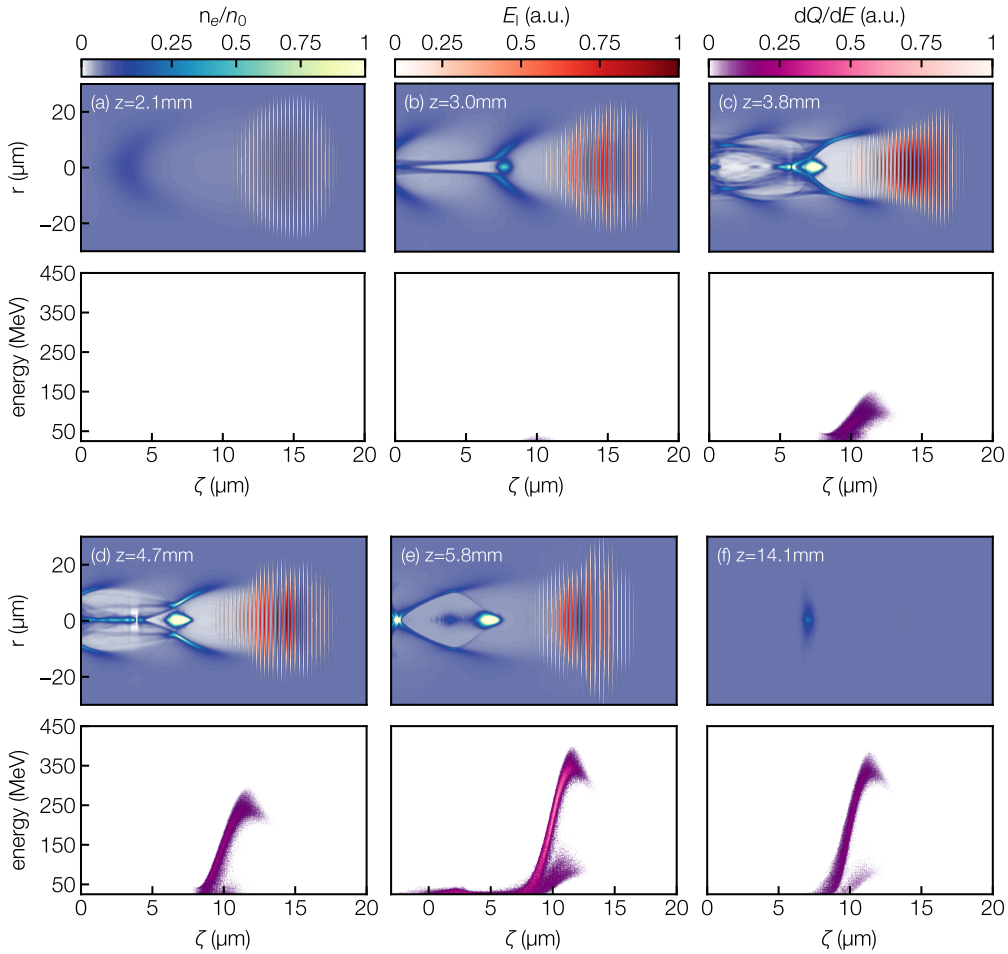
Figure 5.2 – Evolution of the normalized electron density modulation, the laser electric field (top) and electron phase-space (bottom) in longitudinal direction z in the plasma target. The panels correspond to the positions marked with a-f in figure 5.1. The electron density modulation is shown in the co-moving frame of the laser pulse $z - v_g t$, whereas the electron-space space is shown as function of relative bunch coordinate ζ.

The top rows show the density modulation and the laser electric field in the co-moving frame of the laser pulse, whereas the electron phase-space (bottom rows) is plotted as a function of relative longitudinal bunch position ξ. The snapshots correspond to longitudinal positions z marked a-f in figure 5.1.

The snapshot taken at $z = 2.3\,\mathrm{mm}$ in figure 5.2a shows the electron density modulation in an early stage of the laser-plasma interaction. The wakefield starts to form behind the laser pulse which has not yet undergone significant self-focusing. The ion column is not fully formed and no electrons are injected. Electrons are injected at the rear of the first bucket at $z = 3.1\,\mathrm{mm}$, see figure 5.2b. The bunch charge at this position is $\sim 220\,\mathrm{pC}$, which is already sufficiently high to modulate the laser wakefield, as seen by the "v" shaped opening at the rear of the first bucket. Electrons keep being injected over the subsequent few millimeters and a bunch with positive energy chirp is formed at $z = 3.8\,\mathrm{mm}$, see figure 5.2c. Figure 5.2c and figure 5.2e show the drawback of the continuously doped plasma background. Electrons are injected over the whole plasma length when the laser intensity is high enough to ionize the inner shell electrons of the high-Z gas. This spread in injection time and phase results in a continuous longitudinal electron phase-space at the exit of the plasma target, see figure 5.2f.

Although beam loading is clearly present in the simulation, not enough charge is injected over a short distance to terminate further trapping without completely suppressing the accelerating fields. Thus, injection and acceleration are not decoupled. Electron beams generated with ionization injection in such a single stage plasma target hence typically exhibit a broad energy. However, experimental results and additional PIC simulations presented in chapter 7 reveal that the concentration of the high-Z gas determine electron phase-space rotation. This allows for enhancing the electron beam quality by precisely matching laser and plasma parameters.

5.3 Transverse Electron Beam Parameters

As elaborated before, the bunch continues to drive a wakefield in the plasma density ramp at the exit of the plasma target while the laser wakefield is already depleted and diffracted. This also affects the transverse electron beam parameters, especially the beam divergence. The top plot in figure 5.3a shows the evolution of horizontal x'_{rms} and vertical y'_{rms} beam divergence after acceleration in the plasma density ramp.

First, it is noticeable that the beam divergence in the laser polarization direction x'_{rms} is a factor of two larger than in the orthogonal plane y'_{rms}. This is characteristic for ionization injection and caused by the interaction of the electrons and the laser electric field while

being ionized and traversing to the rear of the bucket, see section 2.3.2. This was observed since the first experimental studies of ionization injection and sets an intrinsic limit to the achievable beam divergence and beam emittance out of the plasma target [34].

Second, the beam divergence decreases in both planes by nearly a factor of 9 in the plasma density ramp starting at $z \sim 5 \, \text{mm}$. The reason being are the slowly decreasing focusing forces of the wakefield matching the electron beam size into vacuum.
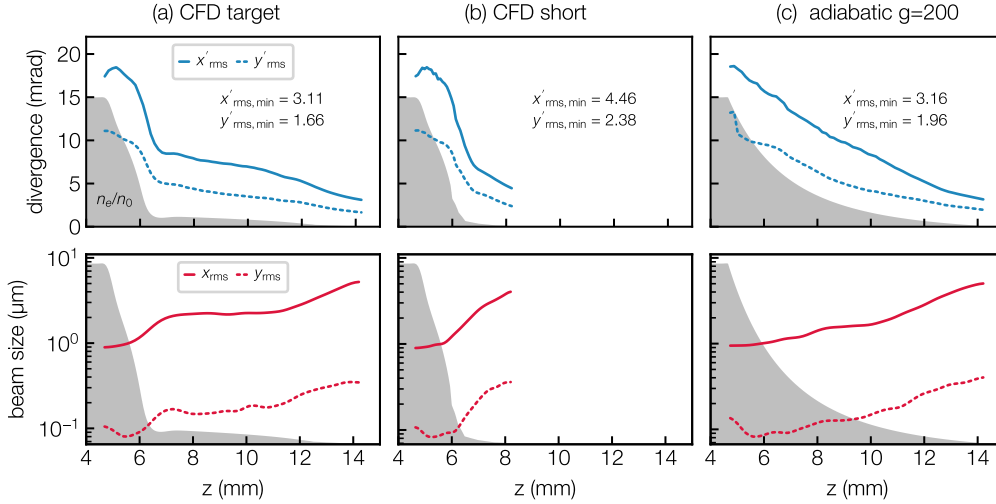
Figure 5.3 – Evolution of the transverse rms beam divergence (top row) and rms beam size (bottom row) in the plasma density ramp at the exit of the plasma target for various plasma ramp profiles. Plasma density ramp of the actual plasma target derived from CFD simulations (a). Longitudinal plasma profile with sharp plasma-vacuum transition (b). Plasma density profile with an adiabatically decreasing exit ramp calculated with eq. 5.3 for $g = 200$ (c).

The transverse rms beam size can be obtained from the beta function $\beta = \langle x^2 \rangle / \varepsilon_x$ with $\varepsilon = \sqrt{\langle x^2 \rangle \langle x'^2 \rangle - \langle xx' \rangle^2}$ being the transverse beam emittance, x and x' the electron position and direction, respectively, see section 3.4.4. A beam is matched to the focusing forces K if $\beta = 1/\sqrt{(K)}$, which implies a constant beam envelope. This is the case during acceleration where strong focusing forces from the wakefield are present. The beam size is small and the beam divergence therefore large. If the focusing forces vanish abruptly, the beam will expand rapidly in free drift. This can be counteracted by adiabatically decreasing the focusing forces before the beam enters vacuum and free drift. Adiabatically means that the decrease is on a length scale is smaller then the transverse motion of the electrons, implying matched conditions. From the scaling of the focusing forces with the plasma density, i.e.

$$K \propto - k_p \exp(-k_p^2), \tag{5.1}$$

$$k_p \propto \sqrt{n_e}, \tag{5.2}$$

it is seen that this can be achieved by gradually decreasing the longitudinal plasma density before the electron beam exits the plasma target [95]. The bottom plot in figure 5.3a shows that the beam size in fact increases in the plasma density ramp at the exit of the plasma target. As the emittance is conserved, this results in a decreases of the beam divergence (top plot). Such an adiabatic extraction section was proposed in previous work [94, 95, 115]. The ideal plasma density profile in the extraction section was found to follow

$$n_e(z) = n_0 \left(1 + 3.45gz + 1.59g^2z^2\right)^{-2}, \tag{5.3}$$

where g is the adiabatic damping factor fulfilling the condition $g\beta_0 \ll 1$ with β_0 being the beta function at the beginning of the extraction section [95]. In order to verify that the plasma density ramp in fact is the reason for the reduced beam divergence, two additional simulations with different plasma density ramps have been performed. In both cases, only the plasma density ramp was changed while keeping the up-ramp at the entrance of the plasma target as well as the plasma density plateau constant. This ensures similar electron beam parameters after acceleration. A symmetric plasma density profile was modeled where the plasma density up-ramp and half of the plateau were mirrored. This corresponds to a plasma target without the extra cut-out volume at its exit. In the second case, the shape of the plasma density ramp was modeled according to equation 5.3 with $g = 200$. The symmetric plasma density profile results in the largest beam divergence amongst the three simulated cases, see figure 5.3b. The simulated electron beam divergences decrease towards the same values in case of the adiabatically decreasing plasma density ramp in figure 5.3c and the plasma density ramp of the actual plasma target, see figure 5.3c. Although the plasma ramp of the designed plasma target noticeably reduces the beam divergence and is close to the adiabatic case with $g = 200$, a further reduction might be achieved by varying g.

5.4 Energy Dependent Phase-Space Parameters

Figure 5.4 shows the horizontal x'_{rms} and vertical beam divergence y'_{rms} as well as the horizontal normalized beam emittance $\varepsilon_{\mathrm{n},x}$ for various energy intervals of $\pm\,5\,\mathrm{MeV}$ along the energy spectrum. The phase-space parameters are not constant and decrease towards higher energy. As was illustrated with the longitudinal phase-space distributions

in figure 5.2, high-energy electrons are located at the head of the bunch. These electrons experience the unperturbed laser wakefield, while low-energy electrons experience the modulated wakefield due to beam loading. Thus, focusing forces are not constant and phase-space parameters vary along the bunch.
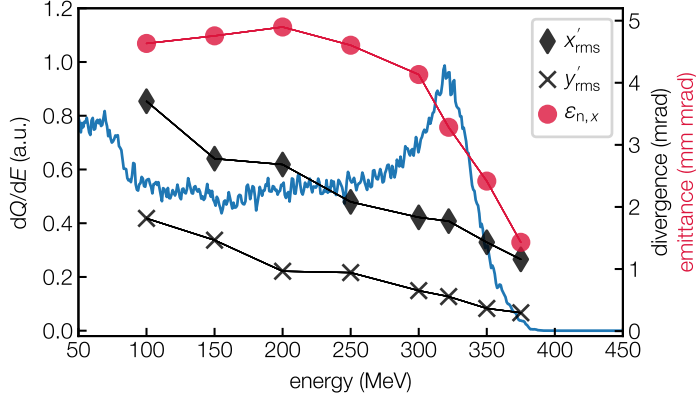
Figure 5.4 – Energy dependent electron phase-space parameters. Horizontal $x'_{\rm rms}$ (diamonds) and vertical $y'_{\rm rms}$ beam divergence (crosses) and normalized horizontal beam emittance $\varepsilon_{{\rm n},x}$, for energy slices of $\pm 5\,{\rm MeV}$ along the energy spectrum (blue). Simulation input parameters are listed in table 5.1.

Simulations reveal that energy resolved phase-space diagnostics are required to fully characterize electron beams and to optimize a preferred energy range in the experiment. Typically, the beam optics are set to transport and focus the high-energy peak in the spectrum showing the highest charge density. Simulations confirm that this is the preferred part of the energy spectrum as the beam divergence and beam emittance are smaller than for the low-energy tail. A technique allowing for energy resolved phase-space measurements was introduced in section 3.4.4 and experimental results are presented in section 7.5.

6 Experimental Electron Beam Parameters

Following the discussion on the injection and acceleration dynamics in the designed plasma target with PIC simulations in chapter 5, the experimental electron beam parameters are introduced in this chapter. The injection threshold for ionization injection is determined in section 6.1. The characteristic energy spectrum and the transverse beam profile of the generated electron beams are presented in section 6.2 and section 6.3, respectively. The stability of the accelerator and sources for shot-to-shot variations in electron beam properties are discussed in section 6.4.

6.1 Ionization Injection Threshold

The ionization injection threshold was determined by gradually increasing the laser pulse energy at constant plasma density and nitrogen concentration of $2.35 \times 10^{18} \, \text{cm}^{-3}$ and 1%, respectively. The on-target laser pulse energy is derived from the energy measured at the pulse compressor input, multiplied by 60% to account for transmission losses in the laser transport beamline. A laser spot size of $26.5 \, \mu\text{m}$ and a pulse duration of $36.5 \, \text{fs}$ were measured upfront at the pre-target laser diagnostics. The critical power for self-focusing for these laser and plasma parameters is $\sim 12.9 \, \text{TW}$, corresponding to a laser pulse energy of $\sim 0.48 \, \text{J}$. Electron beams were detected with the first Beam Position Monitor (BPM1).

Figure 6.1 shows the measured bunch charge as a function of the normalized vector potential a_0, calculated with eq. (2.4). The dashed black line indicates that electron beams were detected for $a_0 \gtrsim 1.38$. The obtained threshold is $\sim 40\%$ lower than the required normalized vector potential of $a_0 \sim 2.18$ to fully ionize the first nitrogen K-shell electron N^{6+}. However, when injection starts, the laser power is ~ 2.5 times larger than the critical power required for self-focusing. Thus, the laser intensity in the plasma increases as the laser spot size is reduced and eventually is sufficient high for ionization. The linear increase of the bunch charge with the normalized vector potential afterwards is caused by a larger ionization volume, associated with higher laser intensities, and confirms that the injected electrons in fact originate form the nitrogen K-shell. The shot-to-shot variations of the bunch charge increase with the laser strength parameter,
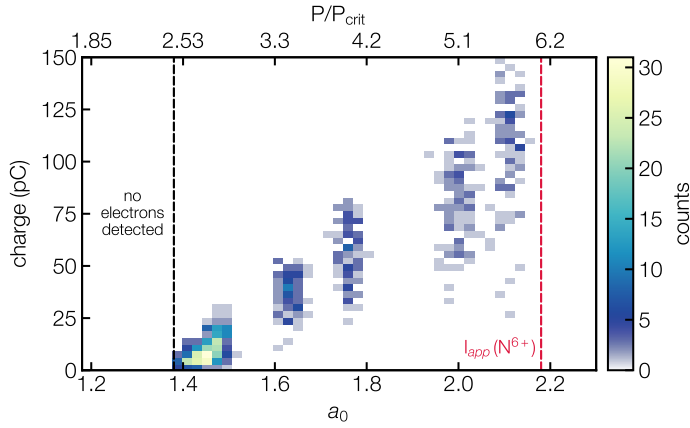
Figure 6.1 – Bunch charge $>2\,\mathrm{pC}$ measured with BPM1 as a function of the normalized vector potential a_0. The black dashed line indicates the injection threshold of $a_0 \sim 1.38$. The red dashed line shows the required a_0 of ~ 2.18 to ionize the first nitrogen K-shell electron N^{6+}. The secondary x axis shows the laser power P normalized to the critical power required for self-focusing P_{crit}.

as the accelerator is operated near the beam loading limit and electron trapping becomes inefficient at high laser intensities.

The measured injection threshold is $\sim 20\,\%$ lower than previously reported by A. Pak et al. [34]. The difference is most likely caused by the sensitivity of laser and electron beam diagnostics. For example, they only considered the charge of electrons with an energy above $25\,\mathrm{MeV}$, whereas the BPM, used for the charge measurement in the above presented results, is independent of the electron energy. In addition, the composition of the plasma, i.e. the plasma density as well as the nitrogen concentration, affect laser self-focusing and hence the laser peak intensity reached in the plasma target [116]. The measured injection threshold of $a_0 \sim 1.38$ can thus not be understood as an absolute value for ionization injection, but as an guideline for the operation of the LUX accelerator.

6.2 Characteristic Energy Spectrum

Figure 6.2 shows the characteristic energy spectra of the generated electron beams. The top row shows the projected energy spectra of 100 consecutive electron beams in a waterfall plot. Each of the two columns below show single shot energy spectra extracted from the beginning respectively end of the dataset. The energy spectra clearly reflect the injection and acceleration dynamics discussed with PIC simulations, i.e. a high-energy peak formed from early trapped electrons and a low-energy tail caused by continuous injection of nitrogen K-shell electrons.
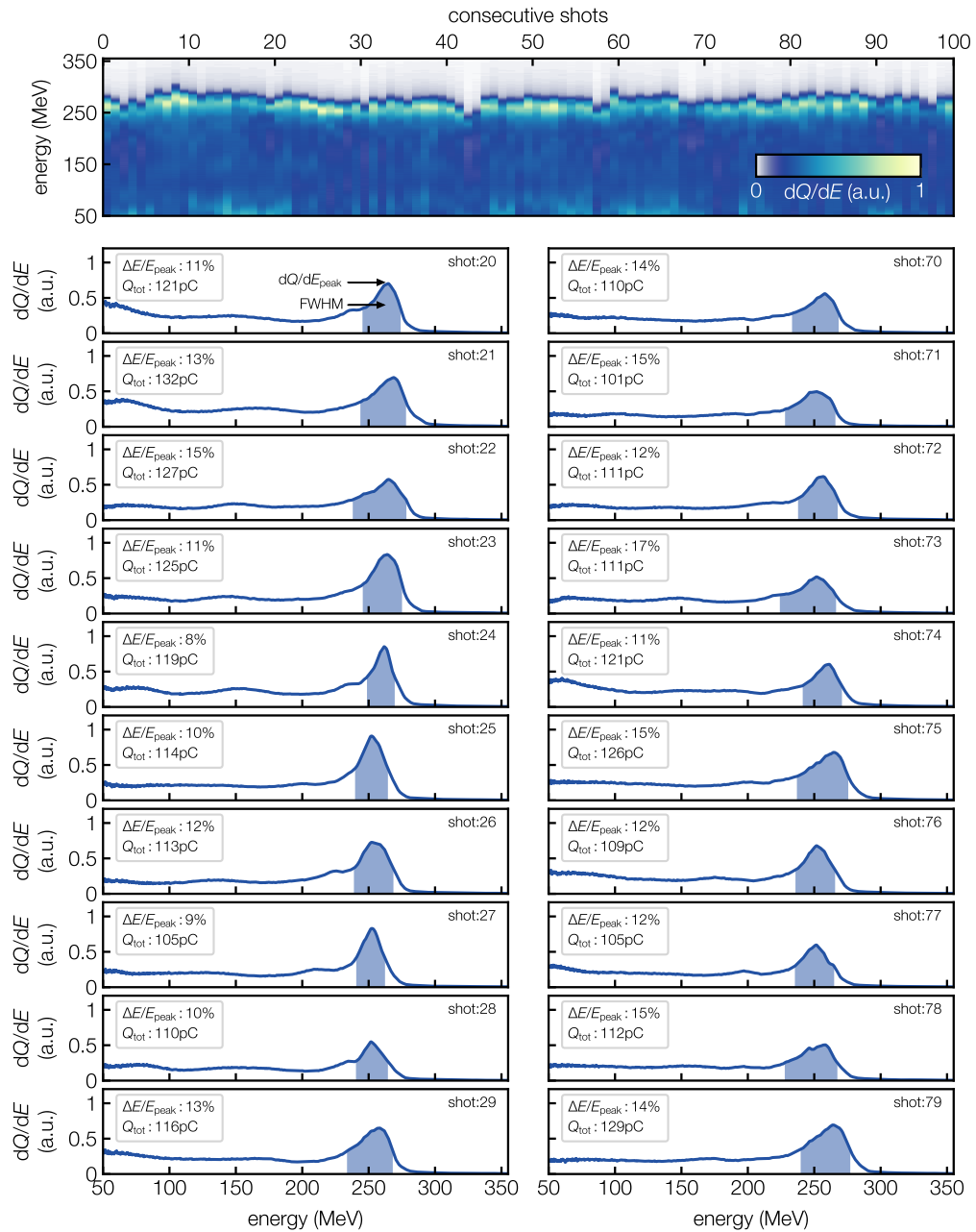
Figure 6.2 – Characteristic energy spectra of electron beams generated with ionization injection in the plasma target introduced in chapter 4. Waterfall plot of 100 consecutive shots (top plot). The colormap shows the charge density. Single shot energy spectra extracted from the beginning and end of the dataset (left and right columns). The shot numbers are displayed in the upper right corners. The blue shaded areas indicate the relative FWHM energy spread of the high-energy peak. Electron beams were generated with a plasma density of $2.47 \times 10^{18}\,\mathrm{cm}^{-3}$, a nitrogen concentration of $1\,\%$ and a laser pulse energy of $1.76\,\mathrm{J}$.

To better compare the accelerator performance depending on the laser-plasma configuration in chapter 7, the following key parameters are extracted from each shot individually. Peak energy E_{peak} and peak charge density $\mathrm{d}Q/\mathrm{d}E_{\text{peak}}$ are derived from the energy and the value where the projected signal of the spectrometer screen image $\mathrm{d}Q/\mathrm{d}E$ is maximized. As mentioned before, the charge density can only be given as a relative measure as the electron spectrometer screen was not charge calibrate during the course of the experimental campaign performed within this thesis. The absolute, respectively relative energy spread ΔE and $\Delta E/E_{\text{peak}}$ are given where the hight of the high-energy peak is first reduced by a factor of two. This yields a mean peak energy of $(260 \pm 8)\,\text{MeV}$ with a relative energy spread of $(14.5 \pm 4)\,\%$ and a bunch charge of $(120 \pm 11)\,\text{pC}$ for the presented dataset.

The high-energy peak is the relevant part of the spectrum, especially when using electron beam optics acting as an energy filter. Thus, the work presented in chapter 7 is aimed to optimize the high-energy peak.

6.3 Characteristic Transverse Electron Beam Profile

The single shot horizontal x'_{rms} and vertical y'_{rms} rms beam divergence of 100 consecutive shots are shown in the top row in figure 6.3. The beam divergence was measured with ESS1 and corrected with the calibration factor of 2.3 to account for the limited charge sensitivity of the screen station, see section 3.5. The two bottom rows each show single shot beam profiles extracted from the beginning and end of the dataset, respectively.

The mean beam divergence in the horizontal plane was $x'_{\text{rms}} = (1.57 \pm 0.15)\,\text{mrad}$, which is ~ 2 times larger than the vertical beam divergence of $y'_{\text{rms}} = (0.77 \pm 0.06)\,\text{mrad}$. The asymmetric beam profile is typical for ionization injection and was already observed in the first published experimental results [34]. It is caused by electrons gaining additional momentum in the laser polarization direction while being ionized inside the laser field, see section 2.3.2.

Not only an optimized energy spectrum is important for the operation of an accelerator, but also a small beam divergence and beam emittance are required for electron beam transport and phase-space manipulation with electron beam optics. Experimental results on the influence of the laser-plasma configuration on the transverse electron beam parameters are presented in chapter 7.
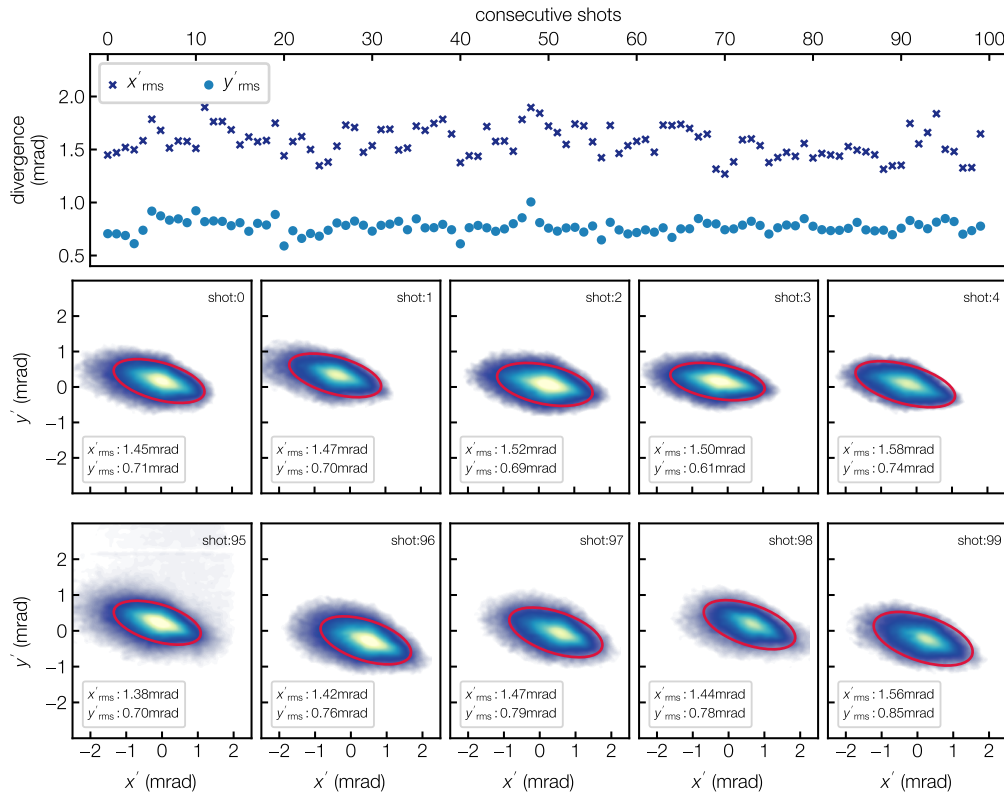
Figure 6.3 – Characteristic transverse electron beam profile. Horizontal x'_{rms} and vertical y'_{rms} beam divergence of 100 consecutive shots (top). Single shot transverse electron beam profiles extracted from the beginning and end of the dataset (bottom rows). The shot numbers are displayed in the upper right corners. The red ellipse shows the 2D Gaussian fit function from which the rms beam divergence is derived. Electron beams were generated with a plasma density of $2.47 \times 10^{18}\,\mathrm{cm}^{-3}$, a nitrogen concentration of $1\,\%$ and a laser pulse energy of $1.76\,\mathrm{J}$.

6.4 Accelerator Stability

The accelerator has to provide a high shot-to-shot stability to perform parameter scans with several tens of consecutive electron beams to ensure statistic relevance of datasets, as well as for the long time operation of the LUX beamline. Shot-to-shot instabilities can arise from fluctuations of the laser parameters and plasma properties. The pressure in the plasma target was monitored online during the experimental campaign. Pressure and hence plasma density fluctuations were below $1\,\%$ due to the operation with continuous gas flow. In addition, measurements presented in section 4.4 showed that the stability of the hydrogen-nitrogen gas mixture is also on the sub percent-level. Plasma properties are therefore assumed to be constant within the resolution of the diagnostics and it is

Table 6.1 – Mean laser and electron beam parameters and rms shot-to-shot variations. The corresponding energy spectra and transverse electron beam profiles are shown in figure 6.2 and figure 6.3. Mean values and rms jitters are given for 100 consecutive shots.

parameter	mean value	rms jitter
electron beam parameters		
Peak energy E_{peak}	260 MeV	$\pm\,4\,\%$
Bunch charge Q_{tot}	120 pC	$\pm\,9\,\%$
Pointing x'_{e}	0	$\pm\,0.42$ mrad
Pointing y'_{e}	0	$\pm\,0.3$ mrad
laser parameters		
pulse energy	1.76 J	$\pm\,1.3\,\%$
pointing x'_l	0	$\pm\,0.13$ mrad
pointing y'_l	0	$\pm\,0.11$ mrad
focus position x_{l}	0	$\pm\,1.8\,\mu$m
focus position y_{l}	0	$\pm\,3\,\mu$m
focus position z_{l}	0	$\pm\,230\,\mu$m
$0°$ astigmatism	0	$\pm\,7$ nm
$45°$ astigmatism	0	$\pm\,7.2$ nm

focused on the effect of laser parameter fluctuations on the electron beam parameters in the following discussion.

Table 6.1 lists the mean laser and electron beam parameters and the rms jitter over 100 consecutive shots. The corresponding energy spectra and transverse electron beam profiles are shown in figure 6.2 and figure 6.3. Horizontal x'_1 and vertical y'_1 laser pointing into the target as well as horizontal x_1 and vertical y_1 laser position in the plasma target are derived with the near- and far-field monitors installed behind the focusing parabola, see section 3.2.1. The calibration was done by C.Werle [60]. The longitudinal laser focus position z_{l}, $0°$ and $45°$ astigmatism were measured with the wavefront sensor installed behind the pulse compressor.

Correlations between the relative change of these laser and electron beam parameters are shown with Pearson correlation coefficients in figure 6.4. The Pearson correlation is a unitless number between -1 and 1, and indicates how strongly two variables are linearly related. Pearson coefficients below 0.2 were set to zero to identify the most pronounced

	$\Delta Q_{tot}/Q_{tot}$	$\Delta E_{peak}/E_{peak}$	$\Delta x_e'/x_e'$	$\Delta y_e'/y_e'$
pulse energy E_l	0.00	0.00	0.24	0.00
laser pointing x_l'	0.00	0.00	0.00	0.00
laser pointing y_l'	0.00	0.00	0.00	0.00
focus position x_l	0.00	0.00	0.00	0.00
focus position y_l	0.00	0.00	0.00	0.00
focus position z_l	0.23	0.36	0.00	0.00
0° astigmatism	0.00	0.00	0.00	0.20
45° astigmatism	0.00	0.00	0.23	0.00

Figure 6.4 – Pearson correlation coefficients between relative change of laser and electron beam parameters.

correlations.

The longitudinal laser focus position is the underlying cause for instabilities in peak energy and bunch charge. This is expected as the focus position determines laser self-modulation and hence the laser peak intensity in the plasma. Experimental results presented in section 7.2 underline this assumption and show that the longitudinal laser focus position allows to tune electron beam parameters.

Electron beam pointing jitter is caused by 0° and 45° astigmatism. These low order laser wavefront aberrations cause an inhomogeneous intensity profile in the focal plane. Previous results suggested that such aberrations can lead to an asymmetrically shaped wakefield [19]. As a consequence, electrons are accelerated under an angle with respect to the laser propagation direction and exit the plasma target with a mean pointing [21, 117]. Horizontal electron beam pointing jitter further correlates with the laser pulse energy. This implies that the asymmetry of the wakefield is also influenced by the laser intensity. It is noted that temporal and spectral laser pulse properties were not accessible online during the experimental campaign but are expected to also affect the stability.

The results show the advantage of the designed single stage plasma target, operated with ionization injection. Electron beams show percent-level stability in peak energy and bunch charge, combined with sub mrad pointing jitter, although fluctuating laser parameters. Such a high accelerator stability allowed for extensive parameter scans and to record 100, respectively 200 consecutive electron beams at each setting, ensuring high statistic relevance. The results of these parameter scans are presented in chapter 7.

7 Results on Electron Beam Generation

Tunable and stable electron beam generation is crucial to set up and operate a laser-plasma accelerator on a daily basis as well as to commission and to calibrate new diagnostics. As the LUX beamline is designed for the generation of spontaneous undulator radiation and for a future upgrade to demonstrate FEL gain, it is further necessary to enhance the beam quality for transport and phase-space manipulation with electron beam optics. This means to optimize the high-energy peak of the energy spectrum in terms of energy spread and charge density and to reduce the beam divergence and beam emittance.

This chapter covers the results of the experimental campaign conducted in January 2019 at the LUX facility, focused on controlled electron beam generation with ionization injection. First, in section, 7.1, it is presented how to steer electrons beams with the laser beam pointing into the plasma target, necessary to align the electron beams onto the design axis. The longitudinal vacuum focus position is derived in section 7.2.1, a prerequisite for the laser focus position scan in section 7.2.2. The influence of the plasma properties such as the plasma density and the nitrogen concentration is discussed in section 7.3 and section 7.4. The influence of the laser pulse energy on the beam emittance is sown in section 7.5. Experimental results in each section are supported with PIC simulations.

The dataset was recorded in a single beam time to exclude small variations of the driver laser in day-to-day operation and consists of over 16000 generated electron beams, ensuring high statistical relevance. The on-target laser parameters, measured at the beginning of the campaign, are summarized in table 3.1. If not otherwise stated, 100 consecutive electron beams have been recorded at each parameter setting. Outliers with variations larger than two standard deviations from the mean were excluded from the analysis. The number of remaining shots is stated in the captions of the figures.

7.1 Electron Beam Alignment

Possible sources for shot-to-shot variations of the electron beam parameters were discussed in section 6.4. It was elaborated that electron beam pointing jitter can originate from laser wavefront aberrations. The same effect can also lead to electron beams exiting

the plasma target with a mean pointing, i.e. direction. Of particular note is here pulse front tilt (PFT) where the arrival time of the pulse varies across the beam profile [118]. This can result in an asymmetrically shaped wakefield, off-axis electron acceleration and beams exiting the target under an angle with respect to the laser propagation direction [21, 117]. PFT is caused by misalignment of optical components in the laser amplification chain, especially by non parallel surfaces of optics or by a misalignment of the pulse compressor. The typical procedure to minimize PFT in preparation of an experimental campaign is to send the laser into the GRENOUILLE and to reduce the delay offset in the reconstructed FROG trace by adjusting the rotation of the pulse compressor gratings. The GRENOUILLE was briefly discussed in section 3.2.1.

However, the gratings in the ANGUS pulse compressor are only motorized in the horizontal plane. A residual PFT in the vertical plane can therefore not be minimized online. In addition, the diagnostic setup can, if not perfectly aligned, also imprint additional PFT on the pulse. A minimized PFT out of vacuum must therefore not necessarily result in a minimized PFT in vacuum. The LUX beamline is in principle equipped with a set of four dipole magnets to correct for electron beam pointing and offset. However, electrons are deflected depending on their energy. In case of broad energy spectrum, this leads to dispersion. It is thus necessary ensure that electron beams exit the plasma target on-axis in the first place to minimize the use of the corrector dipoles.

Electron beams can be steered by adjusting the laser pointing into the plasma target. For this purpose, the last two motorized mirrors in front of the focusing parabola (M3, M4 in figure 3.3) were used to change the incident angle of the laser beam onto the surface while keeping the position constant. Two cameras monitored the laser near- and far-field behind the parabola, see section 3.2.1. A shift in the near-field causes a change in direction into the target, whereas the far-field corresponds to the in transverse focus position. The diagnostic was calibrated in previous work by C. Werle [60]. Electron beam pointing is derived from the center of mass of the transverse beam profile, measured with the first electron screen station ESS1. Electron beams were generated with a plasma density of $2.5 \times 10^{18}\,\text{cm}^{-3}$, a nitrogen concentration of $1\,\%$ and a laser pulse energy of $2.3\,\text{J}$.

The correlation between laser and electron beam pointing is shown in figure 7.1. The initial horizontal and vertical beam pointing over the first 450 shots was $x'_\text{e} = (\text{-}0.3 \pm 0.6)\,\text{mrad}$ and $y'_\text{e} = (\text{-}1.2 \pm 0.2)\,\text{mrad}$, respectively. The offset from the design axis is clearly visible in the mean transverse beam profile in figure 7.1c. The vertical laser pointing y'_l was then adjusted from shot number 450 on. The electron beams follow the direction of the laser beam with a 1:1 dependency, i.e. $1\,\text{mrad}$ change in laser pointing corresponds to $1\,\text{mrad}$ change in electron beam pointing, see figure 7.2a. Figure 7.1d shows the mean transverse beam profile in the vertically aligned case between shot number 800 and 1550, with $y'_\text{e} = (0.06 \pm 0.2)\,\text{mrad}$ and $x'_\text{e} = (0.3 \pm 0.5)\,\text{mrad}$.
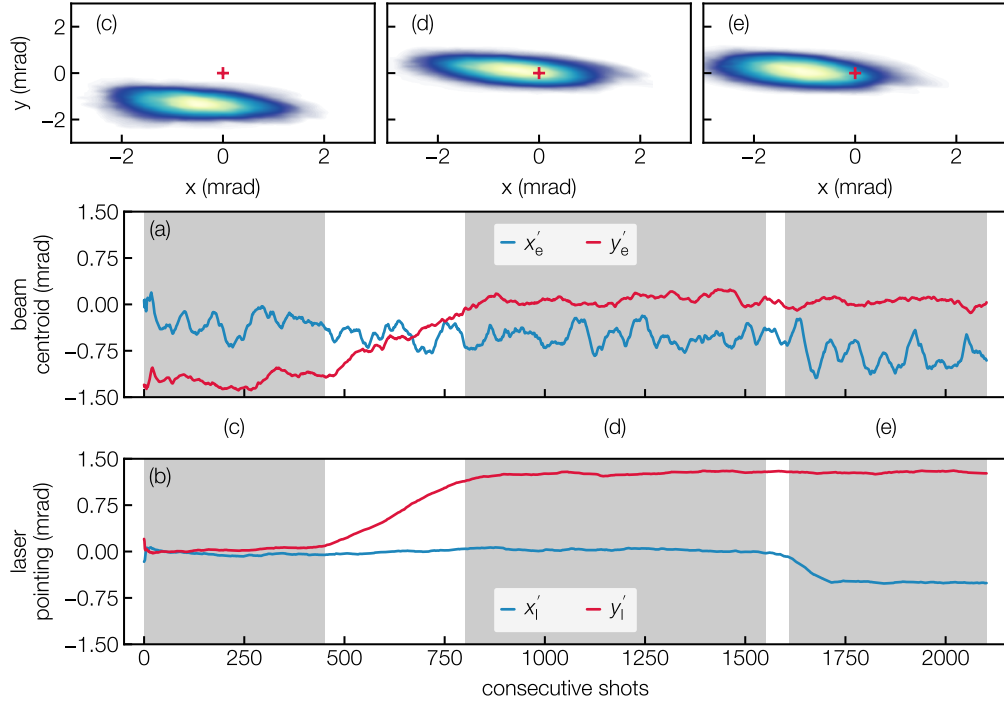
Figure 7.1 – Electron beam alignment. Horizontal x'_e (blue) and vertical y'_e (red) electron beam pointing out of the plasma target measured with ESS1 (a). Horizontal x'_l (blue) and vertical y'_l (red) laser pointing into the plasma target (b). A rolling mean over 50 shots is applied to the data. The gray shaded areas indicate where the laser pointing was actively adjusted. Transverse electron beam profiles showing the initial offset (c), the offset after vertical (d) and horizontal (e) alignment. The red crosses show the target position.

Electron beams were then purposely misaligned horizontally from shot number 1600 on to verify that steering is possible in both directions. The observed correlation between laser and electron beam pointing is $\sim 1{:}0.5$ and is not as pronounced as in the vertical direction due to the larger electron beam pointing jitter, see figure 7.2b. The difference between horizontal and vertical beam pointing jitter is most likely caused by laser wave-front aberrations or spatial temporal couplings, see section 6.4. The final electron beam position with $x'_e = (\text{-}1 \pm 0.5)\,\text{mrad}$ and $y'_e = (0.06 \pm 0.2)\,\text{mrad}$ is shown in figure 7.1e.

The results clearly demonstrate that electron beams can be actively steered by adjusting the laser pointing into the plasma target, which is crucial to compensate for initial electron beam pointing out of the plasma target and therefore to minimize the use of the corrector dipoles.
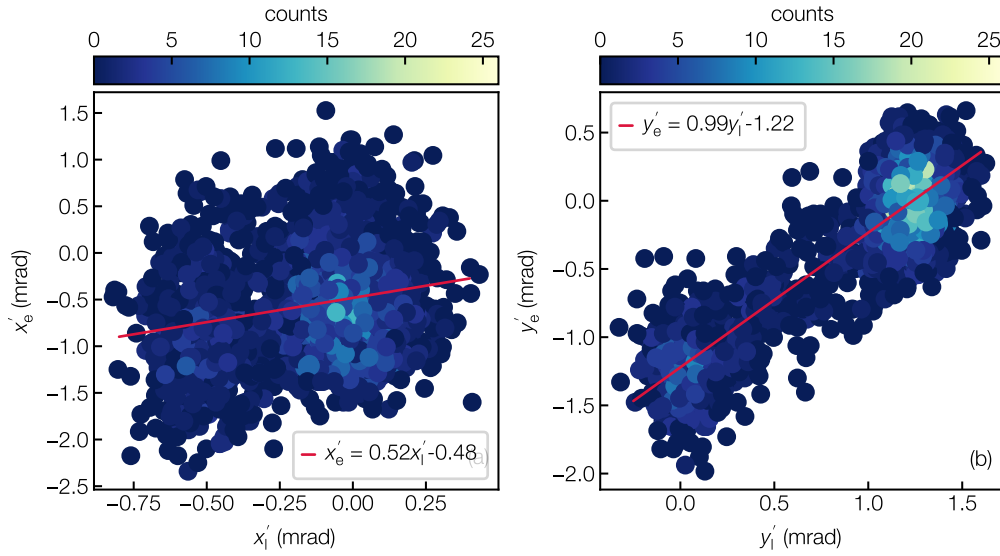
Figure 7.2 – Correlation between laser and electron beam pointing in the horizontal (a) and vertical plane (b).

7.2 Influence of the Laser Focus Position

The first important step in setting up the accelerator is to set the longitudinal focus position in the plasma target. As elaborated in section 2.4, the laser pulse undergoes self-focusing in the plasma when the peak power exceeds the critical power P_c. As a result, the vacuum focus spot size is reduced and the intensity increased. The highly non-linear process crucially affects trapping and acceleration dynamics and can not be easily predicted. Thus, the longitudinal focus position in the plasma target has to be scanned experimentally to find a suitable setting for daily operation.

This section first describes how the longitudinal laser vacuum focus position in the target chamber is determined in section 7.2.1. The effect of the longitudinal focus position, referred to as just laser focus position in the following, in combination with the laser pulse energy on the electron beam parameters is presented in section 7.2.2. PIC simulation support the experimental findings in section 7.2.3.

7.2.1 Vacuum Laser Focus Position Measurement

The vacuum laser focus position z in the target chamber was derived from the recombination light of a hydrogen plasma. The plasma target was driven out of the beam path and the laser aligned onto its design axis. The turbo molecular pumps were switched off and the target chamber was filled to millibar pressure level with hydrogen through the
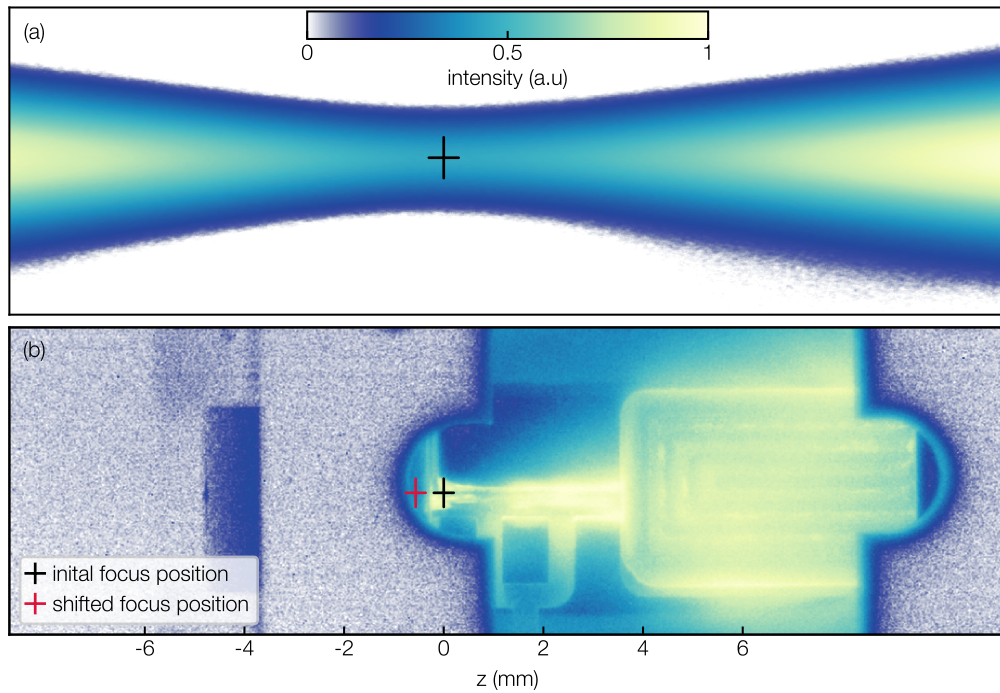
Figure 7.3 – Recombination light of the hydrogen plasma used to determine the longitudinal vacuum position (black cross) (a). Initial (black cross) and laser focus position after thermalization of the pulse compressor gratings (red cross) (b). The plasma was created at 1 mbar pressure level and with a laser pulse energy of 170 mJ. Both figures are scaled identically.

gas inlet of the plasma target. The laser pulse energy was then gradually increased until the typical recombination signal, depicted in figure 7.3a, became visible.

The image was taken with a 16 bit CCD camera through a viewport from the outside of the target chamber. A 800 nm high-pass filter was installed to suppress the laser light. Ionization is a threshold process, thus, the intensity profile mirrors the evolution of the laser spot size around the focal plane. The specific image was recorded at a laser pulse energy of 170 mJ, a focal focal spot size of 26.5 µm and a pulse duration of 37 fs. The corresponding peak intensity in the focal plane was $\sim 5.4 \times 10^{17}$ Wcm^{-2} which is three orders of magnitude larger than the appearance intensity of hydrogen ($\sim 10^{14}$ Wcm^{-2}). Ionization therefore occurs a few millimeters in front, as well as behind the focal plane where the spot size and hence the ionization volume are larger. A larger amount of hydrogen molecules is thus ionized which increases the waist of the signal . The laser focus position is therefore given where the waist is minimal and the intensity lowest, i.e. at $z = 0$ in figure 7.3a. Figure 7.3b shows the plasma target driven back into the beam path. The laser focus position is indicated with the black cross.

The laser propagates at mbar pressure level before reaching the focal plane in this oper-

ation mode. According to eq. 2.37, the critical power for self-focusing at 1 mbar pressure level is $\sim 590\,\text{TW}$, which is two orders of magnitude larger than the used peak power of $4.7\,\text{TW}$. A shift of the laser focus position close to the focal plane affecting the measurement is hence not expected.

The laser focus position was determined at reduced laser power at the beginning of the experimental campaign. The optical components and especially the pulse compressor gratings were in a cold state during the measurement. Results presented by V. Leroux et al. showed that the grating pair heats up and slightly deforms during the first few hours of high power operation [62]. These deformations changes the laser wavefront. The wavefront sensor installed behind the pulse compressor showed that the beam divergence changed between the focus position measurement and the time the thermal equilibrium was reached. As a result, the laser focus position shifted by $\sim 0.56\,\text{mm}$ to the front of the plasma target. The new laser focus position is indicated with the red cross in figure 7.3b.

7.2.2 Energy Spectrum and Bunch Charge

Figure 7.4 shows the influence of the laser focus position and laser pulse energy on the generated electron beams. The plasma target was translated longitudinally in steps of $0.25\,\text{mm}$ for a total range of $2.5\,\text{mm}$ to vary the laser focus position in the density up-ramp at the entrance of the plasma target. The laser pulse energy was increased in four steps from $1.76\,\text{J}$ to $2.83\,\text{J}$ ($1.6 \lesssim a_0 \lesssim 2$) at each longitudinal position z. The plateau plasma density was $2.47 \times 10^{18}\,\text{cm}^{-3}$ and the nitrogen concentration $1\,\%$.

Peak Energy and Bunch Charge
Shifting the focus into the plasma target, i.e. from $z = 0\,\text{mm}$ to $z = 2.25\,\text{mm}$, simultaneously increases electron energy and bunch charge. The laser pulse propagates a larger distance through regions of higher plasma density when the focus is set further into the plasma target. This leads to stronger laser self-focusing and increased laser intensity. A stronger longitudinal acceleration field E_z is thus expected from eg. 2.33, as well as a larger transverse injection volume, which increases electron peak energy and bunch charge. At constant laser focus position, peak energy and bunch charge are further enhanced with the laser pulse energy. Highest bunch charge and peak energy were therefore recorded at $z = 2.25\,\text{mm}$ and at a laser pulse energy of $2.83\,\text{J}$. The relative increase, on the other hand, is strongest for the lowest explored laser pulse energy of $1.76\,\text{J}$, see figure 7.4d. In this case, the bunch charge is increased by nearly $45\,\%$ and the peak energy by $70\,\%$. Self-focusing hence seems to increase the laser peak intensity stronger at lower laser pulse energies in the explored parameter space.

A decrease of the bunch charge and peak energy is observed for the three larger laser pulse energies when the focus is set too far into the plasma target, i.e. for $z > 2.25\,\text{mm}$,

see figures 7.4a to 7.4c. This is presumed to be caused by beam loading which makes electron injection and acceleration inefficient as the wakefield becomes fully loaded. The maximum bunch charge in the beam loading limit, estimated with eq. 2.31, is between 300 pC and 350 pC for the explored laser pulse energies between 2.11 J and 2.83 J. This is in good agreement with the measured bunch charges and thus confirms the operation in a beam loaded regime. Not enough electrons are injected to significantly load and modulate the wakefield for a laser pulse energy of 1.76 J. Hence, no decrease of the peak energy and bunch charge are observed in this case.

Energy Spread and Charge Density

No clear correlation between the charge density and the laser focus position is observed. The charge density, however, increases with the laser pulse energy, especially in the high-energy part of the spectrum. PIC simulations showed that the peak is formed from early trapped electrons, see chapter 5. The charge density is thus mainly determined by the transverse injection volume when injection starts and not by the longitudinal injection distance. As a consequence, there is also no clear correlation between energy spread and laser focus position visible.
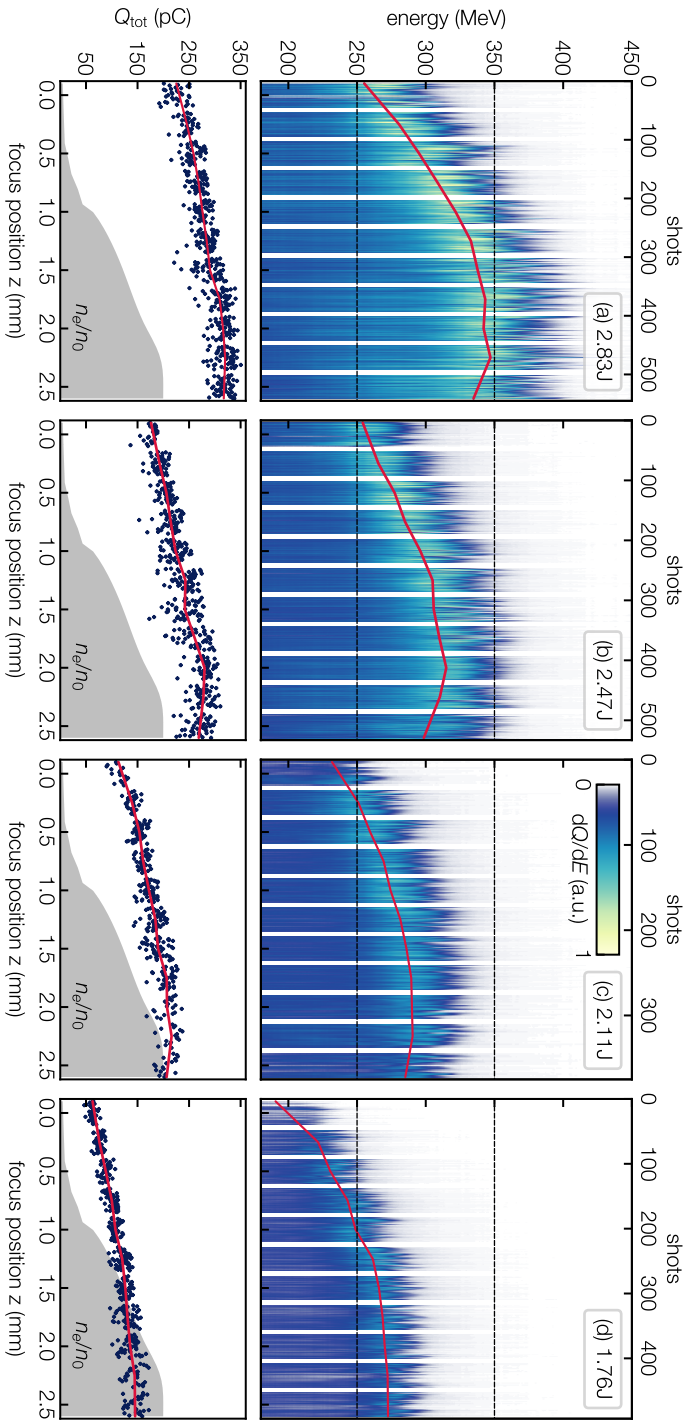
Figure 7.4 – Series of projected energy spectra (top row) and bunch charge (bottom row) as a function of the vacuum laser focus position z for laser pulse energies from 2.83 J down to 1.76 J (a-d). The colormap shows the charge density dQ/dE. Mean peak energy E_{peak} and mean total bunch charge Q_{tot} are depicted in red. The longitudinal plasma density profile is indicated with the gray shaded areas. Number of electron beam data points at each setting is between 35 and 65.

7.2.3 PIC Simulations

A set of PIC simulations was performed to verify the observed scalings. The input parameters for the simulations are listed in table 5.1, except the laser focus position which was chosen according to the experiment. Simulation results are compared to data recorded at a laser pulse energy of 2.47 J in figure 7.5. It is noted that the laser pulse energy of 1.7 J in the simulations is $\sim 30\%$ lower than in the experiment. The comparison is nevertheless reasonable as the difference can be explained by uncertainties in the measured laser parameters. Especially the energy fraction of the laser pulse actually driving the acceleration in the experiment was not directly accessible and is most likely only a fraction of the total pulse energy.
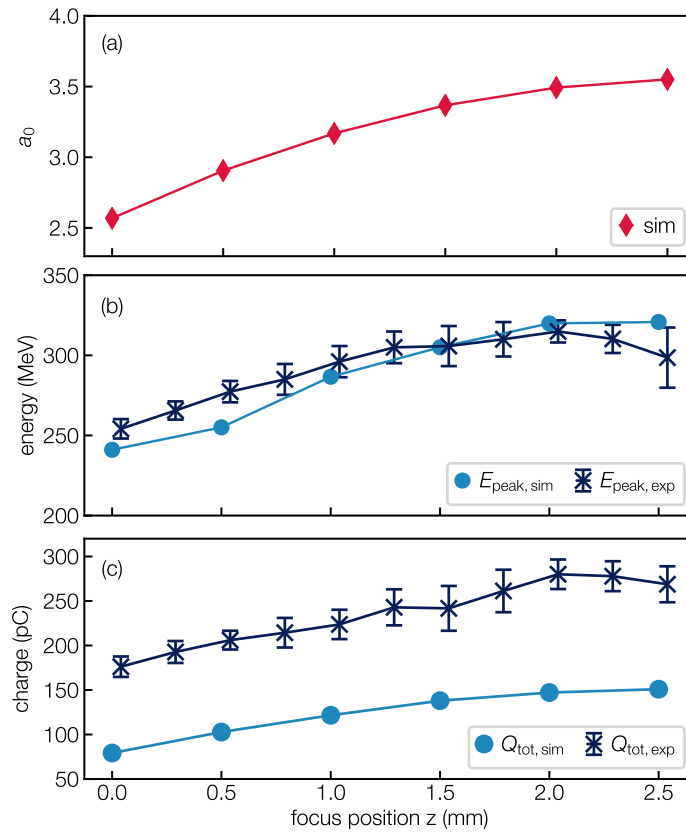
Figure 7.5 – PIC simulated Laser strength parameter a_0 as a function of the vacuum laser focus position (a). Comparison between experimental (crosses) and simulated (dots) peak energy (b) and bunch charge (c) as a function of z. PIC simulation input parameters are listed in table 5.1. Focus positions in the simulation were set in accordance to the experimental focus positions.

Although the bunch charges from the experiment are not reached in the simulations, the trends are very well reproduced. Especially the peak energies are in very good agreement. Simulations show that the focus position allows to maximize bunch charge and peak energy at constant plasma density and additionally reveal that the increase is caused by growing normalized vector potential due to enhanced laser self-focusing.

From the experimental results in combination with the PIC simulations we can draw the conclusion that the laser focus position determines self-focusing and allows to tune the accelerator. Electron beams with comparably high peak energy and bunch charge can be generated even with low laser pulse energies when the focus is set into regions of higher plasma density. Results presented in section 7.4.2 and section 7.5 show that this is of special interest to reduce the electron beam divergence and beam emittance.

7.3 Influence of the Plasma Density

The previous results revealed that the laser focus position is sufficient to maximize beam energy and bunch charge at constant plasma properties. This section shows that electron beam parameters can also be tuned with the plasma density. The influence on the energy spectrum and bunch charge are presented in section 7.3.1. Electron beams were generated at a laser pulse energy of 1.76 J and nitrogen concentration of 1 %. The dependency of the beam divergence on the plasma density is discussed with measurements on the first electron screen station (ESS1) in section 7.3.2. The laser pulse energy was increased to 2.47 J at otherwise identical parameters to ensure high bunch charge and thus a good signal to noise ration on the detection limited screen station. Beam divergence measurements are supported with PIC simulations in section 7.3.3.

7.3.1 Energy Spectrum and Bunch Charge

Peak Energy and Bunch Charge
Figure 7.6a shows that the peak energy increases by $\sim 40\,\%$ when the plasma density is raised from $2.31 \times 10^{18}\,\mathrm{cm}^{-3}$ to $3.15 \times 10^{18}\,\mathrm{cm}^{-3}$. The increase is caused by a stronger longitudinal acceleration field, expected from the scaling $E_z \propto \sqrt{n_e}$, see eq. (2.15). The bunch charge increases by $\sim 40\,\%$ with the plasma density due to a larger availability of a nitrogen K-shell electrons in the background plasma. In addition, the bunch charge is increased by stronger laser self-focusing at higher plasma densities which increases the laser intensity and hence the transverse injection volume.

Energy Spread and Peak Charge Density
The effect of the plasma density on the beam quality is shown in figure 7.6b. The peak charge density $\mathrm{d}Q/\mathrm{d}E_{\mathrm{peak}}$ and the relative energy spread $\Delta E/E_{\mathrm{peak}}$ both increase with
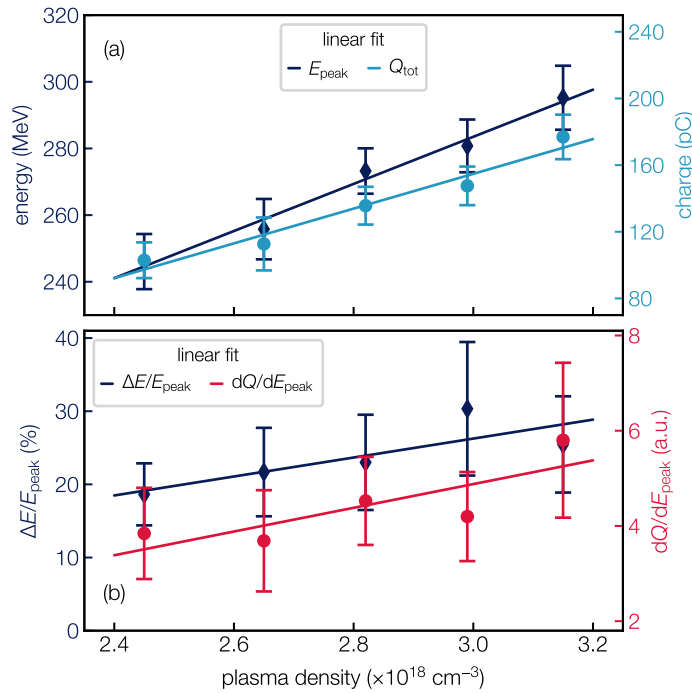
Figure 7.6 – Peak energy E_{peak} and bunch charge Q_{tot} (a), as well as relative energy spread $\Delta E/E_{\text{peak}}$ and peak charge density $\mathrm{d}Q/\mathrm{d}E_{\text{peak}}$ as a function of the plasma density. Electron beams were generated with a laser pulse energy of 1.76 J and a nitrogen concentration of 1 %. Sample size for each setting is between 49 and 80 shots. Linear fits are plotted to guide the eye.

the plasma density. This implies that due to a larger transverse injection volume and availability of nitrogen K-shell electrons, a larger amount of electrons is trapped early in the plasma target and accelerated to high energies.

Although the data was only recorded at a reduced laser pulse energy of 1.76 J, similar trends are expected at higher laser pulse energies since the plasma density will enhance self-focusing and wakefield excitation in a similar way. The results further emphasise the stronger influence of the plasma density on the measured beam properties than the laser pulse energy. In fact, an increase of the pulse energy by $\sim 40\,\%$ caused an increase of the peak energy and the bunch charge of only $\sim 20\,\%$ and $\sim 60\,\%$, respectively.

7.3.2 Beam Divergence

Figure 7.7 shows that the vertical beam divergence x'_{rms} decreases, whereas the horizontal beam divergence y'_{rms} slightly increases at higher plasma densities.
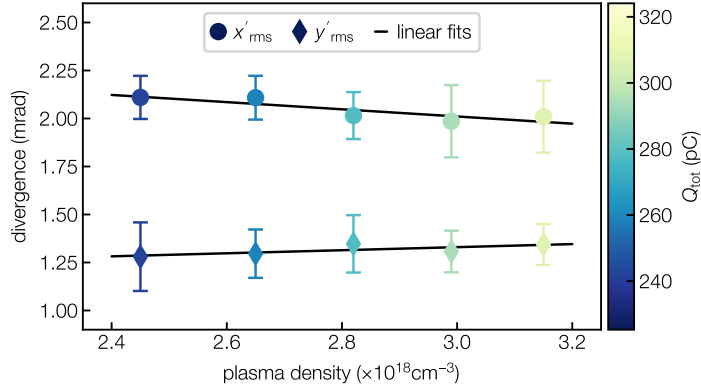
Figure 7.7 – Horizontal x'_{rms} (circles) and vertical y'_{rms} (diamonds) beam divergence as a function of the plasma density. The colormap shows the bunch charge measured with BPM1. Electron beams were generated at a laser pulse energy of 2.47 J and a nitrogen concentration of 1 %. Sample size for each setting is between 54 and 72. Linear fits are plotted to guide the eye.

The changes, however, are only $\sim 5\,\%$ and the beam divergence is nearly constant within the shot-to-shot fluctuations. The colormap shows that the bunch charge increases with the plasma density due to the formerly mentioned higher availability of nitrogen K-shell electrons and a larger transverse injection volume. No correlation between bunch charge and beam divergence can be observed. This is counterintuitive as a larger transverse injection volume causes off-peak electron which results in a larger betatron motion and hence increased beam divergence. Results in section 7.4.2 show that the bunch charge, either tuned with the nitrogen concentration or the laser pulse energy, directly correlates with the electron beam divergence. The reason that the plasma density increases the bunch charge but not the beam divergence is caused by the extraction section of the plasma target. PIC simulations presented in section 7.3.3 show that the beam divergence after acceleration is larger at higher plasma densities. In the plasma density ramp starting at $z \sim 6\,\mathrm{mm}$, the beam divergences are reduced to similar values.

7.3.3 PIC Simulations

The increase in bunch charge and peak energy with the plasma density can readily be explained with an increase of the acceleration field and the transverse injection volume. The effect of the plasma density on the beam divergence, however, is not as obvious on first glance.

Figure 7.8 shows the horizontal beam divergence x'_{rms} and beam size x_{rms} in the plasma density ramp at the exit of the plasma target for a range of similar plateau plasma densities than experimentally explored.
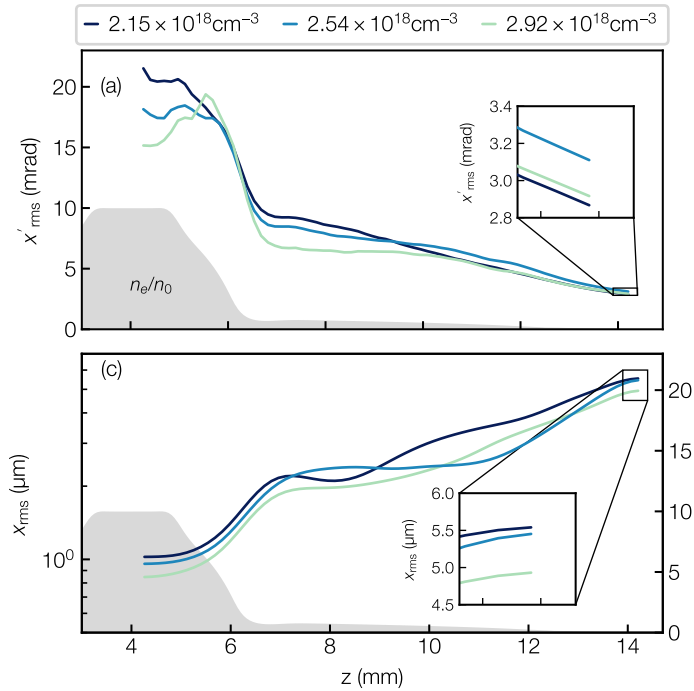
Figure 7.8 – PIC simulated horizontal x'_{rms} beam divergence (a) and rms beam size x_{rms} (c) for plasma densities between $2.15 \times 10^{18}\,\mathrm{cm}^{-3}$ and $2.92 \times 10^{18}\,\mathrm{cm}^{-3}$ in the plasma density ramp at the exit of the plasma target. The inset plots show the beam properties at the exit of the plasma target.

The beam size after acceleration, i.e. at $z \sim 4.3\,\mathrm{mm}$ is $\sim 6\%$ smaller at the highest simulated plasma density. This is due to stronger focusing forces of the wakefield, expected at a higher plasma density. The beam divergence is thus $\sim 30\%$ smaller at higher than at lower plasma density. The beam size increases in the plasma density ramp due to the gradually decreasing focusing forces. As a consequence, the beam divergence decreases. At the exit of the plasma target, shortly before the beam enters free drift, the difference in beam divergence is only $\sim 8\%$. Thus, the plasma density ramp counteracts the initial increase of the beam divergence with the plasma density. The horizontal beam size and beam divergence are not plotted but showed a similar trend.

In combination with the experimental results, we can draw the important conclusion from the PIC simulation results that the beam divergence is not significantly affected by the plasma density. This allows to tune bunch charge and peak energy independent of the beam divergence. This enables, for example, to operate at reduced laser pulse energies ensuring smaller beam divergence, as was shown in section 7.4.2 and to mitigating the reduced bunch charge and energy by increasing the plasma density.

7.4 Influence of the Nitrogen Concentration

Laser focus position, pulse energy and plasma density allow to tune bunch charge and peak energy in a wide range but not for independent control of the electron beam parameters or to specifically enhance electron beam quality. The data further revealed that the accelerator is operated in a beam loaded regime for the chosen laser-plasma parameters. Beam loading is typically associated with limiting the bunch charge and reducing electron energy gain due to the modulation of the laser wakefield by the self-field of the bunch [119]. However, beam loading also decisively determines electron phase-space characteristics and hence electron beam quality. In order to utilize beam loading to enhance electron beam quality it is necessary to precisely control the amount of injected charge.

The injected charge in the ionization injection scheme correlates with the availability of the inner shell electrons of the high Z-gas and thus its concentration. Several experimental results have shown that this allows to directly tune the bunch charge [6, 49, 120]. This was utilized in recent work to achieve optimum loading of the wakefield and to generate electron beams with a comparable small energy spread for ionization injected electron beams of 15 %, combined with 0.5 nC bunch charge [6]. PIC simulation further revealed that the concentration of the high Z-gas determines electron phase-space rotation [113]. This allows to enhance electron beam quality even if an optimum loading of the wakefield is not achieved. Eq. 2.31 shows that beam loading additionally depends on the laser power and that a stronger driven wakefield can sustain more charge. To control beam loading effects and electron phase-space rotation, it is thus necessary to match the amount of injected charge to the laser power.

This section shows how to tune bunch charge and and to control beam loading effects in the ionization injection scheme with a combination of the nitrogen concentration and the laser pulse energy. The influence on the energy spectrum and the bunch charge is presented in section 7.4.1, followed by the influence on the beam divergence in section 7.4.2. Experimental results are supported with PIC simulations in section 7.4.3.

To study beam loading effects independent of laser self-modulation and wakefield excitation, it is important to keep the background plasma density constant while varying the nitrogen concentration. This is achieved by regulating the pressure in the capillary according to eq. 4.7. The plasma density in the dataset presented in the following was $2.52 \times 10^{18}\,\mathrm{cm}^{-3}$ with a stability of $\pm\,5\,\%$ for all explored nitrogen concentrations between 0.1 % and 5 %. Thus, changes in electron beam parameters at constant laser pulse energy can directly be related to the availability of the nitrogen K-shell electrons in the background plasma.

7.4.1 Energy Spectrum and Bunch Charge

Figure 7.9 shows the projected energy spectra and the total bunch charge Q_{tot} as a function of the nitrogen concentration C_{N_2} for the previously explored laser pulse energies between 1.76 J and 2.83 J.

Peak Energy and Bunch Charge
The bunch charge is directly correlated with the nitrogen concentration, confirming that the accelerated electrons in fact originate from ionization of the nitrogen K-shell. The bunch charge is first maximized with the nitrogen concentration before decreasing again at higher concentrations for the three larger laser pulse energies, see figures 7.9a to 7.9c. No decrease is observed for the lowest explored laser pulse energy of 1.7 J, see figure 7.9d. The decrease indicates that the wakefield is fully loaded and that trapping is inefficient due to beam loading. The highest measured bunch charges and the beam loading limited charge, predicted from eq. 2.31, are compared in table 7.1. The bunch charges agree within $\sim 20\,\%$ for laser pulse energies of 2.11 J, 2.47 J and 2.83 J. For a laser pulse energy of 1.76 J, it is predicted that the wakefield can sustain up to 40 % more charge, explaining why no decrease of the bunch charge was observed in the experiment. A higher nitrogen concentration than 5 % would thus be necessary to reach the beam loading limit at this laser pulse energy.

Beam loading manifest itself in a reduced energy gain due to modulation of the longitudinal accelerating field E_z. This trend is clearly observed in the data with decreasing peak energies for increasing nitrogen concentrations. In fact, the highest peak energy is achieved at the lowest explored nitrogen concentration of 0.1 % and hence lowest bunch charge at constant laser pulse energy. This clearly emphasises the trade-off between bunch charge and energy gain when operating in a beam loaded regime.

Table 7.1 – Highest measured bunch charge Q_{exp} compared to theoretical maximum bunch charge Q_{theo} calculated with eq. 2.31.

E_l (J)	C_{N_2} (%)	Q_{exp} (pC)	Q_{theo} (pC)
2.83	2	326 ± 10	350
2.47	3	283 ± 10	327
2.11	3	236 ± 12	302
1.76	5	163 ± 15	276
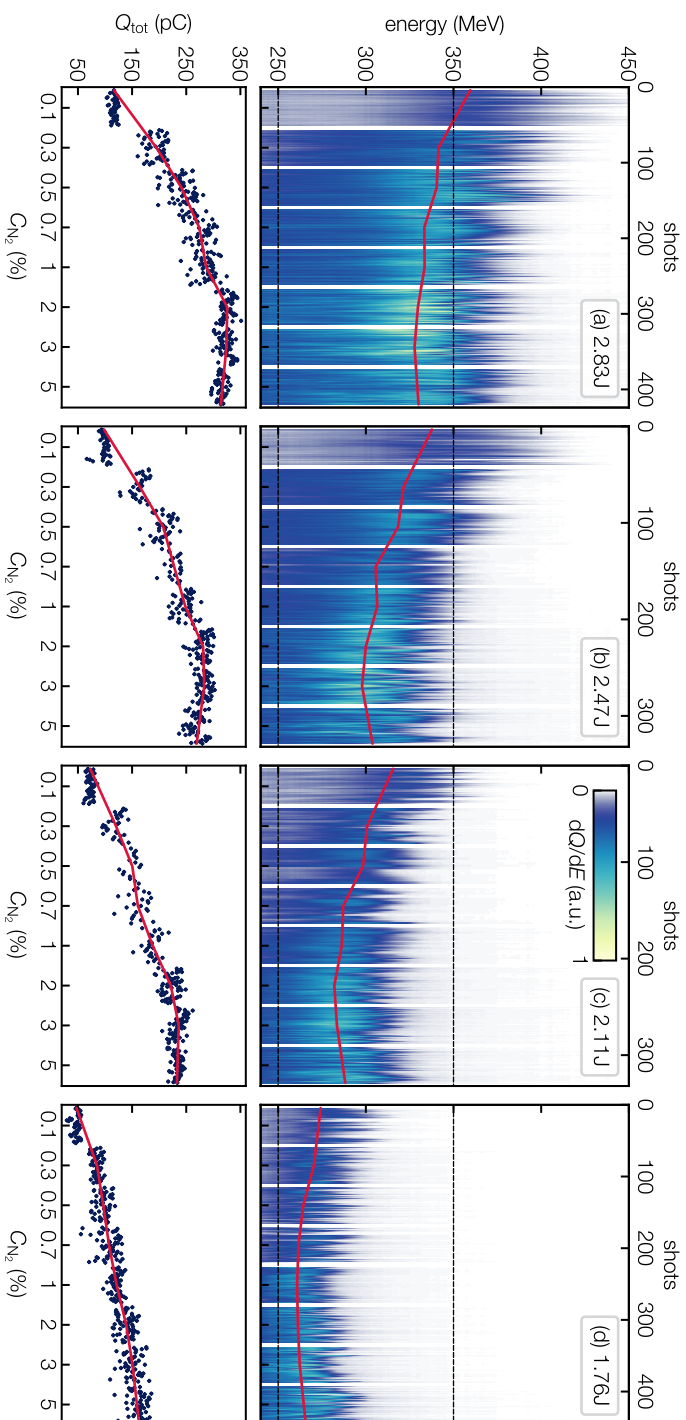
**Figure 7.9** – Series of projected energy spectra (top row) and bunch charge (bottom row) as a function of the nitrogen concentration C_{N_2}. Energy spectra and crosses show single shot data and the red lines connect the mean values of each set point. Each column (a–d) corresponds to a specific laser pulse from 2.83 J down to 1.76 J. Number of electron beam data points for each setting is between 16 and 64.

From the dataset it is further deduced that the laser pulse energy influences bunch charge and peak energy more strongly than the nitrogen concentration. A relative increasing of laser pulse energy by 40 % at a nitrogen concentration of 1 % increases the bunch charge by 40 % and the peak energy by 20 %. A relative increase of the nitrogen concentration by 100 %, on the other hand, increases the bunch charge by only 60 % while the peak energy is reduced by 10 %. Thus, it is preferred to operate with high laser pulse energies to first increase the bunch charge and then use the nitrogen concentration for fine tuning. This is further of interest as higher nitrogen concentrations can cause ionization induced de-focusing which decreases the laser intensity and hence energy gain further [45].

Energy Spread and Peak Charge Density
The effect of the nitrogen concentration on the relative energy spread $\Delta E/E_{\mathrm{peak}}$ and the peak charge density $\mathrm{d}Q/\mathrm{d}E_{\mathrm{peak}}$ is shown in figure 7.10.

When the accelerator is operated in a strongly loaded regime, i.e. for the three larger laser pulse energies, the energy spread is smallest and the peak charge density highest at the same nitrogen concentrations maximizing the bunch charge, see figures 7.10a to 7.10c. This implies that the phase-space of high-energy electrons, located at the head of the bunch, over-rotates and becomes more symmetric in case of fully loaded wakefield. This reduces the slice energy spread of the high-energy peak. In agreement with previous results, this shows that the nitrogen concentrations determines the degree of phase-space rotation [113]. The beam loading limit was not reached for the lowest explored laser pulse energy of 1.76 J, as was shown in table 7.1. Thus, the relative energy spread and the peak charge density continuously increase with the nitrogen concentration, see figure 7.10d.

Although the nitrogen concentration allows to fine tune electron beam quality, the lowest achievable energy spread is still limited by continuous electron injection when operating in a strongly loaded regime. A large amount of charge is initially injected and keeps being injected as the laser is intense enough to ionize the nitrogen K-shell electrons for a comparably large distance in the plasma target. The wakefield is strongly modulated and the acceleration fields vary along the bunch length. Head and tail of the bunch are not separated and the energy spread increases as a result. The influence of the nitrogen concentration on the longitudinal electron phase-space is further discussed with PIC simulations in section 7.4.3.

The lowest relative energy spread of (13 ± 2.4) % was recorded at lowest laser pulse energy and nitrogen concentration of 1.76 J and of 0.1 %, respectively. The vacuum laser intensity of $a_0 \sim 1.6$ is below the appearance intensity of the first nitrogen K-shell electron (N^{6+}) of $a_0 \sim 2.2$. The laser thus has to propagate a larger distance to self-focus and to become intense enough for ionization and trapping. Electrons are therefore injected over a shorter distance in the plasma target. Accelerating fields are still present when injection stops, separating the head and tail of the bunch and thus reducing the energy spread. PIC
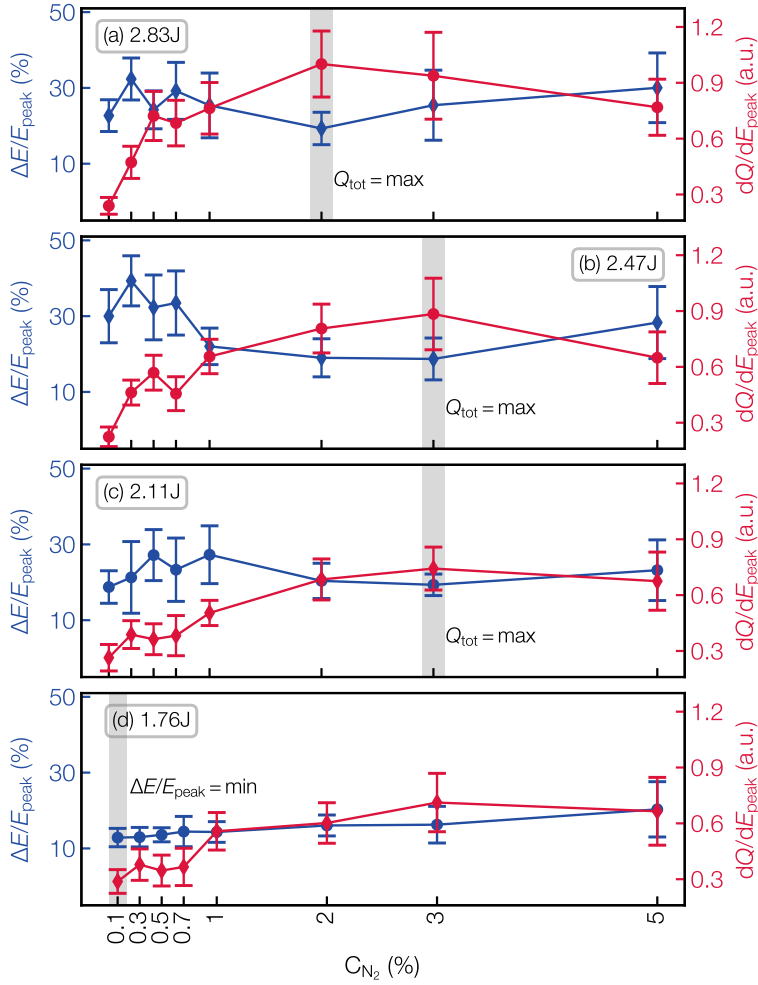
Figure 7.10 – Relative energy spread $\Delta E/E_{peak}$ (blue line) and peak charge density dQ/dE_{peak} (red line) as a function of the nitrogen concentration C_{N_2} for various laser pulse energies (a-d). Gray shaded areas indicate the nitrogen concentrations maximizing the bunch charge (a-c) and lowest recoded energy spread (d). Number of electron beam data points for each setting is between 16 and 64.

simulation results presented by C. Kamperidis et al. confirm this assumption [121]. It was found that narrow energy spread beams can be generated with ionization injection when the laser intensity is closely matched to the appearance intensity of the inner shell electrons of the high-Z gas.

Table 7.2 summarizes the optimized electron beam parameters. For the operation of the accelerator we can draw the following conclusions from the presented results: Electron beams with reduced energy spread can be generated with low laser intensities and nitrogen concentrations but at the expense of bunch charge, peak energy and charge density.

These properties can be increased significantly when operating with higher laser intensities and nitrogen concentrations but with an increased energy spread. In this strongly loaded regime, energy spread and peak charge density can be enhanced simultaneously with the nitrogen concentration.

7.4.2 Beam Divergence

The influence of the nitrogen concentration and the laser pulse energy on the beam divergence was measured with the first electron screen station ESS1 and corrected with the calibration factor of 2.3 to account for the limited charge sensitivity of the screen station, see section 3.5. The same parameter space as for the measurement on the electron spectrometer was explored. The energy spectrum was not recorded simultaneously since the electron beams are scattered when passing through the scintillation screen. In contrast to the dataset acquired on the electron spectrometer, 200 consecutive shots for each setting were taken.

Figure 7.11 shows the horizontal x'_{rms} and vertical y'_{rms} beam divergence as a function of the nitrogen concentration for the range of previously explored laser pulse energies between 1.76 J and 2.83 J.

Here, x'_{rms} corresponds to the laser polarization direction. The beam divergence in both planes increases with the laser pulse energy at constant nitrogen concentration. This trend is commonly observed for ionization injected electron beams and can be explained two-fold [31, 122]. First, the transverse injection volume increases with the pulse energy. Electrons are ionized off-peak i.e. where $a(\xi_{\mathrm{ion}}) \neq 0$ and gain momentum in the laser polarization direction. Second, a higher pulse energy causes off-axis ionization with respect to the laser propagation direction. Electrons experience a larger ponderomotive force in both, the laser polarization and its orthogonal direction, thus increasing the beam divergence in both planes [123].

A first strong increase of the beam divergence in laser polarization direction with the nitrogen concentration is observed. The increase follows the same trends as the bunch charge, see figure 7.9. In fact, the beam divergences are largest at the same nitrogen concentrations maximizing the bunch charge, see table 7.2. The increase therefore seems to be related to the bunch charge, although the intrinsic momentum gained during ionization should, in principle, not dependent on the amount of trapped electrons. The vertical beam divergence shows a much weaker correlation with the nitrogen concentration. Here, the beam divergence is nearly constant for the two lower explored laser pulse energies of 1.76 J and 2.11 J. For laser pulse energies of 2.47 J and 2.83 J, on the other hand, there is also a first increase with the nitrogen concentration up to 0.3 % and 0.5 % and a decrease afterwards observed.
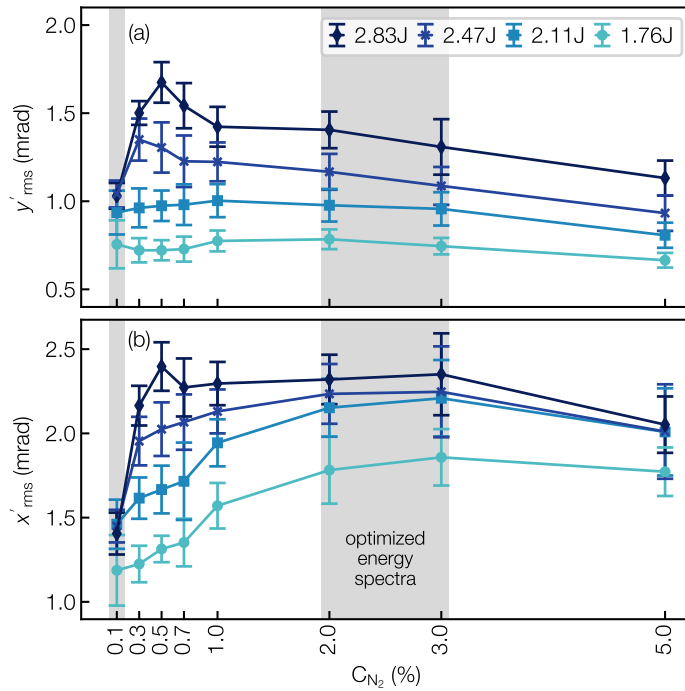
Figure 7.11 – Horizontal x'_{rms} (a) and vertical y'_{rms} beam divergence (b) as a function of the nitrogen concentration C_{N_2}. Each solid line connects mean data points taken at a constant laser pulse energy between 1.76 and 2.83 J. Number of electron beam data points for each setting is between 15 and 146.

An increase of the beam divergence with the nitrogen concentration for comparable laser-plasma parameters was also observed by Gonzalez et al. in [120]. It was found that the increase is caused by a combination of beam loading and direct laser acceleration. In a similar way than in the results presented within this thesis, the peak charge density of the generated electron beams in their experiments increased with the nitrogen concentration. Thus, a larger amount of electrons is located at the head of the bunch and is overlapping with the laser field. These electrons are subject to direct laser acceleration which results in an increased betatron motion of the electrons and hence in a larger beam divergence. Direct laser acceleration (DLA) can be identified by a forked distribution of high-energy electrons in the non-dispersive plane of the electron spectrometer. Such a structure was not present in our measurements. However, these structures were observed by Gonzalez et al. at positions corresponding to a beam divergence of ± 6 mrad [120]. As the LUX electron spectrometer does not cover such a wide range, it can not be completely excluded that such structures were present in the energy spectra. Thus, DLA could be a reason for the increase of the beam divergence with the nitrogen concentration.

However, it is more likely that the increase is caused by beam loading effects. The focusing forces vary across the bunch length depending on the nitrogen concentration as the

modulation of the wakefield depends on the charge density of the electron bunch. Thus, different energy parts of the beam can have a different beam divergence. This effect is illustrated with PIC simulations in figure 5.4. In this particular simulation, the beam divergence decreases with the energy of the electrons as they experience weaker focusing forces during acceleration. The laser wakefield becomes more strongly modulated with increasing charge density and hence nitrogen concentration. It is thus expected that the focusing forces at the tail of the bunch also decrease with the nitrogen concentration and that the beam divergence of the low-energy electrons therefore increases. The energy integrated beam divergence, measured with the electron screen station, therefore increases. To further investigate this effect it is necessary to measure the beam divergence energy resolved. This can be done with the single shot reconstruction technique introduced in section 3.4.4.

The gray shaded areas in figure 7.11 depict the nitrogen concentrations optimizing the energy spectra, as was shown in figure 7.10. The electron beam parameters in these laser-plasma configurations are listed in table 7.2.

Similar to the observations for the energy spread, the smallest horizontal and vertical beam divergence of $x'_{\mathrm{rms}} = (1.2 \pm 0.2)\,\mathrm{mrad}$ and $y'_{\mathrm{rms}} = (0.8 \pm 0.1)\,\mathrm{mrad}$ was recorded at the lowest explored nitrogen concentration of $0.1\,\%$ and laser pulse energy of $1.76\,\mathrm{J}$. This leads to the important conclusion that in order to generate electron beams with sub-millirad beam divergence, required to drive applications such as a FEL, it would be necessary to even further reduce the nitrogen concentration and the laser pulse energy. However, this comes at the expense of beam energy and bunch charge, clearly showing that the limiting factor in the designed plasma target is the momentum gained by the electrons being born inside the laser field. The measured beam divergences from $0.8\,\mathrm{mrad}$ to $2.4\,\mathrm{mrad}$ for nitrogen concentrations between $1\,\%$ and $3\,\%$, the typical operation range of the LUX accelerator, however, are already sufficiently low for the transport with electron beam optics. As elaborated with PIC simulations in section 5.3, the comparably small beam divergence for ionization injected electron beams is due the adiabatic extraction section of the plasma target. Electron beams with similar parameters were successfully focused into the BEAST2 undulator to generate X-Ray radiation with wavelength of $6\,\mathrm{nm}$ to $8\,\mathrm{nm}$ [60]. In this parameter range, the pulse energy seems to have a larger effect on the beam divergence than the nitrogen concentration. This allows to fine-tune the transverse beam emittance with the laser pulse energy. Experimental results are presented in section 7.5.

Table 7.2 – Optimized electron beam parameters depending on the laser pulse energy and the nitrogen concentration.

E_l (J)	C_{N_2} (%)	Q_{tot} (pC)	E_{peak} (MeV)	$\Delta E/E_{\mathrm{peak}}$ (%)	dQ/dE_{peak} (a.u.)	x'_{rms} (mrad)	y'_{rms} (mrad)
2.83	2	326 ± 10	330 ± 10	20 ± 4	$1 \pm 0.17 \times 10^4$	2.4 ± 0.1	1.4 ± 0.1
2.47	3	283 ± 10	298 ± 11	19 ± 6	$0.88 \pm 0.19 \times 10^4$	2.3 ± 0.1	1.1 ± 0.1
2.11	3	236 ± 12	288 ± 6	19 ± 3	$0.74 \pm 0.12 \times 10^4$	2.2 ± 0.2	1 ± 0.1
1.76	0.1	47 ± 6	274 ± 9	13 ± 2.4	$0.67 \pm 0.18 \times 10^4$	1.2 ± 0.2	0.8 ± 0.1

Table 7.3 – PIC simulated parameters of electron beams generated at nitrogen concentrations of 0.1 %, 1 % and 5 %. The corresponding longitudinal electron phase-space and energy spectra are shown in figure 7.13.

E_l (J)	C_{N_2} (%)	Q_{tot} (pC)	E_{peak}	dQ/dE_{peak} (pC/MeV)	x'_{rms} (mrad)	y'_{rms} (mrad)	$\varepsilon_{\mathrm{n,x}}$ (mm mrad)
1.7	0.1	79	390	0.41	2.53	1.7	4.6
1.7	1	148	319	0.72	3.11	1.66	5.1
1.7	5	125	304	0.55	2.89	1.68	4.1

7.4.3 PIC Simulations

PIC simulations with various nitrogen concentrations but otherwise identical parameters as listed in table 5.1 were performed to support the experimental findings. Simulation results are compared to data recorded at a laser pulse energy of 2.47 J in figure 7.12. The experimental observed trends of the peak energy and the bunch charge are well reproduced in the simulations, although the measured bunch charges are not reached. The simulations confirm that the bunch charge can be increased with the nitrogen concentration as well as the resulting decrease of the peak energy.
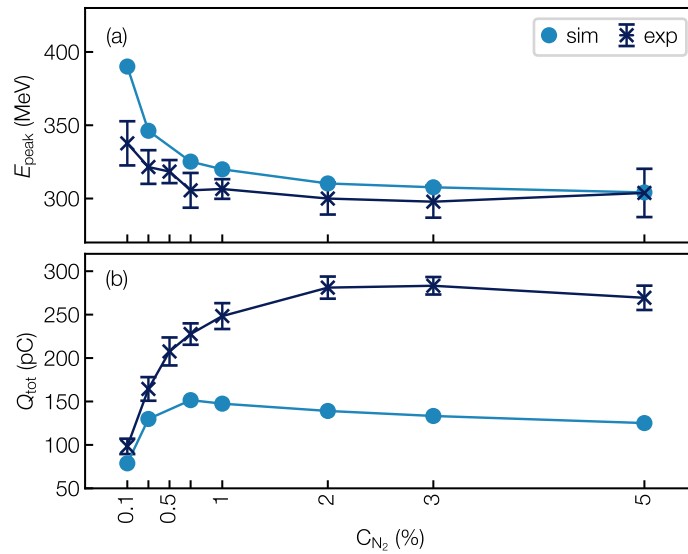

Figure 7.12 – Comparison between experimental (crosses) and simulated (dots) peak energy (a) and bunch charge (b) as a function of the nitrogen concentration C_{N_2}.

To confirm the operation in a beam loaded regime, the average longitudinal accelerating field E_z along the laser-plasma interaction is exemplary shown for nitrogen concentrations of $0.3\,\%$, $1\,\%$ and $5\,\%$ in figure 7.13a. The reduced amplitude for increasing nitrogen concentration due to a stronger modulation of the laser wakefield by the self flied of the electron bunch is clearly visible. This reinforces the experimentally observed trade-off between bunch charge and beam energy. The simulations did not reveal changes in laser self-focusing or self-compression for the different nitrogen concentrations. Effects such as ionization induced de-focusing which would also decrease the accelerating field, can therefore be excluded.

The longitudinal electron phase-spaces and the projected energy spectra at the exit of the plasma target are shown in figures 7.13b to 7.13d. The beam parameters are listed in 7.13. The spectra exhibit the characteristic features of the generated electron beams, i.e.
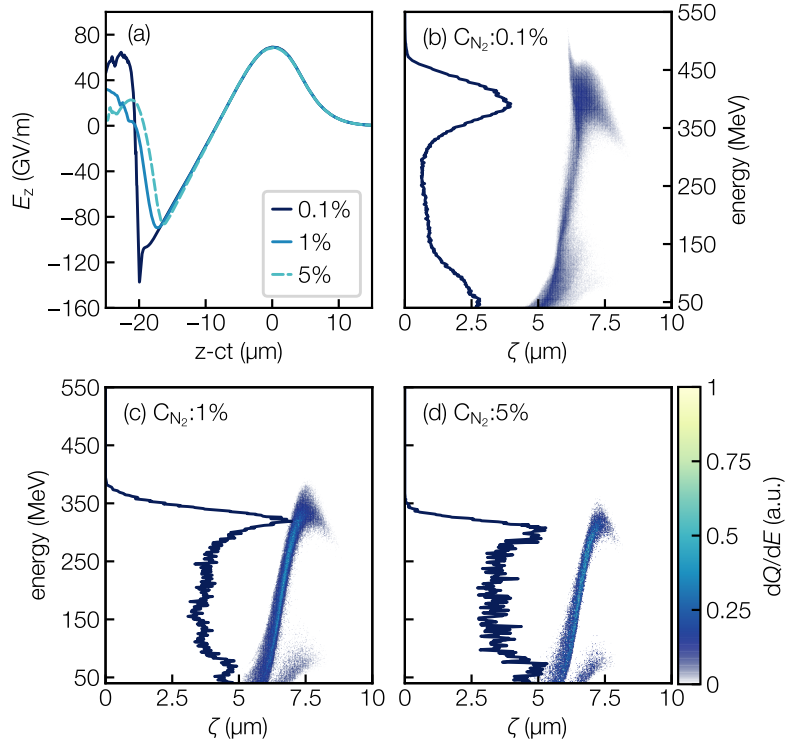
Figure 7.13 – PIC simulated average accelerating field E_z along the laser-plasma interaction length for nitrogen concentrations of 0.3 %, 1 % and 5 % (a). Corresponding longitudinal electron phase-space distribution at the exit of the plasma target (b-d) and projected energy spectra (dark blue lines). The colormap shows the charge density. The simulations were performed with a laser pulse energy of 1.7 J and a plasma density of $2.54 \times 10^{18}\,\mathrm{cm}^{-3}$. Figure (a) is shown in the co-moving frame of the laser pulse. Figures (b-d) are shown as function of relative bunch coordinate ζ. The simulated electron beam parameters are additionally listed in table 7.2.

the high-energy peak and the low-energy tail due to continuous electron injection. In this particular simulation, the high-energy peak is optimized with a nitrogen concentration of 1 % as the phase-space of the high-energy electrons slightly over-rotates and becomes more symmetric than for nitrogen concentrations of 0.1 % and 5 %. The peak charge density of the simulated electron beams is between 0.41 pC/MeV and 0.71 pC/MeV. This gives the order of magnitude for the experimentally electron beams where the peak charge density can only be given as relative measure.

The optimized energy spectrum in the experiment, for a comparable laser pulse energy, was achieved with a nitrogen concentration of 2 %. As beam loading and thus the final electron beam parameters are very sensitive to the laser-plasma configuration, the difference is most likely caused by non-perfectly matching of experimental and simulation parameters. However, PIC simulations confirm the operation in a beam loaded

regime and the optimization potential of electron beam parameters with the nitrogen concentration.

7.5 Emittance Optimization

The previously presented beam divergence measurements on the electron screen station showed a strong increase of the horizontal and vertical beam divergence with the laser pulse energy. From the correlation between beam divergence and beam emittance, i.e. $\epsilon_{n,x} \propto \sqrt{\langle x'^2 \rangle}$ (eq. 3.3), it is expected that the beam emittance increases in a similar way. It was thus a focus to enhance the beam emittance by fine-tuning the laser pulse energy while keeping other parameters constant, i.e. the plasma density at $n_e = 2.44 \times 10^{18}\,\mathrm{cm}^{-3}$ and the nitrogen concentration at $1\,\%$. The beam emittance is reconstructed with the single-shot technique introduced in section 3.4.4.

Electron Beam Parameters
Beam divergence and beam emittance are reconstructed by focusing the electron beams onto the spectrometer screen. Figure 7.14a shows the average transmitted energy spectrum of unfocused and focused electron beams both generated with the same laser-plasma configuration.
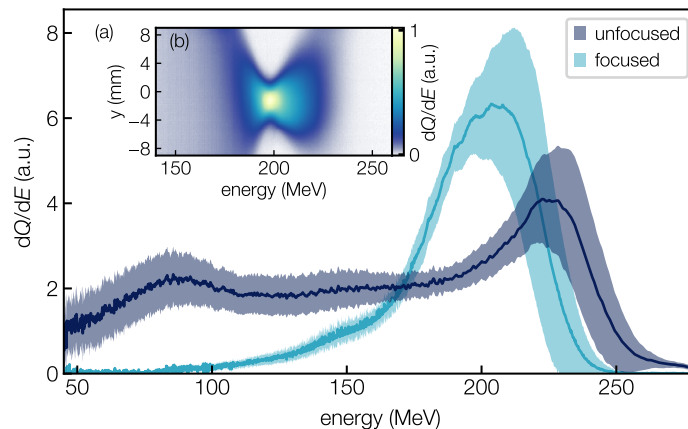
Figure 7.14 – Transmitted energy spectrum of un-focused (dark blue) and focused (light blue) electron beams generated with the same lase-plasma configuration (a). The spectra show the average of 100 consecutive shots. The shaded areas denote the 1 STD shot-to-shot variations. 2D intensity profile of the focused beam on the spectrometer screen (b). The quadrupole doublet was set to focus a beam energy of 200 MeV.

The corresponding 2D intensity profile on the spectrometer screen is depicted in figure 7.14b. The quadrupole doublet was set to image a beam energy of 200 MeV. Focusing the beams reduces the charge density of the low-energy tail and crops energies below $\sim 90\,\mathrm{MeV}$ due to the chromaticity of the quadrupole doublet. The charge density at the

focused energy is increased since the beamline transmission of the unfocused beams is lower due to beam divergence and the finite spectrometer screen width. The transmitted bunch charge is reduced from $(89 \pm 9)\,\mathrm{pC}$ measured for the unfocused beams with BPM1 to $(27 \pm 6)\,\mathrm{pC}$ measured for the focused beams with BPM2, directly in front of the electron spectrometer.

Reconstruction Results

Figure 7.15 shows the horizontal beam divergence x'_{rms} and normalized beam emittance $\epsilon_{\mathrm{n,x}}$ in an energy interval between $196\,\mathrm{MeV}$ and $204\,\mathrm{MeV}$ as a function of the laser pulse energy. The reconstructed plane corresponds to the laser polarization direction. Beam divergence and beam emittance show a linear increase with the laser pulse energy. The increase is caused by off-peak and off-axis ionization of electrons, associated with higher laser intensities and larger transverse injection volume. The larger transverse injection volume is also seen in the increase of the bunch charge, see secondary x-axis.
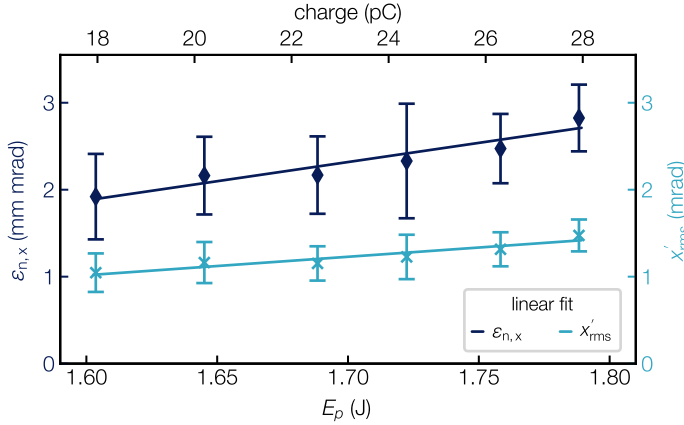
Figure 7.15 – Horizontal rms beam emittance $\varepsilon_{\mathrm{n,x}}$ (diamonds) and beam divergence x'_{rms} (crosses) as a function of the laser pulse energy E_p. The secondary x axis shows the total bunch charge measured with BPM2. Sample size at each setting is between 53 and 63. Linear fits are plotted to guide the eye.

An analytical correlation between laser pulse energy and beam emittance in the ionization injection scheme was given by C. Schroeder et al. [123]. After ionization of the electrons and passing through the laser field, the initial transverse beam emittance in the laser polarization direction can be approximated by

$$\epsilon_{n,x} \simeq \left(\frac{3\pi r_e}{\sqrt{2}\alpha^4} \right) \left(\frac{U_{\mathrm{H}}}{U_i} \right)^{3/2} \frac{\omega_i a_i^2}{\lambda_i}, \tag{7.1}$$

with r_e being the classical electron radius, $\alpha = e^2/\hbar c$ the fine structure constant, a_i, ω_i and λ_i the normalized laser parameters. $U_{\mathrm{H}} = 13.6\,\mathrm{eV}$ and U_{i} are the ionization potential of hydrogen and the inner shell electron of the high-Z dopant, respectively. Eq. 7.1 shows that the laser field a_i has the strongest influence on the beam emittance, i.e. $\epsilon_{\mathrm{n,x}} \propto a_i^2$. In order to reduce the beam emittance, it is thus preferred to operate with low laser pulse energies. However, ionization injection is only possible in the non-linear regime of laser-plasma acceleration, requiring $a_0 \gg 1$, see section 2.3.2. This sets an intrinsic limit to the smallest achievable beam emittance.

The experimental results are on the order of magnitude of previously reported results for ionization injected beams but due to the interaction with the laser field larger than reported for beams generated with other injection techniques [8, 124].

It is noted that the presented correlations can not be understood as an absolute measure over the whole energy spectrum and are only valid for the narrow energy range of $\pm\,4\,\%$ around the focused beam energy of $200\,\mathrm{MeV}$. PIC simulations in section 5.4 show that the electron phase-space parameters are not constant along the bunch length and that the beam divergence and the beam emittance decrease towards higher energies. Measurements performed by P. Winkler at LUX, for electron beams generated with ionization injected in the same plasma target designed within this thesis, confirm these findings [79]. Further experimental investigation is necessary, to reconstruct the beam emittance and beam divergence, in several steps over the full energy spectrum for different laser pulse energies, to get the full picture.

8 Conclusion and Outlook

This thesis has reported on the experimental study of ionization injection in a single stage plasma target aimed towards controlled and stable laser-plasma acceleration. In contrast to previous results, it was not focused on improving the typically large energy spread of ionization injected electron beams [36, 38–41], but rather on extensive control of electron beam parameters. A broad parametric study with high statistical relevance was conducted at the LUX beamline to investigate the effect of the laser-plasma configuration on the electron beam parameters and quality. The presented results and the identified scalings allow the reproducible and stable operation of a laser-plasma accelerator in a wide range and are an important step towards providing electron beams suitable as drivers for many applications.

Electron beam generation with ionization injection was studied in a nitrogen doped hydrogen plasma, provided in a capillary type plasma target. The plasma target was developed and characterized with 3D CFD simulations. A decisive characteristic of the plasma target is the reduction of the beam divergence after acceleration in a density ramp at its axis. Depending on the laser-plasma configuration, a vertical beam divergence between 0.8 ± 0.1 mrad and 1.4 ± 0.1 mrad and a horizontal beam divergence between 1.2 ± 0.2 mrad and 2.4 ± 0.1 mrad were observed. Recent results for ionization injected electron beams showed a noticeably larger beam divergence between 4 mrad and 7 mrad [6, 37, 41, 120]. Although it was found that the electron screen station used for the measurement of the beam divergence within this thesis is limited in charge resolutions, the achieved, comparable small, beam divergence could be confirmed with a second independent measurement technique and could further be reproduced with PIC simulations.

Amongst the applications requiring a small beam divergence are complex laser-plasma driven beamlines which are inevitably equipped with electron beam optics [9, 15]. Beam optical elements with large apertures and strong magnetic fields are necessary to capture electron beams with a large beam divergence. Thus, the designed plasma target with the density ramp at its exit lowers the strong demands imposed on the electron beam optics in terms of beam divergence and can reduce the cost and complexity of such a beamline.

The robust plasma target design, the operation at continuous gas flow and the implementation of direct pressure diagnostic enabled to precisely tune electron beam parameters

with several plasma properties and laser parameters. The identified scalings allow to operate a laser-plasma accelerator in different regimes, depending on the demands of the application.

The most direct ways to tune bunch charge and peak energy of the generated electron beams at constant plasma properties were found to be the laser pulse energy and the laser focus position in the target. While varying the laser pulse energy implies a to some extend powerful laser system, translating the plasma target to change the focus position is more straight forward. On the downside, these parameters also increased the energy spread of the electron beams, especially the laser pulse energy. However, some applications might still benefit from readily tunable bunch charge and peak energy, for example a Thomson scattering X-ray source [125]. The wavelength of the radiation depends on the energy and the number of generated photons on the bunch charge of the electron beams. To mitigate an increasing energy spread which broadens the X-ray spectrum, an active plasma lens could be implemented to filter out certain electron energies [126]. Thus, the presented target could drive a very compact, tunable and robust X-ray source.

When considering to generate X-rays with an undulator, typically the case of state-of-the-art research facilities, with laser-plasma accelerated electrons, it is not sufficiently enough to only increase the bunch charge or the peak energy, but moreover to optimize the energy spectrum in a certain bandwidth. Enhancing the electron beam quality in terms of energy spread and peak charge density was demonstrated within this thesis by balancing the amount of injected charge and the strength of the laser driven wakefield. By precisely adjusting the nitrogen concentration, determining the amount of injected charge online while collectively varying the laser pulse energy, it was possible to increase the number of electrons in the characteristic high-energy peak of the energy spectrum and to simultaneously decrease the energy spread. PIC simulations revealed that the nitrogen concentration is effective to determine electron phase-space rotation and the optimized energy spectra are due to beam loading effects. Although previous results have shown such tuning of the energy spread with the nitrogen concentration [6], the combined effect with the laser pulse energy was not yet shown.

To reach these optimum conditions and the beam loading limit, comparable high laser pulse energies are required. It was identified that the interaction of the electrons with the laser field during ionization results in an increase of the beam divergence with the laser pulse energy. An optimized energy spectrum therefore comes, to some extend, with the expense of a small beam divergence in the explored parameter space. However, the beam divergences achieved with the presented plasma target are still sufficiently low for the transport with electron beam optics. Electron beams with a mean peak energy of $(314 \pm 20)\,\text{MeV}$ and a bunch charge of $(87 \pm 9)\,\text{pC}$ were focused with the high-gradient quadrupole doublet into the BEAST2 undulator [127] to generate spontaneous undulator radiation at 1 Hz repetition rate. Figure 8.1 shows a waterfall plot of X-ray spectra with first order diffractions at $\sim 8.2\,\text{nm}$. From the 1020 consecutively recorded shots, 920
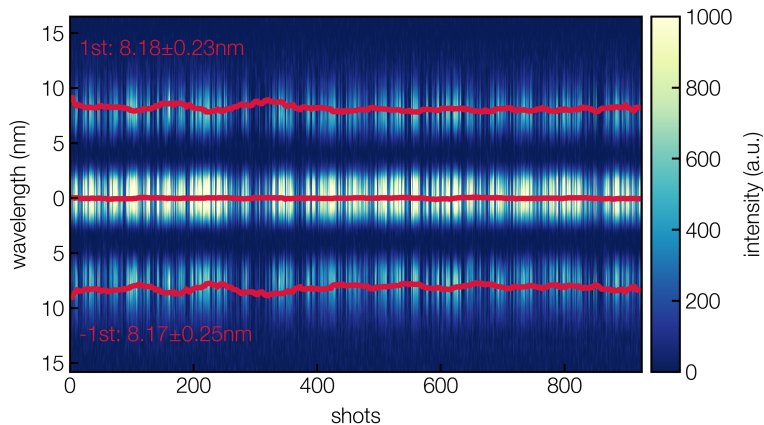
Figure 8.1 – Spontaneous undulator radiation with first order diffractions at $\sim 8.2\,\mathrm{nm}$ generated with the presented plasma target and the BEAST2 undulator (undulator period of $5\,\mathrm{mm}$ and K parameter of ~ 0.27) at LUX. Electron beam parameters: peak energy $(314 \pm 20)\,\mathrm{MeV}$, total bunch charge $(87 \pm 9)\,\mathrm{pC}$. 920 of the 1020 recorded shots show X-ray signal. The red lines show the rolling average over 50 consecutive shots. Data and analysis in courtesy of C. Werle [60].

showed X-ray signal, which correspond to an availability of $\sim 90\,\%$. The setup is not limited to a single X-ray wavelength as the wavelength depends on the energy of the electron beams. A widely used application in scientific disciplines for such a tunable, compact soft X-ray source would be X-ray spectromicroscopy [128].

An increasing number of research fields requires even brighter light sources such as Free-Electron-Lasers (FEL) for high-resolution diffraction and spectroscopic imaging. Only a few FEL facilities exist worldwide due to their immense size and cost. Driving a FEL with laser-plasma accelerated electrons could reduce the size and cost significantly and hence increase their availability.

The LUX beamline is currently being upgraded to demonstrate FEL gain. The major challenge is to achieve the design electron beam parameters: An energy spread of $\sim 1\,\%$, a beam divergence of $\sim 1\,\mathrm{mrad}$ and a beam emittance of $\sim 1\,\mathrm{mm\,mrad}$ at peak energies between $200\,\mathrm{MeV}$ and $300\,\mathrm{MeV}$. The ongoing research at LUX, to generate electron beams with such a high quality, is directed towards the development of novel plasma targets. Due to robust electron injection and direct control of the bunch charge, those plasma target will be operated with ionization injection. The main design aspect is to reduce the longitudinal injection distance, as was identified within this thesis to be the predominantly reason for a broad energy spectrum. This implies that the mixed gas section has to be localized within the plasma target. Simultaneously it has to be ensured that this does not come with the expense of acceleration distance and hence beam energy. The small beam divergences and beam emittances could be achieved two-fold. First, by operating with comparably low laser pulse energies to reduce these parameters during

injection. Second, by including a density ramp at the exit of the plasma target, acting as an adiabatic extraction section, to further decrease beam divergence and beam emittance after acceleration. The operation regime and the exact dimensions of the novel plasma target are currently being derived from PIC simulations taking the identified scalings, with the parametric study performed within this thesis, into account.

Bibliography

[1] T. Tajima and J. M. Dawson. Laser electron accelerator. *Phys. Rev. Lett.*, 43:267–270, Jul 1979.

[2] W. P. Leemans, B. Nagler, A. J. Gonsalves, Cs. Tóth, K. Nakamura, C. G. R. Geddes, E. Esarey, C. B. Schroeder, and S. M. Hooker. Gev electron beams from a centimetre-scale accelerator. *Nature Physics*, 2(10):696–699, 2006.

[3] W. P. Leemans, A. J. Gonsalves, H.-S. Mao, K. Nakamura, C. Benedetti, C. B. Schroeder, Cs. Tóth, J. Daniels, D. E. Mittelberger, S. S. Bulanov, J.-L. Vay, C. G. R. Geddes, and E. Esarey. Multi-gev electron beams from capillary-discharge-guided subpetawatt laser pulses in the self-trapping regime. *Phys. Rev. Lett.*, 113:245002, Dec 2014.

[4] A. J. Gonsalves, K. Nakamura, J. Daniels, C. Benedetti, C. Pieronek, T. C. H. de Raadt, S. Steinke, J. H. Bin, S. S. Bulanov, J. van Tilborg, C. G. R. Geddes, C. B. Schroeder, Cs. Tóth, E. Esarey, K. Swanson, L. Fan-Chiang, G. Bagdasarov, N. Bobrova, V. Gasilov, G. Korn, P. Sasorov, and W. P. Leemans. Petawatt laser guiding and electron beam acceleration to 8 gev in a laser-heated capillary discharge waveguide. *Phys. Rev. Lett.*, 122:084801, Feb 2019.

[5] Alexander Buck, Maria Nicolai, Karl Schmid, Chris M. S. Sears, Alexander Sävert, Julia M. Mikhailova, Ferenc Krausz, Malte C. Kaluza, and Laszlo Veisz. Real-time observation of laser-driven electron acceleration. *Nature Physics*, 7(7):543–548, 2011.

[6] J. P. Couperus, R. Pausch, A. Köhler, O. Zarini, J. M. Krämer, M. Garten, A. Huebl, R. Gebhardt, U. Helbig, S. Bock, K. Zeil, A. Debus, M. Bussmann, U. Schramm, and A. Irman. Demonstration of a beam loaded nanocoulomb-class laser wakefield accelerator. *Nature Communications*, 8(1):487, 2017.

[7] O. Lundh, J. Lim, C. Rechatin, L. Ammoura, A. Ben-Ismaïl, X. Davoine, G. Gallot, J-P. Goddet, E. Lefebvre, V. Malka, and J. Faure. Few femtosecond, few kiloampere electron bunch produced by a laser–plasma accelerator. *Nature Physics*, 7(3):219–222, 2011.

[8] R. Weingartner, S. Raith, A. Popp, S. Chou, J. Wenz, K. Khrennikov, M. Heigoldt, A. R. Maier, N. Kajumba, M. Fuchs, B. Zeitler, F. Krausz, S. Karsch, and F. Grüner. Ultralow emittance electron beams from a laser-wakefield accelerator. *Phys. Rev. ST Accel. Beams*, 15:111302, Nov 2012.

[9] N Delbos, C Werle, I Dornmair, T Eichner, L Hübner, S Jalas, SW Jolly, M Kirchen, V Leroux, P Messner, et al. Lux–a laser–plasma driven undulator beamline. *Nuclear Instruments and Methods in Physics Research Section A: Accelerators, Spectrometers, Detectors and Associated Equipment*, 909:318–322, 2018.

[10] H. P. Schlenvoigt, K. Haupt, A. Debus, F. Budde, O. Jäckel, S. Pfotenhauer, H. Schwoerer, E. Rohwer, J. G. Gallacher, E. Brunetti, R. P. Shanks, S. M. Wiggins, and D. A. Jaroszynski. A compact synchrotron radiation source driven by a laser-plasma wakefield accelerator. *Nature Physics*, 4(2):130–133, 2008.

[11] Matthias Fuchs, Raphael Weingartner, Antonia Popp, Zsuzsanna Major, Stefan Becker, Jens Osterhoff, Isabella Cortrie, Benno Zeitler, Rainer Hörlein, George D. Tsakiris, Ulrich Schramm, Tom P. Rowlands-Rees, Simon M. Hooker, Dietrich Habs, Ferenc Krausz, Stefan Karsch, and Florian Grüner. Laser-driven soft-x-ray undulator source. *Nature Physics*, 5(11):826–829, 2009.

[12] A. R. Maier, N. Kajumba, A. Guggenmos, C. Werle, J. Wenz, N. Delbos, B. Zeitler, I. Dornmair, J. Schmidt, E. M. Gullikson, F. Krausz, U. Schramm, U. Kleineberg, S. Karsch, and F. Grüner. Water-window x-ray pulses from a laser-plasma driven undulator. *Scientific Reports*, 10(1):5634, 2020.

[13] Victor Malka, Jérôme Faure, Yannick Glinec, Clément Rechatin, Thomas Fuchs, Uwe Oelfke, and Hannitra Szymanowski. Medical applications with electron beam generated by laser plasma accelerators - art. no. 68810b. *Proc SPIE*, 6881, 02 2008.

[14] A. R. Maier, A. Meseck, S. Reiche, C. B. Schroeder, T. Seggebrock, and F. Grüner. Demonstration scheme for a laser-plasma-driven free-electron laser. *Phys. Rev. X*, 2:031019, Sep 2012.

[15] M E Couprie, M Labat, C Evain, F Marteau, F Briquez, M Khojoyan, C Benabderrahmane, L Chapuis, N Hubert, C Bourassin-Bouchet, M El Ajjouri, F Bouvet, Y Dietrich, M Valléau, G Sharma, W Yang, O Marcouillé, J Vétéran, P Berteaud, T El Ajjouri, L Cassinari, C Thaury, G Lambert, I Andriyash, V Malka, X Davoine, M A Tordeux, C Miron, D Zerbib, K Tavakoli, J L Marlats, M Tilmont, P Rommeluère, J P Duval, M H N'Guyen, A Rouqier, M Vanderbergue, C Herbeaux, M Sebdouai, A Lestrade, N Leclercq, D Dennetière, M Thomasset, F Polack, S Bielawski, C Szwaj, and A Loulergue. An application of laser–plasma acceleration: towards a free-electron laser amplification. *Plasma Physics and Controlled Fusion*, 58(3):034020, feb 2016.

[16] B M Alotaibi, Sh M Khalil, B W J McNeil, and Piotr Traczykowski. Modelling a laser plasma accelerator driven free electron laser. *Journal of Physics Communications*, 3(6):065007, jun 2019.

[17] E. Esarey, C. B. Schroeder, and W. P. Leemans. Physics of laser-driven plasma-based electron accelerators. *Rev. Mod. Phys.*, 81:1229–1285, Aug 2009.

[18] S. Kuschel, M. B. Schwab, M. Yeung, D. Hollatz, A. Seidel, W. Ziegler, A. Sävert, M. C. Kaluza, and M. Zepf. Controlling the self-injection threshold in laser wakefield accelerators. *Phys. Rev. Lett.*, 121:154801, Oct 2018.

[19] B. Beaurepaire, A. Vernier, Maimouna Bocoum, Frederik Böhle, A. Jullien, J-P Rousseau, T. Lefrou, Denis Douillet, G. Iaquaniello, Rodrigo Lopez-Martens, Agustin Lifschitz, and Jérôme Faure. Effect of the laser wave front in a laser-plasma accelerator. *Physical Review X*, 5, 01 2015.

[20] Hyung Taek Kim, VB Pathak, Ki Hong Pae, A Lifschitz, F Sylla, Jung Hun Shin, C Hojbota, Seong Ku Lee, Jae Hee Sung, Hwang Woon Lee, E Guillaume, C Thaury, Kazuhisa Nakajima, J Vieira, LO Silva, V Malka, and Chang Hee Nam. Stable multi-gev electron accelerator driven by waveform-controlled pw laser pulses. *Scientific reports*, 7(1):10203, August 2017.

[21] A. Popp, J. Vieira, J. Osterhoff, Zs. Major, R. Hörlein, M. Fuchs, R. Weingartner, T. P. Rowlands-Rees, M. Marti, R. A. Fonseca, S. F. Martins, L. O. Silva, S. M. Hooker, F. Krausz, F. Grüner, and S. Karsch. All-optical steering of laser-wakefield-accelerated electron beams. *Phys. Rev. Lett.*, 105:215001, Nov 2010.

[22] A. Modena, Z. Najmudin, A. E. Dangor, C. E. Clayton, K. A. Marsh, C. Joshi, V. Malka, C. B. Darrow, C. Danson, D. Neely, and F. N. Walsh. Electron acceleration from the breaking of relativistic plasma waves. *Nature*, 377(6550):606–608, 1995.

[23] J. Faure, Y. Glinec, A. Pukhov, S. Kiselev, S. Gordienko, E. Lefebvre, J. P. Rousseau, F. Burgy, and V. Malka. A laser–plasma accelerator producing monoenergetic electron beams. *Nature*, 431(7008):541–544, 2004.

[24] C. G. R. Geddes, K. Nakamura, G. R. Plateau, Cs. Toth, E. Cormier-Michel, E. Esarey, C. B. Schroeder, J. R. Cary, and W. P. Leemans. Plasma-density-gradient injection of low absolute-momentum-spread electron bunches. *Phys. Rev. Lett.*, 100:215004, May 2008.

[25] K. K. Swanson, H.-E. Tsai, S. K. Barber, R. Lehe, H.-S. Mao, S. Steinke, J. van Tilborg, K. Nakamura, C. G. R. Geddes, C. B. Schroeder, E. Esarey, and W. P. Leemans. Control of tunable, monoenergetic laser-plasma-accelerated electron beams using a shock-induced density downramp injector. *Phys. Rev. Accel. Beams*, 20:051301, May 2017.

[26] Anthony Gonsalves, Kei Nakamura, Chen Lin, S. Shiraishi, T. Sokollik, C. Benedetti, C. B. Schroeder, C. G. R. Geddes, J. van Tilborg, E. Esarey, C. Toth, D. Panasenko, J. Osterhoff, and Wim Leemans. Tunable laser plasma accelerator based on longitudinal density tailoring. *Nature Physics*, 7:862–866, 2011.

[27] E. Esarey, R. F. Hubbard, W. P. Leemans, A. Ting, and P. Sprangle. Electron injection into plasma wakefields by colliding laser pulses. *Phys. Rev. Lett.*, 79:2682–2685, Oct 1997.

[28] Jérôme Faure, Clément Rechatin, A Norlin, Agustin Lifschitz, Y Glinec, and Victor Malka. Controlled injection and acceleration of electrons in plasma wakefields by colliding laser pulses. *Nature*, 444:737–9, 12 2006.

[29] C. Rechatin, J. Faure, A. Ben-Ismail, J. Lim, R. Fitour, A. Specka, H. Videau, A. Tafzi, F. Burgy, and V. Malka. Controlling the phase-space volume of injected electrons in a laser-plasma accelerator. *Phys. Rev. Lett.*, 102:164801, Apr 2009.

[30] E. Oz, S. Deng, T. Katsouleas, P. Muggli, C. D. Barnes, I. Blumenfeld, F. J. Decker, P. Emma, M. J. Hogan, R. Ischebeck, R. H. Iverson, N. Kirby, P. Krejcik, C. O'Connell, R. H. Siemann, D. Walz, D. Auerbach, C. E. Clayton, C. Huang, D. K. Johnson, C. Joshi, W. Lu, K. A. Marsh, W. B. Mori, and M. Zhou. Ionization-nduced electron trapping in ultrarelativistic plasma wakes. *Phys. Rev. Lett.*, 98:084801, Feb 2007.

[31] T. P. Rowlands-Rees, C. Kamperidis, S. Kneip, A. J. Gonsalves, S. P. D. Mangles, J. G. Gallacher, E. Brunetti, T. Ibbotson, C. D. Murphy, P. S. Foster, M. J. V. Streeter, F. Budde, P. A. Norreys, D. A. Jaroszynski, K. Krushelnick, Z. Najmudin, and S. M. Hooker. Laser-driven acceleration of electrons in a partially ionized plasma channel. *Phys. Rev. Lett.*, 100:105005, Mar 2008.

[32] C McGuffey, AGR Thomas, W Schumaker, T Matsuoka, V Chvykov, FJ. Dollar, G. Kalintchenko, V. Yanovsky, A. Maksimchuk, K. Krushelnick, et al. Ionization induced trapping in a laser wakefield accelerator. *Physical Review Letters*, 104(2):025004, 2010.

[33] M. Chen, E. Esarey, C. B. Schroeder, C. G. R. Geddes, and W. P. Leemans. Theory of ionization-induced trapping in laser-plasma accelerators. *Physics of Plasmas*, 19(3):033101, 2012.

[34] Arthur Pak, KA. Marsh, SF. Martins, WB. Lu, W .and Mori, and C. Joshi. Injection and trapping of tunnel-ionized electrons into laser-produced wakes. *Physical Review Letters*, 104(2):025003, 2010.

[35] S. P. D. Mangles, G. Genoud, M. S. Bloom, M. Burza, Z. Najmudin, A. Persson, K. Svensson, A. G. R. Thomas, and C.-G. Wahlström. Self-injection threshold in

self-guided laser wakefield accelerators. *Physical Review Special Topics - Accelerators and Beams*, 15(1), Jan 2012.

[36] Ming Zeng, Nasr Hafz, Kazuhisa Nakajima, Li Chen, Wei Lu, W. Mori, Zheng-Ming Sheng, and Jie Zhang. Controlled ionization-induced injection by tailoring the gas-density profile in laser wakefield acceleration. *Journal of Plasma Physics*, 78:363–371, 08 2012.

[37] C. Thaury, E. Guillaume, A. Lifschitz, K. Ta Phuoc, M. Hansson, G. Grittani, J. Gautier, J. P. Goddet, A. Tafzi, O. Lundh, and V. Malka. Shock assisted ionization injection in laser-plasma accelerators. *Scientific Reports*, 5(1):16310, 2015.

[38] F. Li, J. F. Hua, X. L. Xu, C. J. Zhang, L. X. Yan, Y. C. Du, W. H. Huang, H. B. Chen, C. X. Tang, W. Lu, C. Joshi, W. B. Mori, and Y. Q. Gu. Generating high-brightness electron beams via ionization injection by transverse colliding lasers in a plasma-wakefield accelerator. *Phys. Rev. Lett.*, 111:015003, Jul 2013.

[39] L.-L. Yu, E. Esarey, C. B. Schroeder, J.-L. Vay, C. Benedetti, C. G. R. Geddes, M. Chen, and W. P. Leemans. Two-color laser-ionization injection. *Phys. Rev. Lett.*, 112:125001, Mar 2014.

[40] Song Li, Nasr A. M. Hafz, Mohammad Mirzaie, Thomas Sokollik, Ming Zeng, Min Chen, Zhengming Sheng, and Jie Zhang. Enhanced single-stage laser-driven electron acceleration by self-controlled ionization injection. *Opt. Express*, 22(24):29578–29586, Dec 2014.

[41] M. Mirzaie, S. Li, M. Zeng, N. A. M. Hafz, M. Chen, G. Y. Li, Q. J. Zhu, H. Liao, T. Sokollik, F. Liu, Y. Y. Ma, L. M. Chen, Z. M. Sheng, and J. Zhang. Demonstration of self-truncated ionization injection for gev electron beams. *Scientific Reports*, 5(1):14659, 2015.

[42] Anthony E. Siegman. *Lasers*. University Science Books, 1986.

[43] Dieter Meschede. *Optik, Licht und Laser*. Springer-Verlag, 2009.

[44] Robert J Goldston and Paul Harding Rutherford. *Introduction to plasma physics*. CRC Press, 1995.

[45] Paul Gibbon. *Short pulse laser interactions with matter*. World Scientific Publishing Company Singapore, 2004.

[46] CRC Handbook. *CRC Handbook of Chemistry and Physics, 88th Edition*. CRC Press, 88 edition, 2007.

[47] MV Ammosov, NB Delone, V Krainov, AM Perelomov, V Popov, M Terent'ev, Gennady L Yudin, and Misha Yu Ivanov. Tunnel ionization of complex atoms and of atomic ions in an alternating electric field. *Sov. Phys. JETP*, 64(6):1191–1194, 1986.

[48] W. Lu, C. Huang, M. Zhou, W. B. Mori, and T. Katsouleas. Nonlinear theory for relativistic plasma wakefields in the blowout regime. *Phys. Rev. Lett.*, 96:165002, Apr 2006.

[49] Mohammad Mirzaie, Guobo Zhang, Song Li, Kai Gao, Guangyu Li, Quratul Ain, and Nasr A. M. Hafz. Effect of injection-gas concentration on the electron beam quality from a laser-plasma accelerator. *Physics of Plasmas*, 25(4):043106, 2018.

[50] Jérôme Faure. Plasma injection schemes for laser-plasma accelerators. *arXiv preprint arXiv:1705.10542*, 2017.

[51] Thomas C. Katsouleas, S. Wilks, P. Chen, J. M. Dawson, and J. J. Su. Beam Loading in Plasma Accelerators. *Part. Accel.*, 22:81–99, 1987.

[52] Wei Lu, M Tzoufras, C Joshi, FS Tsung, WB Mori, J Vieira, RA Fonseca, and LO Silva. Generating multi-gev electron bunches using single stage laser wakefield acceleration in a 3d nonlinear regime. *Physical Review Special Topics-Accelerators and Beams*, 10(6):061301, 2007.

[53] C. G. Durfee, J. Lynch, and H. M. Milchberg. Development of a plasma waveguide for high-intensity laser pulses. *Phys. Rev. E*, 51:2368–2389, Mar 1995.

[54] D. J. Spence, A. J. Gonsalves, C. M. McKenna, and S. M. Hooker. Application of the Gas-Filled Capillary Discharge Waveguide to Laser-Plasma Acceleration. 737:825–831, 2004.

[55] E. Esarey, B. A. Shadwick, C. B. Schroeder, and W. P. Leemans. Nonlinear pump depletion and electron dephasing in laser wakefield accelerators. *AIP Conference Proceedings*, 737(1):578–584, 2004.

[56] Claire Ellen Max, Jonathan Arons, and A. Bruce Langdon. Self-modulation and self-focusing of electromagnetic waves in plasmas. *Phys. Rev. Lett.*, 33:209–212, Jul 1974.

[57] Jérôme Faure, Yannick Glinec, Jay Santos, F Ewald, J-P Rousseau, S Kiselev, A. Pukhov, T. Hosokai, and Victor Malka. Observation of laser-pulse shortening in nonlinear plasma waves. *Physical review letters*, 95:205003, 12 2005.

[58] Guo-Zheng Sun, Edward Ott, Y. C. Lee, and Parvez Guzdar. Self-focusing of short intense pulses in plasmas. *The Physics of Fluids*, 30(2):526–532, 1987.

[59] N. Delbos, C. Werle, I. Dornmair, T. Eichner, L. Hübner, S. Jalas, S.W. Jolly, M. Kirchen, V. Leroux, P. Messner, M. Schnepp, M. Trunk, P.A. Walker, P. Winkler, and A.R. Maier. Lux – a laser–plasma driven undulator beamline. *Nuclear Instruments and Methods in Physics Research Section A: Accelerators, Spectrometers, Detectors and Associated Equipment*, 909:318 – 322, 2018. 3rd European Advanced Accelerator Concepts workshop (EAAC2017).

[60] Werle Christian Markus. *First Undulator Experiments at te LUX Beamline: Towards a Plasma-Based Accelerator as Soft X-ray Source.* PhD thesis, University of Hamburg, Fachbereich Physik, Hamburg, Germany, 2019.

[61] Donna Strickland and Gerard Mourou. Compression of amplified chirped optical pulses. *Optics communications*, 56(3):219–221, 1985.

[62] Vincent Leroux, Spencer Jolly, Matthias Schnepp, Timo Eichner, Sören Jalas, Manuel Kirchen, Philipp Messner, Christian Werle, Paul Winkler, and Andreas Maier. Wavefront degradation of a 200 tw laser from heat-induced deformation of in-vacuum compressor gratings. *Optics Express*, 26:13061, 05 2018.

[63] yi xu, Jianzhou Wang, Yansui Huang, Yanyan Li, Xiaomin Lu, and Yuxin Leng. Nonlinear temporal pulse cleaning techniques and application. *High Power Laser Science and Engineering*, 1, 09 2013.

[64] Fastlite. Dazzler, ultrafast pulse shaper. http://www.fastlite.com/en/ar824665-823529-Dazzler.html. Accessed: 2019-04-18.

[65] Pierre Tournois. Acousto-optic programmable dispersive filter for adaptive compensation of group delay time dispersion in laser systems. *Optics communications*, 140(4-6):245–249, 1997.

[66] Vincent Leroux. *On the wavefront of ultrahigh intensity laser: spatial contrast and gratings deformation.* PhD thesis, University of Hamburg, Fachbereich Physik, Hamburg, Germany, 2018.

[67] Fastlite. Wizzler, single-shot, high contrast pulse measurement. http://www.fastlite.com/en/ar824651-823532-Wizzler.html. Accessed: 2019-04-18.

[68] Swamp Optics. Grenouille. http://www.swampoptics.com/grenouille.html. Accessed: 2020-01-23.

[69] Thomas Oksenhendler, Sebastien Coudreau, Nicolas Forget, V Crozatier, S Grabielle, R Herzog, O Gobert, and D Kaplan. Self-referenced spectral interferometry. *Applied Physics B*, 99(1-2):7–12, 2010.

[70] Rick Trebino, Kenneth W. DeLong, David N. Fittinghoff, John N. Sweetser, Marco A. Krumbügel, Bruce A. Richman, and Daniel J. Kane. Measuring ultrashort laser pulses in the time-frequency domain using frequency-resolved optical gating. *Review of Scientific Instruments*, 68(9):3277–3295, 1997.

[71] Adam Borzsonyi, Attila Kovács, and Karoly Osvay. What we can learn about ultrashort pulses by linear optical methods. *Applied Sciences*, 3:515–544, 06 2013.

[72] Winkler Paul. Electron beam focusing at the laser wakefield accelerator lux. Master's thesis, University of Hamburg, Fachbereich Physik, Hamburg, Germany, 2015.

[73] Helmholtz zentrum dresden-rossendorf (HZDR. Helmholtz-zentrum dresden-rossendorf (hzdr. https://www.hzdr.de/db/Cms?pNid=0. Accessed: 2019-02-25.

[74] CAWO Solutions. Green emitting screens. https://www.cawo.com/products/intensifying-screens/green-emitting/. Accessed: 2019-02-25.

[75] Klaus Wille. *The physics of particle accelerators: an introduction.* Clarendon Press, 2000.

[76] Klaus Flöttmann. Astra, a space charge tracking algorithm. http://www.desy.de/~mpyflo/Astra_manual/Astra-Manual_V3.2.pdf. Accessed: 2019-02-19.

[77] J. Rossbach and Peter Schmueser. Basic course on accelerator optics. *Conf. Proc.*, C9209071:17–88, 1992.

[78] Hübner" "Lars. Single shot emittance measurements of laser-wakefield accelerated electron beams at lux. Master's thesis, University of Hamburg, Fachbereich Physik, Hamburg, Germany, 2018.

[79] Winkler Paul. Emittance measurements at laser-wakefield accelerators. Master's thesis, University of Hamburg, Fachbereich Physik, Hamburg, Germany, 2019.

[80] Basler AG. aca2000-50gm - basler ace. https://www.baslerweb.com/de/produkte/kameras/flaechenkameras/ace/aca2000-50gm/. Accessed: 2019-02-25.

[81] Kowa Optimed. Kowa-lm12hc. https://www.kowa-lenses.com/industrie-objektive/305/lm12hc. Accessed: 2020-02-10.

[82] C. Wiebers et all. Scintillating screen monitors for transverse electron beam profile diagnostics at the european xfel. In Ian Martin and Guenther Rehm, editors, *IBIC2013: Proceedings of the 2nd International Beam Instrumentation Conference*, pages 807–810. JACoW, 2013.

[83] Schneider Kreuznach. Schneider kreuznach 120/5,6 makro-symmar hm. https://schneiderkreuznach.com/en/industrial-optics/lenses-v38-line-scan-macro-system. Accessed: 2020-01-23.

[84] Basler AG. ava2300-25gm - basler aviator. `https://www.baslerweb.com/de/produkte/kameras/flaechenkameras/aviator/ava2300-25gm/`. Accessed: 2020-01-23.

[85] A. Buck, K. Zeil, A. Popp, K. Schmid, A. Jochmann, S. D. Kraft, B. Hidding, T. Kudyakov, C. M. S. Sears, L. Veisz, S. Karsch, J. Pawelke, R. Sauerbrey, T. Cowan, F. Krausz, and U. Schramm. Absolute charge calibration of scintillating screens for relativistic electron detection. *Review of Scientific Instruments*, 81(3):033301, 2010.

[86] B. Keil et all. The european xfel beam positioning monitor system. In Shin ichi Kurokawa and Katsunobu Oide, editors, *Proceedings of IPAC'10*, pages 1125–1127. ACM, 2010.

[87] S. Semushin and V. Malka. High density gas jet nozzle design for laser target production. *Review of Scientific Instruments*, 72(7):2961–2965, 2001.

[88] K. Schmid and L. Veisz. Supersonic gas jets for laser-plasma experiments. *Review of Scientific Instruments*, 83(5):053304, 2012.

[89] S. Semushin and V. Malka. High density gas jet nozzle design for laser target production. *Review of Scientific Instruments*, 72(7):2961–2965, 2001.

[90] F. Sylla, M. Veltcheva, S. Kahaly, A. Flacco, and V. Malka. Development and characterization of very dense submillimetric gas jets for laser-plasma interaction. *Review of Scientific Instruments*, 83(3):033507, 2012.

[91] T.L. Audet, P. Lee, G. Maynard, S. Dobosz Dufrénoy, A. Maitrallain, M. Bougeard, P. Monot, and B. Cros. Gas cell density characterization for laser wakefield acceleration. *Nuclear Instruments and Methods in Physics Research Section A: Accelerators, Spectrometers, Detectors and Associated Equipment*, 909:383 – 386, 2018. 3rd European Advanced Accelerator Concepts workshop (EAAC2017).

[92] C. Aniculaesei, Hyung Taek Kim, Byung Ju Yoo, Kyung Hwan Oh, and Chang Hee Nam. Novel gas target for laser wakefield accelerators. *Review of Scientific Instruments*, 89(2):025110, 2018.

[93] F Filippi, M P Anania, E Brentegani, A Biagioni, A Cianchi, E Chiadroni, M Ferrario, R Pompili, S Romeo, and A Zigler. Gas-filled capillaries for plasma-based accelerators. *Journal of Physics: Conference Series*, 874:012036, jul 2017.

[94] R. Ariniello, C. E. Doss, K. Hunt-Stone, J. R. Cary, and M. D. Litos. Transverse beam dynamics in a plasma density ramp. *Phys. Rev. Accel. Beams*, 22:041304, Apr 2019.

[95] I. Dornmair, K. Floettmann, and A. R. Maier. Emittance conservation by tailored focusing profiles in a plasma accelerator. *Phys. Rev. ST Accel. Beams*, 18:041302, Apr 2015.

[96] Crystran Ltd. Sapphire al2o3 data sheet. http://www.crystran.co.uk/userfiles/files/sapphire-al2o3-data-sheet.pdf. Accessed: 2020-01-27.

[97] The OpenFOAM Foundation. Openfoam. https://openfoam.org. Accessed: 2019-03-27.

[98] Y. Nakayama and R.F. Boucher. *Introduction to Fluid Mechanics*. Wiley, 1997.

[99] The OpenFOAM Foundation. sonicfoam. https://cfd.direct/openfoam/user-guide/v6-standard-solvers/#dx13-99012. Accessed: 2020-02-23.

[100] The OpenFOAM Foundation. Openfoam v6 user guide: 5.2 boundaries. https://cfd.direct/openfoam/user-guide/v6-boundaries/. Accessed: 2019-03-28.

[101] R. Courant, K. Friedrichs, and H. Lewy. Über die partiellen differenzengleichungen der mathematischen physik. *Mathematische Annalen*, 100(1):32–74, Dec 1928.

[102] The OpenFOAM Foundation. Openfoam v6 user guide: 7.1 thermophysical models. https://cfd.direct/openfoam/user-guide/v6-thermophysical/. Accessed: 2019-03-28.

[103] The Engineering ToolBox. Hydrogen-thermophysical properties. https://www.engineeringtoolbox.com/hydrogen-d_1419.html. Accessed: 2020-01-27.

[104] The Engineering ToolBox. Nitrogen-thermophysical properties. https://www.engineeringtoolbox.com/nitrogen-d_1421.html. Accessed: 2020-01-27.

[105] Bruce E Poling, John M Prausnitz, John P O'connell, et al. *The properties of gases and liquids*, volume 5. Mcgraw-hill New York, 2001.

[106] Alexandra Wassiljewa. Warmeleitung in gasgemischen. *Physik. Z.*, 5:737–742, 1904.

[107] L. D. Landau and E. M. Lifshitz. *Fluid Mechanics, Second Edition: Volume 6 (Course of Theoretical Physics)*. Course of theoretical physics / by L. D. Landau and E. M. Lifshitz, Vol. 6. Butterworth-Heinemann, 2 edition, January 1987.

[108] B.G. Lipták. *Instrument engineers' handbook: Process measurement and analysis, fourth edition*. 01 2003.

[109] Pfeiffer Vacuum. Active line transmitter cmr 361. https://www.pfeiffer-vacuum.com/de/produkte/messung-analyse/messgeraete/activeline/activeline-transmitter/?detailPdoId=4366. Accessed: 2019-03-31.

[110] Philipp Messner. Target design and diagnostics for laser wakefield acceleration. Master's thesis, University of Hamburg, Fachbereich Physik, Hamburg, Germany, 2015.

[111] QCAL Messtechnik GmbH. Gasmischer gms 2ch. https://www.qcal.de/deutsch/2-3-kanal-gasmischer/. Accessed: 2019-04-10.

[112] SENSIRION AG. Datasheet sfc5400 mass flow controller. https://www.sensirion.com/fileadmin/user_upload/customers/sensirion/Dokumente/0_Datasheets/Mass_Flow_Controller/Sensirion_Mass_Flow_Controllers_SFC5400_Datasheet.pdf. Accessed: 2019-04-10.

[113] Patrick Lee, G. Maynard, Thomas Audet, Remi Lehe, J. Vay, and B. Cros. Optimization of laser-plasma injector via beam loading effects using ionization-induced injection. *Physical Review Accelerators and Beams*, 21, 11 2017.

[114] Rémi Lehe, Manuel Kirchen, Igor A. Andriyash, Brendan B. Godfrey, and Jean-Luc Vay. A spectral, quasi-cylindrical and dispersion-free particle-in-cell algorithm. *Computer Physics Communications*, 203:66–82, Jun 2016.

[115] Klaus Floettmann. Adiabatic matching section for plasma accelerated beams. *Phys. Rev. ST Accel. Beams*, 17:054402, May 2014.

[116] M.-W. Lin, C.-Y. Hsieh, D. K. Tran, and S.-H. Chen. Simulation study of ionization-induced injection in sub-terawatt laser wakefield acceleration. *Physics of Plasmas*, 27(1):013102, 2020.

[117] Maxence Thévenet, Daniel E. Mittelberger, Kei Nakamura, Rémi Lehe, Carl B. Schroeder, Jean-Luc Vay, Eric Esarey, and Wim P. Leemans. Pulse front tilt steering in laser plasma accelerators. *Phys. Rev. Accel. Beams*, 22:071301, Jul 2019.

[118] Selcuk Akturk, Xun Gu, Erik Zeek, and Rick Trebino. Spatial chirp and pulse-front tilt in ultrashort laser pulses and their measurement. In *International Conference on Ultrafast Phenomena*, page ME39. Optical Society of America, 2004.

[119] Clément Rechatin, Xavier Davoine, Augustin Lifschitz, A. Ismail, Jae Lim, E Lefebvre, Jérôme Faure, and Victor Malka. Observation of beam loading in a laser-plasma accelerator. *Physical review letters*, 103:194804, 11 2009.

[120] I Gallardo González, H Ekerfelt, M Hansson, T L Audet, B Aurand, F G Desforges, S Dobosz Dufrénoy, A Persson, X Davoine, C-G Wahlström, B Cros, and O Lundh. Effects of the dopant concentration in laser wakefield and direct laser acceleration of electrons. *New Journal of Physics*, 20(5):053011, may 2018.

[121] Christos Kamperidis, Dimitriou Vasillis, Stuart Mangles, A E Dangor, and Zul-fikar Najmudin. Low energy spread electron beams from ionization injection in a weakly relativistic laser wakefield accelerator. *Plasma Physics and Controlled Fusion*, 56:084007, 07 2014.

[122] Mohammad Mirzaie, Guobo Zhang, Song Li, Kai Gao, Guangyu Li, Quratul Ain, and Nasr Hafz. Effect of injection-gas concentration on the electron beam quality from a laser-plasma accelerator. *Physics of Plasmas*, 25:043106, 04 2018.

[123] C. B. Schroeder, J.-L. Vay, E. Esarey, S. S. Bulanov, C. Benedetti, L.-L. Yu, M. Chen, C. G. R. Geddes, and W. P. Leemans. Thermal emittance from ionization-induced trapping in plasma accelerators. *Phys. Rev. ST Accel. Beams*, 17:101301, Oct 2014.

[124] SK Barber, J Van Tilborg, CB Schroeder, R Lehe, HE Tsai, KK Swanson, S Steinke, K Nakamura, CGR Geddes, C Benedetti, et al. Parametric emittance measurements of electron beams produced by a laser plasma accelerator. *Plasma Physics and Controlled Fusion*, 60(5):054015, 2018.

[125] K. Khrennikov, J. Wenz, A. Buck, J. Xu, M. Heigoldt, L. Veisz, and S. Karsch. Tunable all-optical quasimonochromatic thomson x-ray source in the nonlinear regime. *Phys. Rev. Lett.*, 114:195003, May 2015.

[126] J. Tilborg, Sven Steinke, C. Geddes, Nicholas Matlis, Brian Shaw, Anthony Gonsalves, J. Huijts, Kei Nakamura, Joost Daniels, C. Schroeder, Carlo Benedetti, E. Esarey, S. Bulanov, Nadezhda Bobrova, P. Sasorov, and Wim Leemans. Active plasma lensing for relativistic laser-plasma-accelerated electron beams. *Physical Review Letters*, 115:184802, 11 2015.

[127] Trunk Maximilian. Construction and characterization of the undulator beast 2. Master's thesis, University of Hamburg, Fachbereich Physik, Hamburg, Germany, 2016.

[128] Tae Hyun Yoon. Applications of soft x-ray spectromicroscopy in material and environmental sciences. *Applied Spectroscopy Reviews*, 44(2):91–122, 2009.

Acknowledgement

First of all, im grateful to Andreas R. Maier and Joerg Rossbach for supervising my PhD project. Especially to Andreas, who gave me the opportunity to join the LUX team and supported me strongly during the very exciting last few years.

I would also like to thank the Max Planck Institute for the Structure and Dynamics of Matter for founding my PhD projected.

The last years would have not been as exciting and fun without the strong group cohesion at LUX. I would therefore like to express my particular gratitude to the members of the LUX team for all their assistance. Special thanks should go to Vincent Leroux, Paul Winkler, Manuel Kirchen and Sören Jalas not only for their incredible support at work but also for the great moments we spent outside of work.

Lastly, i would like to thank my family and dear friends on which i can always count.